

SYNTHESIS AND STRUCTURE-PROPERTY RELATIONSHIPS IN RARE EARTH DOPED BISMUTH FERRITE

Christopher M. Kavanagh

**A Thesis Submitted for the Degree of PhD
at the
University of St Andrews**



2013

**Full metadata for this item is available in
St Andrews Research Repository
at:**

<http://research-repository.st-andrews.ac.uk/>

Please use this identifier to cite or link to this item:

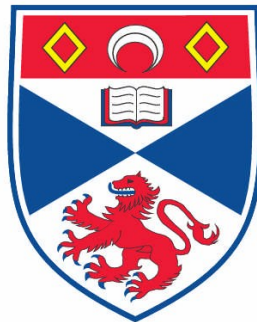
<http://hdl.handle.net/10023/3555>

This item is protected by original copyright

**This item is licensed under a
Creative Commons Licence**

Synthesis and Structure-Property Relationships in Rare Earth Doped Bismuth Ferrite

Christopher M. Kavanagh



This thesis is submitted in partial fulfilment for the degree of
PhD
at the
University of St Andrews

Date of Submission

March 2013

1. Candidate's declarations:

I, Christopher Kavanagh hereby certify that this thesis, which is approximately 36,144 words in length, has been written by me, that it is the record of work carried out by me and that it has not been submitted in any previous application for a higher degree.

I was admitted as a research student in March 2009 and as a candidate for the degree of PhD in March 2010; the higher study for which this is a record was carried out in the University of St Andrews between 2009 and 2013.

Date signature of candidate

2. Supervisor's declaration:

I hereby certify that the candidate has fulfilled the conditions of the Resolution and Regulations appropriate for the degree of PhD in the University of St Andrews and that the candidate is qualified to submit this thesis in application for that degree.

Date signature of supervisor

signature of supervisor

3. Permission for electronic publication:

In submitting this thesis to the University of St Andrews I understand that I am giving permission for it to be made available for use in accordance with the regulations of the University Library for the time being in force, subject to any copyright vested in the work not being affected thereby. I also understand that the title and the abstract will be published, and that a copy of the work may be made and supplied to any bona fide library or research worker, that my thesis will be electronically accessible for personal or research use unless exempt by award of an embargo as requested below, and that the library has the right to migrate my thesis into new electronic forms as required to ensure continued access to the thesis. I have obtained any third-party copyright permissions that may be required in order to allow such access and migration, or have requested the appropriate embargo below.

The following is an agreed request by candidate and supervisor regarding the electronic publication of this thesis:

Embargo on both all of printed copy and electronic copy for the same fixed period of 2 years on the following ground:

publication would preclude future publication;

Date signature of candidate signature of supervisor

signature of supervisor

Abstract

There has been significant interest in BiFeO_3 over the past decade. This interest has focused on the magnetic and electrical properties, which in the long term may prove useful in device applications.

This thesis focuses on the synthesis, electrical characterisation, and structural origin of the electrical properties of rare earth doped bismuth ferrite. Two systems have been studied: BiFeO_3 doped with lanthanum and neodymium ($\text{Bi}_{1-x}\text{RE}_x\text{FeO}_3$ RE= La, Nd). Specific examples have been highlighted focusing on a detailed structural analysis of a lanthanum doped bismuth ferrite, $\text{Bi}_{0.5}\text{La}_{0.5}\text{FeO}_3$, and a neodymium analogue, $\text{Bi}_{0.7}\text{Nd}_{0.3}\text{FeO}_3$. Both adopt an orthorhombic GdFeO_3 -type structure (space group: $Pnma$) with G-type antiferromagnetism.

Structural variations were investigated by Rietveld refinement of temperature dependent powder neutron diffraction using a combination of both conventional “bond angle/bond length” and symmetry-mode analysis. The latter was particularly useful as it allowed the effects of A-site displacements and octahedral tilts/distortions to be considered separately. This in-depth structural analysis was complemented with ac-immittance spectroscopy using the multi-formulism approach of combined impedance and modulus data to correlate structural changes with the bulk electrical properties. This approach was essential due to the complex nature of the electrical response with contributions from different electroactive regions.

The structural variations occur due to a changing balance between magnetic properties and other bonding contributions in the respective systems. This results in changes in the magnitude of the octahedral tilts, and A-site displacements giving rise to phenomena such as negative thermal expansion and invariant lattice parameters *i.e.*, the invar effect.

More specifically, analysis of $\text{Bi}_{0.5}\text{La}_{0.5}\text{FeO}_3$ highlights a structural link between changes in the relative dielectric permittivity and changes in the FeO_6 octahedral tilt magnitudes, accompanied by a structural distortion of the octahedra with corresponding A-site

displacement along the c -axis; this behaviour is unusual due to an increasing in-phase tilt mode with increasing temperature. The anomalous orthorhombic distortion is driven by magnetostriction at the onset of antiferromagnetic ordering resulting in an Invar effect along the magnetic c -axis and anisotropic displacement of the A-site Bi^{3+} and La^{3+} along the a -axis. This contrasts with the neodymium analogue $\text{Bi}_{0.7}\text{Nd}_{0.3}\text{FeO}_3$ in which a combination of increasing A-site displacements in the ac -plane and decrease in both in-phase and anti-phase tilts combine with superexchange giving rise to negative thermal expansion at low temperature. The A-site displacements correlate with the orthorhombic strain.

By carefully changing the synthesis conditions, a significant change in bulk conductivity was observed for a number of $\text{Bi}_{1-x}\text{La}_x\text{FeO}_3$ compositions. A series of $\text{Bi}_{0.6}\text{La}_{0.4}\text{FeO}_3$ samples are discussed, where changes in the second step of the synthesis result in significantly different bulk conductivities. This behaviour is also observed in other compositions *e.g.* $\text{Bi}_{0.75}\text{La}_{0.25}\text{FeO}_3$. Changes in the electrical behaviour as a function of temperature are discussed in terms of phase composition and concentration gradients of defects. Activation energies associated with the conduction process(es) in $\text{Bi}_{1-x}\text{La}_x\text{FeO}_3$ samples, regardless of composition, fall within one of two broad regimes, *circa*. 0.5 eV or 1.0 eV, associated with polaron hopping or migration of charge *via* oxygen vacancies, respectively.

The use of symmetry-mode analysis, in combination with conventional crystallographic analysis and electrical analysis using multi-formalism approach, presents a new paradigm for investigation of structure-property relationships in rare earth doped BiFeO_3 .

Acknowledgments

First and foremost, I would like to acknowledge the help of my supervisors Dr Finlay Morrison and Professor Philip Lightfoot without their help and guidance I would not have made it this far through my PhD.

Finlay has been an invaluable mentor, teaching not just me but the whole group about ac-
c-
mittance spectroscopy and other analytical techniques, in a calm and collected manner. His door has always been open to those in need of a little bit of help and guidance. Over the years, my PhD has shifted towards developing an understanding of the electrical and structural relations in materials. In this regard, Phil has been able to offer helpful advice in some of our long discussions relating to the crystallography presented within this thesis.

During my PhD, I have had the opportunity on two occasions to use the HRPD diffractometer at the ISIS neutron spallation source. I would like to thank the beam line scientist, Dr Aziz Daoud-Aladine for his assistance and expertise whenever a problem arose with the instrument.

There have been a number of members of Morrison group, past and present that have offered assistance during the course of my PhD. Dr Donna Arnold and Andrei Rotaru were there from the beginning of my PhD in St Andrews offering help from day one. From the Lightfoot group Dr Richard Goff provided help with the initial refinements of some of the powder neutron diffraction patterns. Over the years, these members have left the group and new members have joined. I would like to wish Sarah Turp and Jonathan Gardner the best of luck in completing their theses.

Over the past couple of years, I have developed a number of computer controlled analytical techniques. This task would have been significantly harder without the helpful programming framework developed by my brother Richard Kavanagh.

A PhD at times can be an emotional roller coaster, with this in mind I would like to thank my friends that have not been mentioned so far. Specifically, I would like to mention Katie Renouf, Judith Reeks and Nicolas Drewett. They have always offered a helping hand and have been there when I have needed someone to listen to me.

Finally, I would like to thank my parents Stuart and Denise Kavanagh and the rest of my family. Their endless years of help and support have allowed me to get where I am today.

Contents

Abstract.....	i
Acknowledgments.....	iii
Contents.....	v
Abbreviations list	xi
1 Introduction and Background.....	1
1.1 Background - The perovskite structure.....	1
1.2 Crystallography ⁷⁻¹⁰	5
1.2.1 Symmetry operations ^{7,9}	8
1.2.2 Miller indices and planes	9
1.3 Symmetry and magnetism ^{11, 12}	10
1.4 Magnetic order and Shubnikov symmetry.....	11
1.5 Electroceramic materials.....	14
1.6 Polar dielectrics ^{15, 16}	16
1.7 Multiferroic materials	18
1.8 Multiferroic BiFeO ₃	20
1.9 Rare earth doped BiFeO ₃	23
1.10 Bi _{1-x} La _x FeO ₃	23
1.11 Bi _{1-x} Pr _x FeO ₃	25
1.12 Bi _{1-x} Nd _x FeO ₃	25
1.13 Bi _{1-x} Sm _x FeO ₃	27

1.14	$\text{Bi}_{1-x}\text{RE}_x\text{FeO}_3$ RE = Eu, Gd, Tb, Dy	27
1.15	Thesis overview	28
1.16	Aims and objectives	29
1.17	References.....	30
2	Experimental Methods	33
2.1	Synthesis.....	33
2.1.1	Solid state synthesis – BiFeO_3 ¹	33
2.1.2	Synthesis of $\text{Bi}_{1-x}\text{RE}_x\text{FeO}_3$ (RE = La, Nd)	34
2.1.3	Synthesis of $\text{Bi}_{1-x}\text{RE}_x\text{FeO}_3$ (RE = Nd $x \leq 0.2$, La $x \leq 0.25$)	34
2.1.4	Synthesis of $\text{Bi}_{1-x}\text{RE}_x\text{FeO}_3$ (RE = Nd $x > 0.2$, La $x > 0.25$)	35
2.2	Powder x-ray diffraction.....	35
2.2.1	Fundamentals of x-ray diffraction ^{3,4}	36
2.2.2	Reciprocal lattice and Ewald's sphere ³⁻⁵	37
2.3	Generation of x-rays ^{3,4}	39
2.4	Powder neutron diffraction (c.f. PXRD).....	40
2.4.1	Fundamentals of neutron diffraction ^{4,6}	41
2.4.2	Generation of neutrons ⁷	41
2.5	HRPD instrument ⁸	42
2.6	Rietveld refinement ⁹⁻¹²	43
2.7	ac - Impedance spectroscopy	46
2.7.1	The impedance formalisms	47

2.7.2	Sample preparation	51
2.7.3	Ceramics and the brick layer model	52
2.7.4	Data collection	55
2.7.5	Total capacitance and loss sweeps	56
2.7.6	(ac-IS) Data analysis of isothermal data.....	57
2.7.7	Activation energies	62
2.8	Scanning electron microscopy with energy-dispersive x-rays	62
2.9	References.....	63
3	A Magnetically driven dielectric: $\text{Bi}_{0.5}\text{La}_{0.5}\text{FeO}_3$	65
3.1	Introduction.....	65
3.2	Experimental Method	67
3.3	Preliminary structural analysis	68
3.4	Electrical Properties	76
3.5	Correlation of structure and dielectric response	81
3.6	Structural response to magnetic ordering	84
3.7	Conclusions.....	92
3.8	References.....	93
4	Superexchange mediated negative thermal expansion in $\text{Bi}_{0.7}\text{Nd}_{0.3}\text{FeO}_3$	95
4.1	Introduction.....	95
4.2	Experimental	97

4.3	Results - Preliminary structural analysis	97
4.4	Strain and the impact on diffraction	103
4.5	Electrical properties	105
4.6	Activation energy of the bulk conduction process.	115
4.7	Correlation between structural behaviour and the dielectric response	116
4.8	Structural changes and magnetic ordering	127
4.9	Conclusions.....	130
4.10	References.....	131
5	Variations in the electrical properties of rare earth doped BiFeO ₃	133
5.1	Introduction.....	133
5.2	Experimental	135
5.3	Results	135
5.4	Preliminary Structural analysis – BLFO40 with temperature.....	135
5.5	Electrical response - BLFO40 1000 °C in Air	138
5.6	Electrical response - BLFO40 1000 °C N ₂	142
5.7	BLFO40 1100 Air	144
5.8	Comparison of bulk and “total sample” permittivities	145
5.9	BLFO25 1000 °C N ₂	147
5.10	Possible origins of the changes in the electrical response	151
5.11	Activation energies in Bi _{1-x} La _x FeO ₃	156
5.12	Conclusions.....	157
5.13	References.....	159

6	Summary, Conclusions and Future work.....	161
6.1	Summary	161
6.2	Conclusions.....	161
6.3	Further Work.....	163
6.4	References.....	164

Abbreviations list

ac-IS: Alternating current immittance spectroscopy

AFM: Antiferromagnetic order

BNFO30: $\text{Bi}_{0.7}\text{Nd}_{0.3}\text{FeO}_3$

BLFO25: $\text{Bi}_{0.75}\text{La}_{0.25}\text{FeO}_3$

BLFO40: $\text{Bi}_{0.6}\text{La}_{0.4}\text{FeO}_3$

BLFO50: $\text{Bi}_{0.5}\text{La}_{0.5}\text{FeO}_3$

DFT: Density functional theory

EDX: Energy dispersive x-ray system

FWHM: Full width half maximum

GSAS: General structural analysis system

HRPD: High-resolution powder diffraction

ICSD: Inorganic Crystal Structure Database

Linac: Linear accelerator

PND: Powder neutron diffraction

PXRD: Powder x-ray diffraction

RFQ: Radio frequency quadrupole

SEM: Scanning electron microscope

SPXRD: Synchrotron powder X-ray diffraction

XRD: X-ray diffraction

Introduction and Background

1.1 Background - The perovskite structure

BiFeO_3 and the doped derivatives presented within this thesis adopt the perovskite structure. The perovskite structure is a very common structural type of the form ABX_3 where A and B represent a large and smaller cation, respectively. X represents an anion such as a halide, but more commonly oxygen. The structure consists of a three dimensional network of corner sharing BX_6 octahedra with an interpenetrating primitive lattice of A-site atoms.

The name of the perovskite structure has been taken from the mineralogical name of CaTiO_3 that adopts a pseudo-cubic form of this structure. There are two possible representations of the structure with the A-site at the origin or at the centre of the unit cell. A representation of the perovskite structure is shown in Figure 1.1.

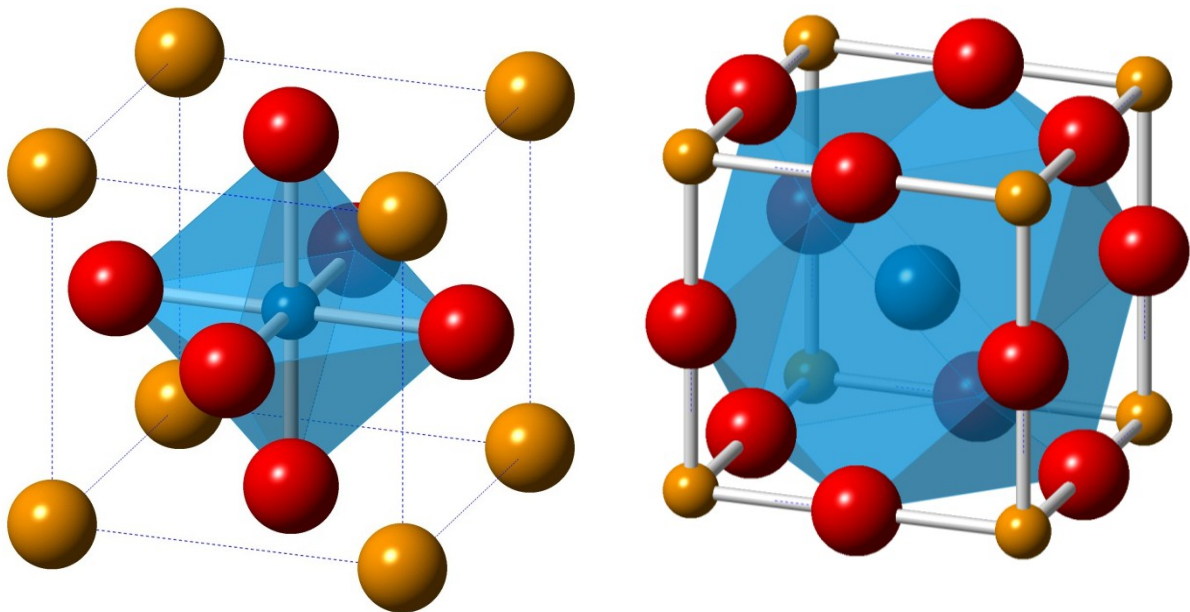


Figure 1.1: The unit cell of a cubic perovskite: a) showing the BX_6 octahedra at the centre of the unit cell with a primitive arrangement of A-site atoms at the cell edges (left). b) The alternate representation of the perovskite structure (right) shows the idealised AO_{12} dodecahedron of the A-site surrounded by BX_6 octahedra in the extended lattice. A-site: orange B-site: Blue X: red spheres, respectively.

In reality, the perovskite structure is very flexible and will form a variety of different non-cubic structures. The BX_6 octahedra are typically “rigid” such that to distort the structure away from the cubic model the octahedra must tilt. There are also atomic displacements, which may cause the octahedra to distort. This brings in two concepts: tilt systems and the degree by which a perovskite can distort away from the cubic structure.

The degree of distortion away from the cubic structure can be described with simple geometry. This idea of a tolerance factor, t , was developed by Goldschmidt in 1926. It assumes ionic bonding and relates the radii of the A-site cation and anion to that of the B-site via Equation 1.1.¹

$$t = \frac{(R_A + R_x)}{\sqrt{2}(R_B + R_x)} \quad \text{Equation 1.1}$$

Tolerance factors above one ($t > 1$) mean that the A-site is larger than the BX_6 octahedral framework can comfortably accommodate. The structure will therefore distort to accommodate the A-site. Tolerance factors less than one ($t < 1$) mean that the A-site cannot occupy the whole space of the undistorted dodecahedra volume and the octahedra will tilt in order to shorten the A-X bond length. This idea of the octahedra rotating to maximise ionic bonding, perhaps in competition with other effects such as magnetism, is an important concept in understanding perovskites and their physical properties.

The tilt systems have been described in a number of papers²⁻⁵ over the years based on Glazer’s 1972 paper⁶, which describes the accepted method for classifying tilts in perovskites. There are three possible independent tilts, if they are not equivalent by symmetry, along the axes of the pseudo-cubic unit cell [100], [010] and [001]; these are assigned letters a , b , and c for non-equivalent magnitudes of tilts. Tilts are also assigned symbols denoting if the tilt of the neighbouring octahedra are the same, opposite, or if the octahedra have no tilt with respect to each axis and are denoted by +, -, or 0, respectively. Glazer’s original 23 different tilt systems are summarised in Table 1.1, with the corresponding space groups.

Table 1.1: The 23 Glazer tilt systems with accompanying space groups⁶

Tilt system number	Symbol	Space group	Tilt system number	Symbol	Space group
1	$a^+b^+c^+$	<i>I</i> mmm (#71)	13	$a^-b^-b^-$	<i>I</i> 2/a (#15-3)
2	$a^+b^+b^+$	<i>I</i> mmm (#71)	14	$a^-a^-a^-$	<i>R</i> -3c (#167-2)
3	$a^+a^+a^+$	<i>I</i> m-3 (#204)	15	$a^0b^+c^+$	<i>I</i> mmm (#71)
4	$a^+b^+c^-$	<i>P</i> mmn (#59-2)	16	$a^0b^+b^+$	<i>I</i> 4/mmm (#139)
5	$a^+a^+c^-$	<i>P</i> mmn (#59-2)	17	$a^0b^+c^-$	<i>P</i> mmn (#59-2)
6	$a^+b^+b^-$	<i>P</i> mmn (#59-2)	18	$a^0b^+b^-$	<i>P</i> mmn (#59-2)
7	$a^+a^+a^-$	<i>P</i> mmn (#59-2)	19	$a^0b^-c^-$	<i>I</i> 2/m (#123)
8	$a^+b^-c^-$	<i>P</i> 2 ₁ /m (#11-1)	20	$a^0b^-b^-$	<i>I</i> mma (#74)
9	$a^+a^-c^-$	<i>P</i> 2 ₁ /m(#11-1)	21	$a^0a^0c^+$	<i>P</i> 4/mbm (#127)
10	$a^+b^-b^-$	<i>P</i> nma (#62)	22	$a^0a^0c^-$	<i>I</i> 4/mcm (#140)
11	$a^+a^-a^-$	<i>P</i> nma (#62)	23	$a^0a^0a^0$	<i>P</i> m-3m (#221)
12	$a^-b^-c^-$	F-1 (#2)	-	-	-

The orthoferrites and many of the materials studied within this thesis adopt the crystal structures defined by the space group $Pnma$, tilt system 10, $(a^+b^-b^-)$. This means that there are two independent tilts of differing magnitudes: an anti-phase and an in-phase tilt.

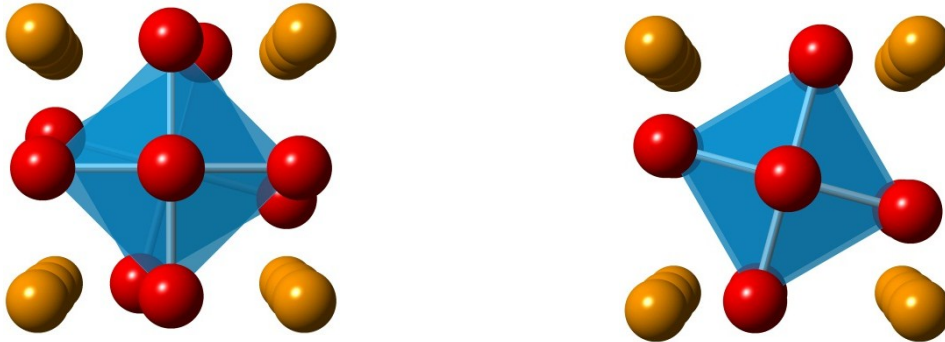


Figure 1.2: The anti-phase, -, (left) and in-phase, +, (right) tilts are shown, with the octahedra rotated around a pseudo-cubic axis by 15°.

In the $Pnma$ setting, with a unique b -axis, the in-phase tilt is about the b -axis and the anti-phase tilt along the $[101]$ plane of the $Pnma$ unit cell.

Typically, the orthoferrites are reported as $Pbnm$, which is an alternate setting to $Pnma$. The transformation between the two settings is simple and can be performed by following the following matrix:

$$\begin{pmatrix} 0 & 1 & 0 \\ 0 & 0 & 1 \\ 1 & 0 & 0 \end{pmatrix} \begin{pmatrix} 0 \\ 0 \\ 0 \end{pmatrix}$$

This means that the unit cell is not displaced and the axis set is switched such that the lattice parameters a, b, c transforms to c, a, b .

1.2 Crystallography⁷⁻¹⁰

Crystallography has been used to describe the structure of the materials presented within this thesis. A crystal is a solid comprised of a regular three-dimensional repeating collection of atoms or groups of atoms. This arrangement of atoms can be described mathematically in the form of a crystal lattice *i.e.*, an infinite three-dimensional mathematical array of repeating points. This array can be described simply by translating a smaller repeating unit or unit cell, which is an imaginary parallel-sided region that is then displaced to generate the lattice.

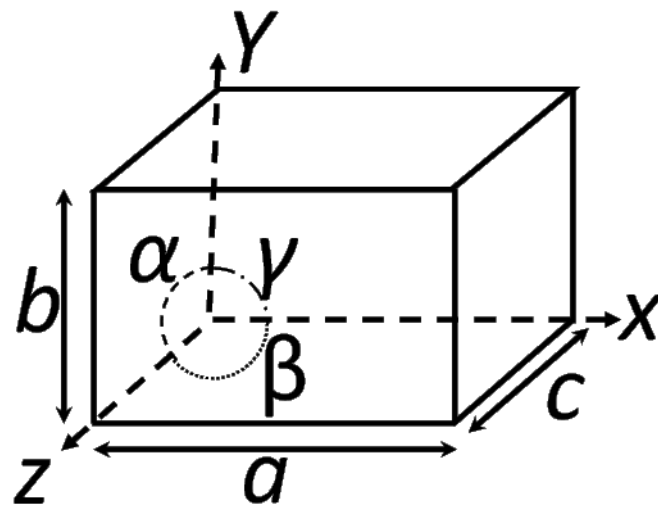
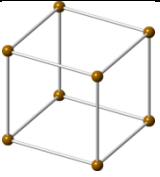
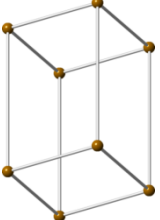
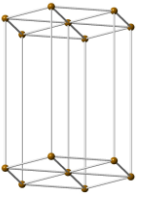
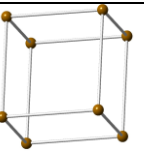
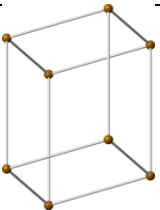
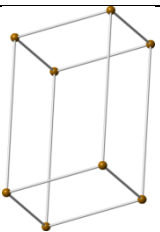
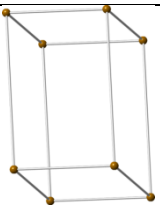


Figure 1.3: Unit cell showing lengths a , b , and c and angles (α , β , γ)

and vectors x , y , z

There are seven possible parallelepiped unit cells, given by the possible permutations in varying unit cell dimensions and angle. The unit cell is given lengths a , b , and c and angles α , β , γ . The crystallographic systems are more formally described by the essential symmetry operations tabulated in Table 1.2 (see section 1.2.1 for the symmetry operations).

Table 1.2: The 7 crystal systems

Crystal System		Axial representation	Essential symmetry elements
Cubic		$a = b = c, \alpha = \beta = \gamma = 90^\circ$	Four 3-fold rotational axes
Tetragonal		$a = b \neq c, \alpha = \beta = \gamma = 90^\circ$	One 4-fold rotational axis
Hexagonal		$a = b \neq c, \alpha = \beta = 90^\circ, \gamma = 120^\circ$	One 6-fold rotational axis
Trigonal/ Rhombohedral		$a = b = c, \alpha = \beta = \gamma \neq 90^\circ$	One 3-fold rotational axis
Orthorhombic		$a \neq b \neq c, \alpha = \beta = \gamma = 90^\circ$	Three perpendicular 2 fold axes and/or mirror planes
Monoclinic		$a \neq b \neq c, \alpha = \gamma = 90^\circ \beta \neq 90^\circ$	2-fold rotational axes or mirror plane
Triclinic		$a \neq b \neq c, \alpha \neq \beta \neq \gamma \neq 90^\circ$	None

The unit cell contains atom positions or groups of atoms, a basis, which is described in relation to the unit cell as fractional coordinates of the axis length a , b , and c . Changing the number of lattice points or positions within the unit cell gives rise to a number of different crystal lattices commonly labelled with the letters P , I , F , and C .

The primitive unit cell (P) has one lattice point within the cell, typically depicted on the corners of the unit cell or at its centre. Lattice points can be fractional depending on whether they reside wholly or partially in the unit cell, so the corners count as $\frac{1}{8}$. ($\frac{1}{8} \times 8 = 1$). By translating this cell *i.e.*, displacing the unit cell by a defined amount along its axis, the other cells can be generated.

The body-centred cell (I) can be generated by translating the primitive unit cell by $(x + \frac{1}{2}, y + \frac{1}{2}, z + \frac{1}{2})$ such that it has two positions, depicted on the corners and centre of the unit cell. The C -centred cell differs by having the position on the centre of opposite faces of the unit cell as opposed to the centre of the body centred cell. It is generated by translating the primitive cell by $(x, y + \frac{1}{2}, z + \frac{1}{2})$. Finally, the face centred (F) cell has four positions that are located on the corners and at the centre of all faces of the unit cell. The different lattices are shown below in Figure 1.4:

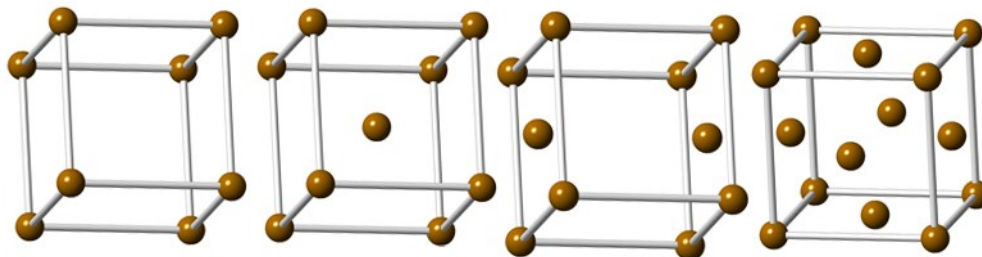


Figure 1.4: Primitive, Body centred, C-centred and Face centred unit cells.

The seven crystal systems are combined with the four crystal lattices to generate 14 Bravais lattices, shown in table 1.3:

Table 1.3: The 14 Bravais lattices.

Crystal System	Bravais Lattice
Cubic	P,I,F
Tetragonal	P,I
Hexagonal	P
Trigonal /Rhombohedral	P/R*
Orthorhombic	P,I,F,C
Monoclinic	P,C
Triclinic	P

*The symbol R is normally used to describe the centred unit cell.

The application of point group symmetry elements results in 32 crystallographic point groups, which are combined with the Bravais lattices and other translational symmetry elements, giving 230 space groups. The point group symmetry elements and translational elements are described in the following sub-section.

1.2.1 Symmetry operations^{7,9}

There are a number of possible symmetry operations that can be performed on a discrete object or molecule: rotation, reflection, and inversion. These are the point symmetry operations – where the applied symmetry operation can be performed such that the object appears unchanged by that operation.

After rotating an object by less than 360° about an axis, if the object appears unchanged, it has rotational symmetry about that axis. Rotational symmetry is denoted by the order, n , which is the number of times that the object can be rotated about the axis before reaching its starting position ($360^\circ/n$).

Reflections occur across a mirror plane; all objects are translated to the equivalent positions given by a mirror, m , *i.e.*, a mirror along y result in x, y, z giving $x, -y, z$.

An inversion is the operation where an object is translated through a point or inversion centre. If the object has an inversion centre, then moving all points on the object an equal distance through the centre will result in the object appearing unchanged. An inversion centre at the origin results in x, y, z going to $-x, -y, z$. It is given the symbol $\bar{1}$. This leads on to improper symmetry, which combines a rotation of order n with an inversion. Rotoinversions are given the symbol \bar{n} where $n = 2, 3, 4$ or 6 .

In addition to the point symmetry operations there are translational symmetry operations that can be performed – screw axes and glide planes. A glide plane combines a mirror plane with a translation parallel to the plane. They are given the symbols a, b, c, n , and d . The symbols a, b, c represent a reflection in the plane followed by a translation by $\frac{1}{2}$ of the length a, b, c , respectively. The n -glide after the reflection translates the object by $\frac{1}{2}$ along two of the cell lengths – *i.e.*, a diagonal bisecting the crystallographic axis. The d -glide translates the object by $\frac{1}{4}$.

The screw axis combines a rotation and simultaneous translation. Allowed rotations are $1, 2, 3, 4$, and 6 ; others are prevented by three-dimensional periodicity of the crystal lattice. The object is translated along the axis by a fraction given by the subscript. The denominator is given by the order of the rotation and the numerator is given by the subscript *i.e.*, 2_1 axis translates by $\frac{1}{2}$.

1.2.2 Miller indices and planes

It can be useful to consider a crystal lattice as a series of layers or a series of equally spaced parallel planes of atoms. These planes are referred to as Miller planes and are denoted by the integers h, k , and l , known as Miller indices. A Miller index is based on the fractional coordinate at which the plane intercepts the unit cell vectors a, b , and c (Figure 1.3). The reciprocal of the fractional intercept point is taken, giving an integer value. In defining a plane, the three Miller indices are presented in parenthesis as (h,k,l) .

1.3 Symmetry and magnetism^{11, 12}

Magnetic dipoles can cooperatively align within a system and possess long-range magnetic order. This magnetic order can be described using symmetry using one of two different approaches: Shubnikov symmetry, which describes commensurate magnetic structures; and group representational analysis.¹³

A space group assigned to a crystal structure should reflect all the physical properties and the respective directions relative to which the properties are observed. On the introduction of magnetic order, the symmetry of the space group may have to change to reflect the magnetic symmetry. Shubnikov (also called Heesch) symmetry does this by introducing “colour” to symmetry operations. Often, a spin direction is considered to be a polar vector with a magnitude and a direction; however, within a magnetic system an axial current loop has to be described that is 90° to that of the polar axis. Operations such as a centre of inversion do not affect the direction of the current loop (Figure 1.5).

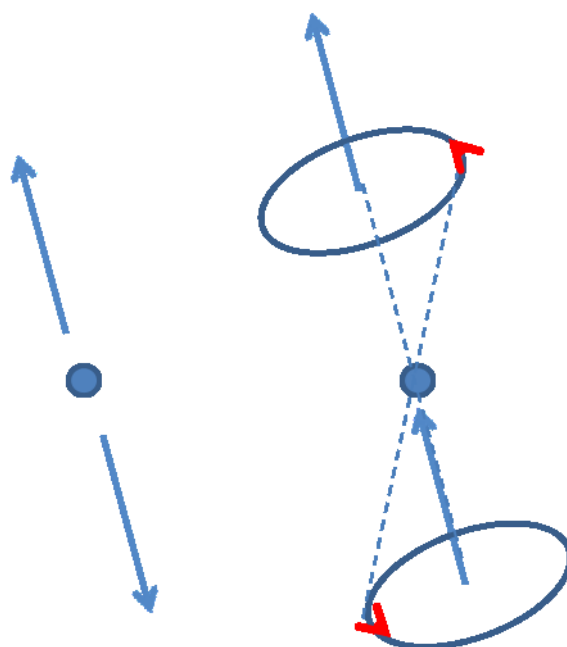


Figure 1.5: Inversion centre applied to a polar and axial vector showing an inversion in the polar vector and no change in the anticlockwise axial orbital direction.

Therefore, the “colour” extension to the space group symmetry operations determines if the operation flips the direction of the magnetic spin and is represented by the addition of primes to the space group e.g. $Pn'ma'$. The prime after the symmetry operator indicates that the symmetry operation is obeyed followed then by flipping the spin direction. It is sometimes referred to as in the literature as “time reversal” or “anti” operators. In crystallographic software such as GSAS the primed operator is represented by the red spin operator and black represents the unchanged operation.¹⁴

1.4 Magnetic order and Shubnikov symmetry

The alignment of magnetic moments and their arrangement in space creating long-range order is responsible for the overall observed magnetic properties of a bulk material. There are a number of different types of ordering based on how the moments are aligned. Applied external magnetic fields affect the alignments of the moments. Types of magnetism include paramagnetic, ferromagnetic, antiferromagnetic and ferrimagnetic order.

Paramagnetism is a state in which magnetic moments are randomly aligned such that there is no net macroscopic magnetic moment in the absence of a magnetic field. In the presence of an external magnetic field, the atoms with an overall moment can align with the field and the material will obey Curie’s law where there will be a small net attraction showing linear behaviour to an applied field.

In ferromagnetic materials, the adjacent magnetic moments cooperatively align in parallel, such that there is a spontaneous net moment in the absence of a magnetic field. Ferromagnetic order occurs spontaneously in the absence of an applied field. On cooling a paramagnetic material through an ordering temperature known as the Curie temperature, T_c , the thermal energy is no longer greater than that of the interaction energies between moments, and the moments can align ferromagnetically.

In antiferromagnetic materials, the moments align in an antiparallel manner, such that there is no net magnetic moment. The moments align with respect to a given crystallographic direction, which may give rise to different unit cells that possess antiferromagnetic order (AFM). Ferrimagnetic order differs slightly as the moments are aligned antiparallel, but do not completely cancel resulting in a net magnetic moment.

Figure 1.6 shows representations of the different types of magnetic order:

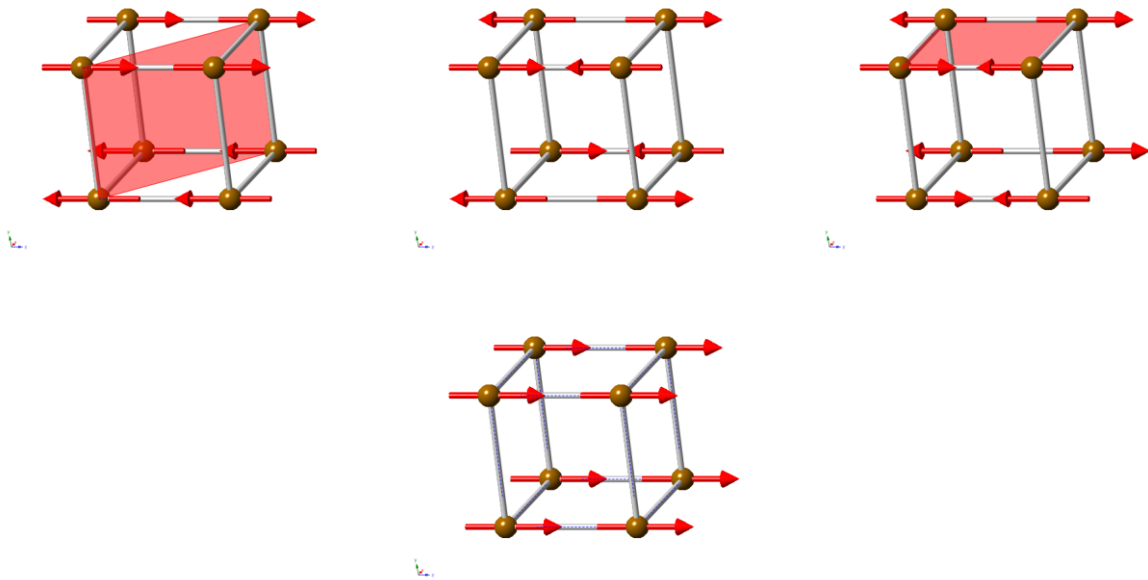


Figure 1.6: Magnetic unit cells: The A-type, G-type, C-type, and F-type magnetic cells are shown left to right. The AFM plane is shown for the A-type and C-type magnetic cells.

An example of the G_z type magnetic unit cell ($Pn'ma'$), with the time reversal spin operators is show in Figure 1.7:

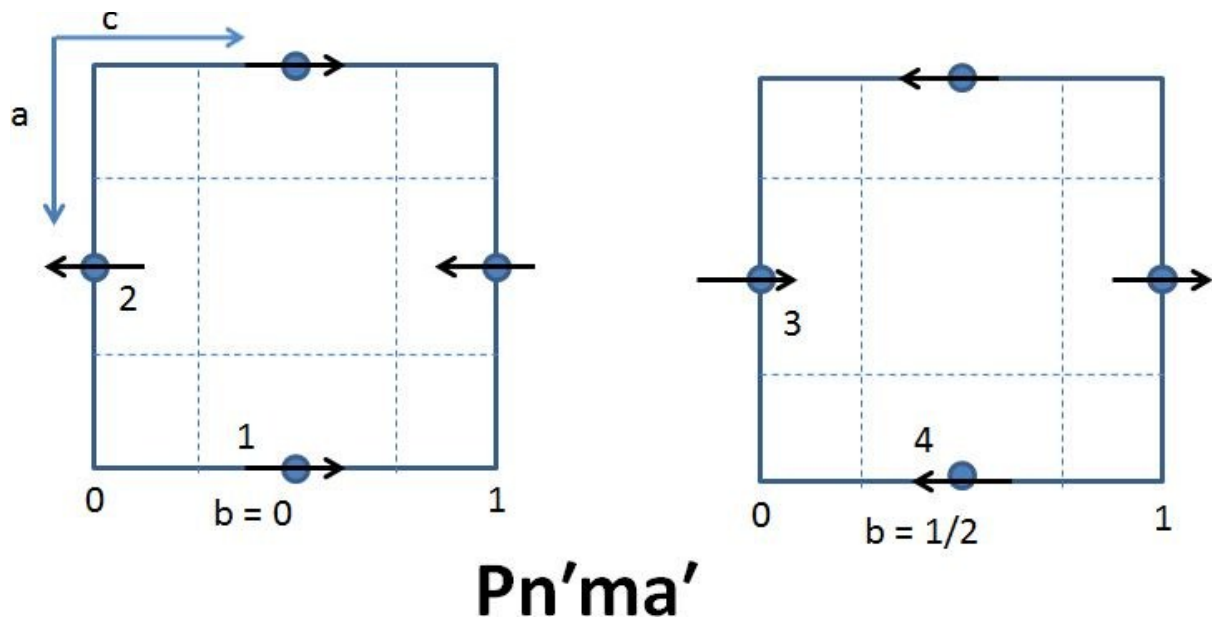


Figure 1.7: G_z type magnetic cell ($Pn'ma'$) showing the direction of the moments and selected spins with their operators.

Atomic positions

- | | |
|----------------------------------|----------------------------------|
| 1. $0, 0, \frac{1}{2}$ | 2. $\frac{1}{2}, 0, 0$ |
| 3. $\frac{1}{2}, \frac{1}{2}, 0$ | 4. $0, \frac{1}{2}, \frac{1}{2}$ |

As a general rule, as an electron has a moment with a perpendicular current loop it can be considered as a complex object (*i.e.*, not a single point) when a symmetry operation is applied. Donnay *et al.* show that when the mirror plane is parallel to the electron orbit (*i.e.*, perpendicular to the moment) the direction of the current loop does not change and the operation does not flip the moment.¹² However, this is not true if the mirror plane is parallel to the moment and the direction of the moment switches.

In the case of $Pn'ma'$, only the a-glide is perpendicular to the moment, so

a-glide at $z = \frac{1}{4}$ from 1 to 2 **doesn't** change orbit direction, and is therefore primed

n-glide at $x = \frac{1}{4}$ from 1 to 3 **does** change orbit direction, and is therefore primed

m-plane at $y = \frac{1}{4}$ from 1 to 4 **does** change orbit direction, and therefore isn't primed

1.5 Electroceramic materials

Electroceramics are a class of materials in which the physical properties primarily of interest relate to the electrical behaviour of the material. In addition to their electrical properties, they may also exhibit other interesting properties characterised by their optical and magnetic behaviour.

Electrical properties of particular interest relate to the polarisability and electrical conductivity of the materials. Polarisation is a measure of how easily an external electrical field, E , is able to perturb the distribution of electrical charge. This may arise from the displacement of the electronic cloud, ionic displacements of the anions and cations, reorientation of polar molecules or space charge. The polarisability, α , of a material is defined in Equation 1.2 where p is the overall dipole moment.

$$\alpha = \frac{p}{E} \quad \text{Equation 1.2}$$

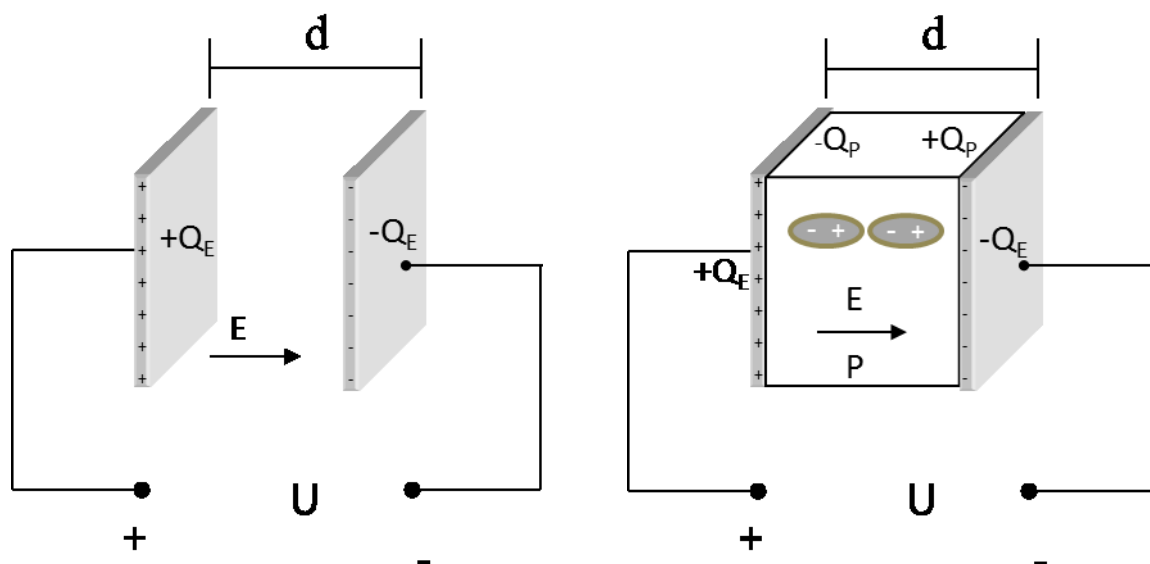


Figure 1.8: a) A parallel plate capacitor comprised of two plates separated by free space (left) and b) the equivalent parallel plate capacitor with dielectric medium (right).

An applied electrical potential, U , across parallel plates separated by a vacuum will create two oppositely charged electrode surfaces as shown in Figure 1.8. The separation of charge, Q , over the area of the electrode, A , creates an electrical field between the plates.

$$E = \frac{Q}{A} = \frac{U}{d} \quad \text{Equation 1.3}$$

The strength of the electric field is dependent on the separation between the electrodes, d , indicated in Figure 1.8 and the relationship with the applied potential as shown in Equation 1.3.

Figure 1.8 b) represents the case where an electrically homogeneous insulating material known as a dielectric is situated between the parallel plates. The externally applied electric field across the parallel plates will affect the electronic cloud and distribution of electrical charge in the dielectric. However, the electrical charge in an insulating material is not delocalised. Therefore, electrical dipoles within the material align parallel to the electrical field along a displacement vector, D , and produce a net polarisation. The displacement vector is comprised of two charge density terms, σ_E , and σ_P which relate to the contribution from the parallel plates and the dielectric, respectively.

$$D = \sigma_E + \sigma_P \quad \text{Equation 1.4}$$

The dipoles align opposing the electrical field, which means the charges on opposing plates are shielded and the net effective charge on the electrodes is reduced such that the total net charge, Q_N , is:

$$Q_N = Q_E - Q_P \quad \text{Equation 1.5}$$

The rearrangement of Equation 1.5 shows that the total free electrical charge on the electrode, Q_E , is enhanced by Q_P . Materials have different susceptibilities, χ_e , to an external electrical field, so the contribution of charge stored due to the polarisation of the dielectric also varies. Equation 1.6 gives the total polarisation, P , relative to that of a vacuum where the permittivity of free space is ϵ_0 .

$$P = \epsilon_0 \chi_e E \quad \text{Equation 1.6}$$

For a linear dielectric, the charge held on the electrode varies proportionally to the polarisation therefore; the charge density of a capacitor is given by:

$$D = \epsilon_0 E + P = \epsilon_0 E (1 + \chi_e) \quad \text{Equation 1.7}$$

The two contributions to the displacement vector can be simplified by collecting the terms shown in Equation 1.4. This can be simplified further by using a material constant known as

the dielectric constant. The dielectric constant, k , is usually expressed as a relative permittivity, ϵ_r , to that of a vacuum ($\epsilon_r = (1 + \chi_e) = \frac{\epsilon}{\epsilon_0}$ ϵ_0 : $8.854 \times 10^{-12} \text{ Fm}^{-1}$) and is frequency dependent. Measured at zero frequency the dielectric constant is the static permittivity, ϵ' . Alternatively, there is the absolute permittivity $\epsilon = \epsilon_0 \epsilon_r$.

1.6 Polar dielectrics^{15,16}

So far, the description of a dielectric material has described linear dielectrics where distortions in the electronic cloud create a polarisation. However, there are a number of different types of dielectric material, based on the absence of a centre of symmetry. These are the polar dielectrics, which allow for ionic displacements within a specific crystallographic direction. The polar dielectrics are piezoelectric, pyroelectric, and ferroelectric materials.

Piezoelectric materials are named after the Greek *piezen* to press and are non-centrosymmetric materials which exhibit an electrical polarisation when subjected to a mechanical force.¹⁶ Piezoelectrics do not necessarily have a polar space group, however they are allowed to develop a polarisation along an axis when subjected to a mechanical stress; this is due to the absence of an inversion centre. The piezo effect occurs due to the anisotropic displacement of ions along this displacement vector resulting in a net polarisation. The electrical charge developed is proportional to the applied force.¹⁵ There is also the converse effect known as the motor effect where an electrical field will displace ions creating a macroscopic strain.

Pyroelectric materials require a polar axis when not subjected to an external stress. Therefore, this effect will only occur in materials with one of the 10 non-centrosymmetric *and* polar space groups. The pyroelectric effect is a temperature dependent effect whereby, uniformly heating the material results in the development of an electrical dipole due to a change in the relative positions of the cation and anions. Typically, this is due to an off centring of cations within the lattice relative to the centre of the unit cell. The summation of these dipoles gives a spontaneous polarisation throughout the material on heating.

Ferroelectrics are a subset of pyroelectric materials and similarly exhibit a spontaneous polarisation in the absence of an applied external electric field. However, the applied

electric field in a ferroelectric can reversibly change the direction of the spontaneous dipole moment and magnitude of the polarisation up to a saturation limit, P_s . In the absence of an external field, there is a remanent polarisation, P_r , the sign of which is dependent on the previously applied field. This creates hysteretic behaviour, as shown in Figure 1.9.

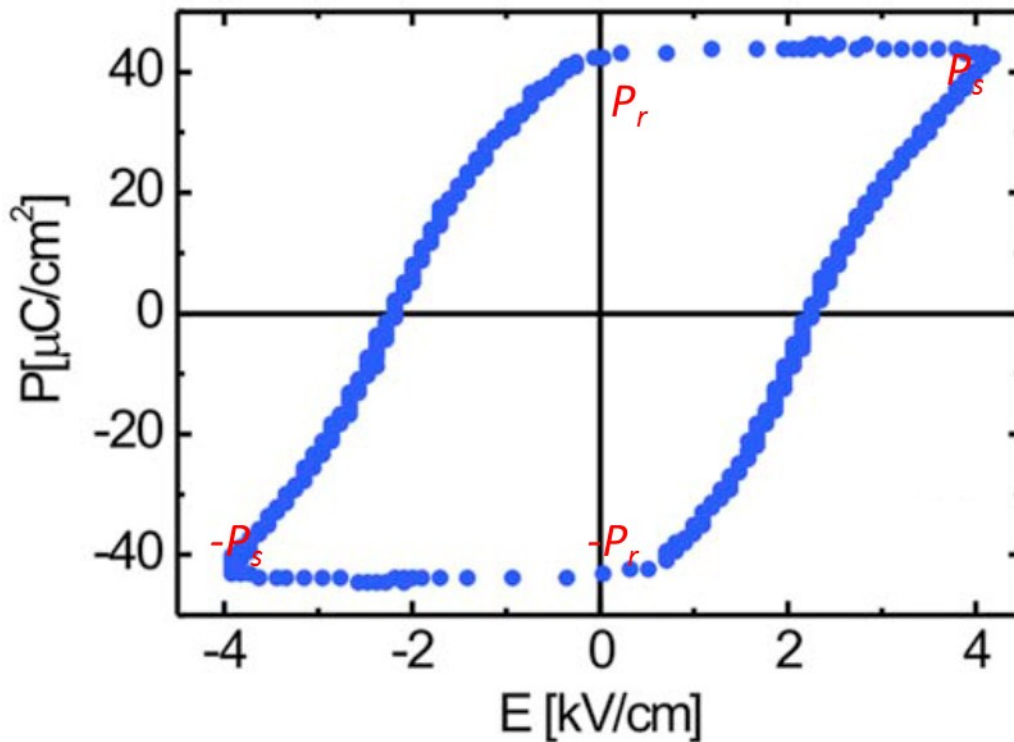


Figure 1.9: P - E hysteresis loop showing the remanent polarisation, P_r , and saturation limit P_s in a ferroelectric material.

Adapted figure of BiFeO_3 P - E loop at room temperature 50 Hz¹⁷

This hysteresis loop is analogous to the loops observed in ferromagnetic polycrystalline samples (M - H loops) where on increasing a magnetic field, H , the magnetic moments of the domains will align with the field up to a limit, the magnetic saturation, M_s . On relaxing the field, the alignments can partially relax, resulting in a similar remanent magnetisation, M_r , as the field strength cycles.

The descriptions of the polar dielectrics show that the classes are related and dependent on increasing symmetry and energetic considerations. Therefore, polar dielectrics can be represented in terms of sets shown in Figure 1.10.

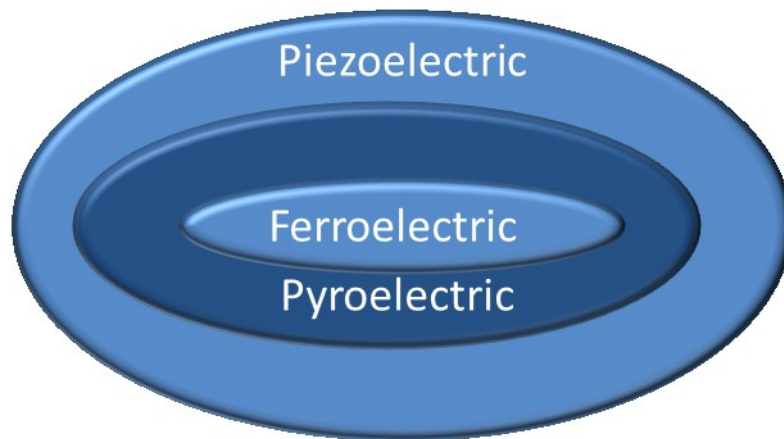


Figure 1.10: Polar dielectrics: A Venn diagram showing the relationship between piezoelectric, pyroelectric, and ferroelectric materials.

1.7 Multiferroic materials

The most common types of ferroic behaviour an electroceramic may exhibit are summarised below:

- i. **Ferroelectricity:** Spontaneous polarisation (P) that is switchable by an applied electric field (E).
- ii. **Ferromagnetism:** Spontaneous magnetisation (M) that is switchable by an applied magnetic field (H).
- iii. **Ferroelasticity:** Spontaneous strain (ϵ) switchable under applied stress (σ).

If a material possesses more than one of these properties within the same phase, the material is classed as a multiferroic. Changes in the physical properties arise due to structural changes. If the structural changes and chemical nature of the material are complementary, the physical properties may be coupled. Applying an electrical field across an electroceramic therefore, may change the material's shape or the direction of the spontaneous magnetisation. The coupling of two or more of the summarised ferroic properties, which are within the same phase of a material, are outlined in Figure 1.11.

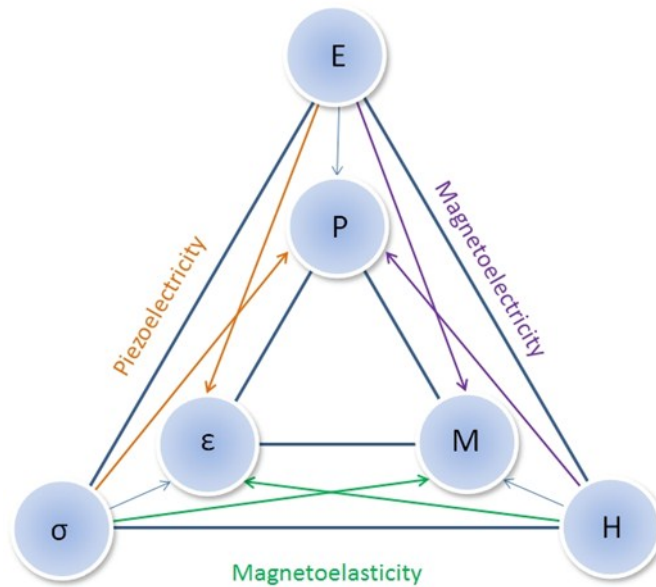


Figure 1.11: Diagram showing the relationships between various ferroic properties.¹⁸

Coupled properties are of interest for device applications and have been the subject of a number of reviews.¹⁹⁻²² In a piezoelectric material, for instance an electric field influences the strain creating a physical deformation used in actuators. Alternatively, an applied pressure creates an electrical polarisation that can be used in applications such as sonar, microphones, and energy harvesting. Magnetoelastic materials have found similar applications in sensing devices.

The final coupled property is the magnetoelectric effect in which a spontaneous magnetisation is switchable with an electric field or a magnetic field can switch the electrical polarisation. Potential applications include data storage, spintronics, and microelectronics.^{17, 23}

As pointed out by Hill *et al.*, there are very few magnetic ferroelectric materials, in part due to the requirement of unpaired electrons (typically *d*-electrons) for magnetism and a preference for d^0 , e.g. BaTiO₃ Ti⁴⁺, with respect to the ferroelectric properties such that the material is more likely to be insulating. In addition, the coupling between the ferroelectric and ferromagnetic state is often too weak for applications and needs to be enhanced.²⁴ Promising candidates with the perovskite structure involve the presence of a lone pair e.g. Bi³⁺ and Pb²⁺.¹⁷

1.8 Multiferroic BiFeO₃

BiFeO₃ is currently the only known room temperature multiferroic oxide and is therefore a good candidate for further research due to its high ferroelectric ($T_c \sim 810 - 830$ °C)^{25, 26} and antiferromagnetic ($T_N \sim 370$ °C) ordering temperature.²⁷

However, producing high purity single phase BiFeO₃ is not without its problems. BiFeO₃ is prone to parasitic secondary phases that nucleate around the grain boundaries.²² Potential secondary phase include sillenite - Bi₂₅FeO₃₉ and mullite - Bi₂Fe₄O₉ shown in the phase diagram produced by Palai *et al.* (Figure 1.12).²⁸

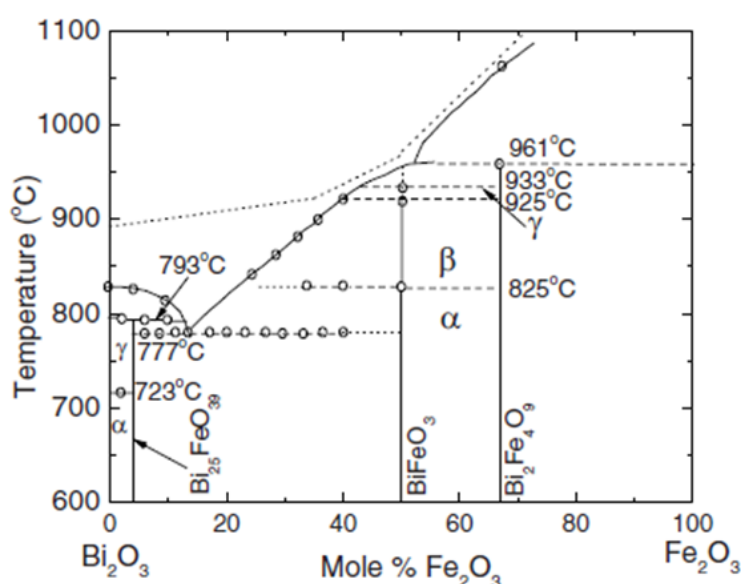


Figure 1.12: Phase diagram of the Bi₂O₃-Fe₂O₃ solid solutions. The α , β , and γ phases are rhombohedral, orthorhombic, and “cubic”, respectively.²⁸

The dotted line above liquidus shown in Figure 1.12 represents the approximate temperature where the volatility of Bi₂O₃ becomes a problem. Synthesis of samples above this line may result in non-stoichiometry due to bismuth loss and decomposition into secondary phases. Valant *et al.* describe in detail about the influences on the secondary phases suggesting that the purity of the starting materials can strongly influence the composition of product.²⁹ Small amounts of impurities such as Ti⁴⁺ on the B-site can dramatically affect the phase diagram and reduce the amount of Bi₂Fe₄O₉.²⁹ Other impurity ions such as Al³⁺ can promote secondary phases.²⁹ These effects are dependent on which secondary phase the impurity ion favours.

The detection of impurity phases using standard lab based analysis such as X-ray diffraction (XRD) can be difficult owing to the relative detection limits of Bi^{3+} and Fe^{3+} , due to their different scattering factors (based on atomic number). Consequently, $\text{Bi}_2\text{Fe}_4\text{O}_9$ is harder to detect than BiFeO_3 by XRD. In addition, as demonstrated in chapter 3, the detection of secondary phases such as hematite Fe_2O_3 using scanning electron microscopy is difficult without the aid of backscattered electrons.

The phase diagram, Figure 1.12, shows that BiFeO_3 can exist potentially as one of at least three phases before decomposition – below T_c a rhombohedral α phase exists, which transforms to an intermediate β orthorhombic phase at elevated temperatures between 830 – 925 °C, and finally at high temperature a γ phase exists between 925 – 933 °C before decomposition.²⁸

The low temperature rhombohedral phase adopts the space group $R3c$ with the lattice parameters $a_H = 5.58 \text{ \AA}$, $c_H = 13.867 \text{ \AA}$ (in the hexagonal setting) at room temperature.^{23, 30} The BiFeO_3 structure at room temperature can be described as two distorted perovskite blocks connected along the pseudo-cubic $[111]$.²¹ The octahedra are tilted around this axis by about 13.8° ²¹ which is consistent with the $[\bar{a}\bar{a}\bar{a}]$ tilt system. The Fe^{3+} site displaces away from the centre of the octahedra and there is a large displacement of the Bi^{3+} relative to the FeO_6 octahedra. This means that the bulk $R3c$ phase is susceptible to developing a polarisation and has been found to be ferroelectric with a polarisation of $P_s \approx 40 \mu\text{Ccm}^{-2}$ at room temperature ($E_{\text{max}} \sim 4 \text{ kVcm}^{-1}$ see Figure 1.9).¹⁷ These measurements can be difficult to obtain due to the requirement of high poling potentials and low leakage currents. In carefully prepared samples, BiFeO_3 is an indirect band gap semiconductor with an activation energy associated with the bulk of the $R3c$ phase *circa* 1.0 eV. This band gap falls above T_N to around 0.6 eV. The direct band gap has been calculated *circa* 2.8 eV.³¹

A number of authors have studied the magnetic structure in BiFeO_3 .³²⁻³⁴ The $R3c$ phase has a G-type magnetic cell with a incommensurate cycloidal spin with a repeating period of $\sim 620 \text{ \AA}$.³⁴ The spins are not perfectly antiparallel due to a weak canting moment caused by magnetoelectric coupling to the polarisation.²² This means that the $R3c$ phase is weakly antiferromagnetic with a propagation vector along the $[110]$ direction.

A representation of the cycloidal spin, Figure 1.13, shows the magnetic propagation vector 90° to that of the polarisation:

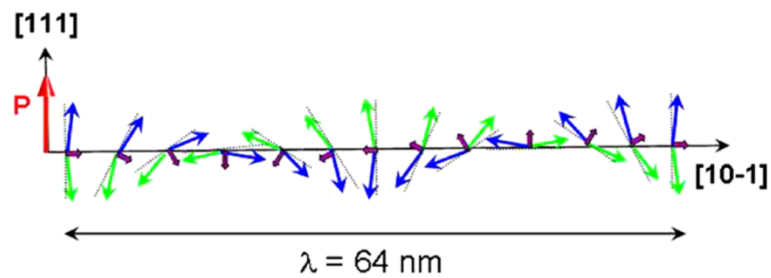


Figure 1.13: The canted antiferromagnetic spins are shown with the blue and green arrows give a resultant magnetic moment in purple. The net magnetic moments average to zero over the period of the cycloidal rotation. The polarisation vector is shown in red and the cycloidal propagation vector is shown in black $[10\bar{1}]$.³⁰

On heating BiFeO_3 , the α - phase transforms to a paraelectric orthorhombic ($Pbnm \ a^-a^-b^+$) β phase with a $\sqrt{2} a_p \times \sqrt{2} a_p \times 2 a_p$ unit cell, confirmed using powder neutron diffraction (PND).³⁵ The lattice parameters at 830°C are $a = 5.613 \text{ \AA}$, $b = 5.647 \text{ \AA}$, $c = 7.971 \text{ \AA}$.³⁵ At the ferroelectric paraelectric transition, Arnold *et al.* report an abrupt drop in unit cell volume, a gradual change in the Fe-O bonds with the lengths become effectively equivalent and there is a decrease in the octahedral rotation with decreasing cation displacements.

Prior to this work by Arnold *et al.*, in part due to decomposition and secondary products, other phases have been suggested, for example, tetragonal, $I4/mcm$ (based on first principle calculations)³⁶ rhombohedral, $R\bar{3}C$,³⁷ and monoclinic, $C2/m$ ³⁶ and $P2_1/m$ (based on high temperature XRD).³⁸ However, as pointed out by Catalan *et al.*, on the removal of the ferroelectric polarisation, which is a significant influences the structure, it adopts the same GdFeO_3 structure as the orthoferrites which aren't influenced by a lone pair - this probably means it is correctly assigned as $Pbnm$.²²

The nature of the γ phase is still controversial. Palai *et al.* have suggested that the γ phase is cubic.²⁸ However, more recent work by Arnold *et al.* (using PND), suggests that the phase transformation from the β $Pbnm$ phase to the γ phase is an insulator-metal transition, where the γ phase remains orthorhombic, space group $Pbnm$.³⁹ Decomposition of the BiFeO_3 impeded a definitive identification of the space group. Attempts have been made to study BiFeO_3 as a function of pressure, which has equally left the phase sequence remarkably unresolved.²²

1.9 Rare earth doped BiFeO₃

An alternative approach to investigate the high temperature phases is chemical doping. Doping BiFeO₃ by substituting volatile Bi³⁺ with rare earth elements such as La³⁺ has been shown to improve the thermal stability and electrical properties of the perovskite phase. The ionic radius of Bi³⁺ (Bi^{3+ VIII}: 1.17 Å) is similar to that of La³⁺ (La^{3+ VIII}: 1.16 Å)⁴⁰ such that the effect of doping will probably be dominated by the presence (or absence) of the lone pair which is responsible for the ferroelectric nature of BiFeO₃. Doping with La³⁺ is therefore more likely to favour the stability of the higher temperature phases observed in BiFeO₃ *e.g.* GdFeO₃ structure (*Pbnm*). This has been shown with recent research into La-doped BiFeO₃, where a complicated series of phase transitions has been observed.⁴¹

Doping with other rare earth elements such as Nd³⁺ (Nd^{3+ VIII}: 1.109 Å) means the average ionic radius of the A-site is smaller than the Bi³⁺, which results in a more significant contribution based on the relative differences in the ionic radii. This may favour the orthorhombic structure based on Goldschmidt's tolerance factor (Equation 1.1).

1.10 Bi_{1-x}La_xFeO₃

The investigation of phases within this series is complicated by the presence of multiple thermodynamically stable phases, incommensurate structures and impurity phases. These complications result in debate and disagreement about the boundaries of the phase sequence.^{41, 42} Rusakov *et al.* observed the following phase sequence (under ambient conditions) as a function of composition for samples prepared by solid-state methods:⁴¹

$R3c$ ($0 < x < 0.1$) \rightarrow '*Pnam*' ($x = 0.18$) \rightarrow incommensurate '*Imma*' ($0.19 < x < 0.30$) \rightarrow *Pnma* ($x > 0.5$) (Mixed phase regions exist between the specified compositions)

Troyanchuk *et al.* are reasonably in agreement with Rusakov *et al.* However, they suggest that the *R3c* range extends to $x \leq 0.15$ which is then followed by a phase mixture of *R3c* and the *Pnam*, PbZrO₃-like phase ($x = 0.16$, ratio 1:2 at room temperature).⁴³ This antipolar PbZrO₃-like, orthorhombic phase was first reported by them and exhibits a unusual isothermal polar-antipolar structural transition rarely observed in a ceramics.⁴⁴ Composition close to the *R3c* to *Pnam* morphotropic phase boundary can gradually transform over a period of time to the orthorhombic phase at room temperature. This phase transition is

pressure induced relieving stress within the ceramic. At $x = 0.19$, the phase mixture is mainly incommensurate “*Imma*”, which is observed up to $x > 0.45$. At $x = 0.5$, the *Pnma* phase is observed at ambient conditions, which is in agreement with Rusakov.⁴³ The series of phase mixtures has been found to be independent of synthesis conditions using the ceramic method.⁴²

Density functional theory (DFT) calculations, corroborated by experimental evidence, suggest that within the *R3c* phase, the degree of the ferroelectric off-centering along the *c*-axis of the unit cell (hexagonal setting) is reduced with increasing lanthanum content.⁴⁵ This influences the ferroelectric properties, significantly reducing the ferroelectric polarisation with doping concentration. However, it does allow samples to sustain higher electric fields by reducing leakage currents.⁴⁵

The ‘*Pnam*’ phase has a PbZrO_3 -like antipolar superlattice, with a $\sqrt{2} a_p \times 2\sqrt{2} a_p \times 4 a_p$ unit cell, relative to the aristotype cubic perovskite (a_p). The antipolar PbZrO_3 -like phase ($x = 0.185$ 92.5%) has been studied with PND as a function of temperature.⁴⁴ This study eliminated the possibility of impurity phases by thermally inducing the phase change to *Pnma* (700°C), removing the satellite peaks that could be associated with an incommensurate structure.⁴⁴ In subsequent papers, the suggestion of the *Pna2₁* space group was considered based on electron diffraction experiments.⁴¹ A few different space groups have been suggested for this phase and it usually depends on the sensitivity of the technique. Troyanchuk *et al.* best describe the issue referring to the NaNbO_3 -type tilting which “is not strong and/or sufficiently ordered to give clear superlattice reflections in conventional X-ray or neutron diffraction experiments”- accordingly the space group *Pbam* can be used.⁴⁴ They base their work on $\text{Bi}_{1-x}\text{Nd}_x\text{FeO}_3$, which exhibits a similar intermediate phase in its phase sequence.^{46, 47}

The ‘*Imma*’ unit cell approximates to $\sqrt{2} a_p \times 2 a_p \times \sqrt{2} a_p$ superstructure This incommensurate *Imma* structure is based on the $x = 0.25$ composition, which has been solved using synchrotron powder X-ray diffraction (SPXRD).⁴¹ Rusakov *et al.* suggest it is incommensurate due to competing dipole-dipole interactions caused by antipolar Bi^{3+} displacements and octahedral tilting.⁴¹ The displacements were analysed using Rietveld refinement, with random displacements of the A-site cation off the *a*-axis mirror plane. They

reason that the displacement occurs due to the localisation of the Bi^{3+} lone pair requiring a strong short covalent bond to the axial oxygen positions.⁴¹ The Bi^{3+} and La^{3+} site were treated separately due to the absence of a lone pair associated with the La^{3+} . This was modelled with anisotropic refinements, suggesting a displacement along the b -axis.⁴¹

The $Pnma$ structure is the common GdFeO_3 -type structure, with a $\sqrt{2} a_p \times 2 a_p \times \sqrt{2} a_p$ unit cell. The GdFeO_3 structure is adopted by LaFeO_3 (typically refined in the alternate crystallographic setting $Pbnm$).⁴⁸⁻⁵⁰ LaFeO_3 is a canted G-type antiferromagnetic phase with a slightly off-axis component.⁴⁸

1.11 $\text{Bi}_{1-x}\text{Pr}_x\text{FeO}_3$

The praseodymium system shares some similarities with the lanthanum doped system, adopting the parent BiFeO_3 polar $R3c$ phase up to $x < 0.12$.⁴³ An isothermal structural transformation occurs in $x = 0.125$, where approximately 10% of the sample changes to an antipolar phase after 1 month.⁴³ XRD shows that a purely antipolar phase (refined as $Pnam$ $\sqrt{2}a_p \times 2\sqrt{2} a_p \times 4a_p$) exists within the compositional range $0.16 \leq x \leq 0.25$.⁴³ However, in more heavily doped samples ($x = 0.2 - 0.25$) the superstructure peaks have not been seen by diffraction, such that the PbZrO_3 $Pbam$ structure ($\sqrt{2}a_p \times 2\sqrt{2}a_p \times 2a_p$) can be used.⁴³ The absence of the incommensurate phase in heavier doped samples has been suggested to be due to the relatively lower ionic polarisability (given by Shannon) of Pr^{3+} compared to La^{3+} .^{40, 43} However, as Karimi *et al.* point out “ionic polarisability is directly proportional to ionic radius and therefore it is difficult to distinguish which of the crystallochemical factors is most important” with respect to the absence of the incommensurate phase.⁵¹ At higher doping, $x \geq 0.27$, the system can be refined as $Pnma$.

1.12 $\text{Bi}_{1-x}\text{Nd}_x\text{FeO}_3$

A number of different authors have studied $\text{Bi}_{1-x}\text{Nd}_x\text{FeO}_3$.^{46, 47, 52-54} Levin *et al.* have constructed a phase diagram observing the following series of transitions at room temperature: $R3c \rightarrow$ “ $Pnam$ ” PbZrO_3 -like $\rightarrow Pbnm$ ($Pnma$).^{46, 54} The phase transitions have been studied with a number of different techniques including electron diffraction, XRD and PND.^{46, 47, 54}

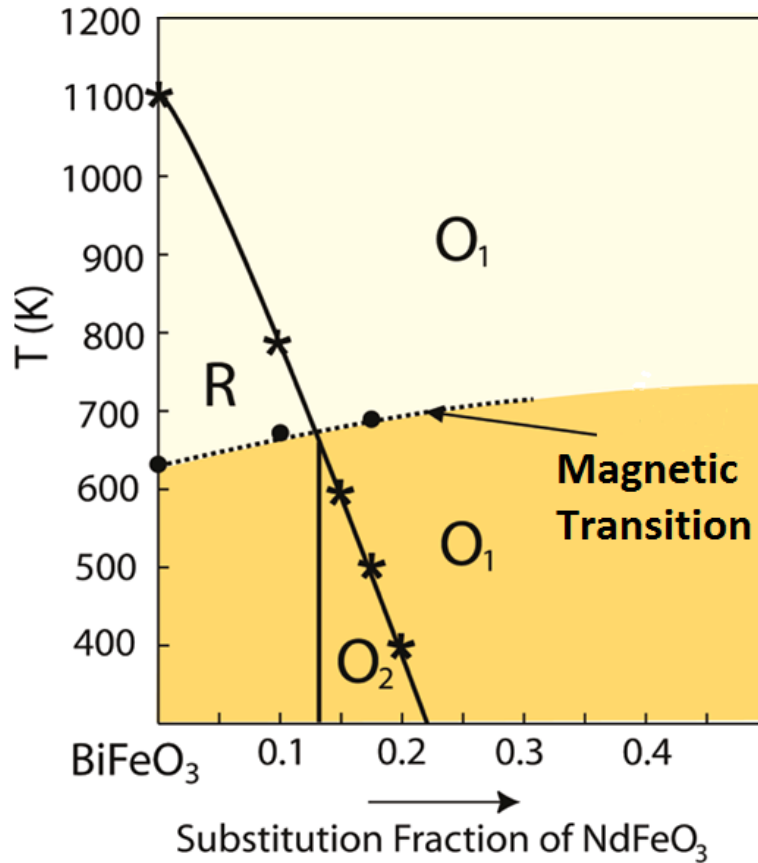


Figure 1.14: Phase diagram of $\text{Bi}_{1-x}\text{Nd}_x\text{FeO}_3$ indicating structural and magnetic transitions based on PND and magnetic measurements. The R phase is ferroelectric, O_1 phase is paraelectric, and O_2 phase is supposedly antiferroelectric (Figure adapted from Levin *et al.*)⁵⁴

Temperature dependent PND experiments of $\text{Bi}_{0.9}\text{Nd}_{0.1}\text{FeO}_3$ (BT-1 NIST) have revealed structural changes at the AFM rhombohedral ($R3c$) to orthorhombic paramagnetic $Pbnm$ boundary.⁵⁴ At the transition following the change in magnetic behaviour, a significant discontinuous drop in unit cell volume is observed. This is coupled with an increasing FeO_6 octahedral volume, and an increased anti-phase tilt.⁵⁴ This will decrease the A-site volume and presumably the average A-O bond length, as the balance between the magnetic and bonding contributions in the system changes with the loss of AFM order.

A similar structural change is observed (in $\text{Bi}_{0.85}\text{Nd}_{0.175}\text{FeO}_3$) with the $Pbam$ “ PbZrO_3 -like” to $Pbnm$ transition.^{46, 54} There is a reorientation of the dipoles with a similar accompanying drop in unit cell volume and increasing FeO_6 volume.^{46, 54}

This phase sequence contrasts with the lanthanum and praseodymium analogues, as there was no isothermal structural phase transition observed near the polar-antipolar phase boundary. The (in)commensurate *Imma* phase is also not observed.

1.13 $Bi_{1-x}Sm_xFeO_3$

The antipolar phase region narrows with decreasing ionic radius. In the samarium-doped system ($Bi_{1-x}Sm_xFeO_3$) the following phase ranges are observed: *R3c* ($x < 0.1$) \rightarrow “*Pnam*” ($x = 0.14$) \rightarrow *Pnma* ($x = 0.18$). Mixed phase regions exist between the specified compositions.⁴³

1.14 $Bi_{1-x}RE_xFeO_3$ $RE = Eu, Gd, Tb, Dy$

The stability of the anti-polar phase continues to decrease with the ionic radii of the rare-earth elements and polarisability. Troyanchuk *et al.* has reported compositional ranges for a series of elements (Eu: w , Gd: x , Tb: y , Dy: z) and suggest the following phase sequence limits:

R3c ($w \leq 0.09, x, y \leq 0.08, z \leq 0.075$) \rightarrow “*Pnam* $PbZrO_3$ -like”_{max} ($w, x: 0.12, y: 0.115$) \rightarrow *Pnma* ($w, x, y, z \geq 0.18$)

They report a small amount of the non-polar *Pnma* phase (circa 5%) is present in the *Pnam* $PbZrO_3$ -like phases.^{43, 55} In the $Bi_{1-z}Dy_zFeO_3$ series the “*Pnam*” phase was not detected.⁴³

Other authors has suggested that the “*Pnam*” phase does exist in the $Bi_{1-z}Dy_zFeO_3$ system.⁵⁶

1.15 Thesis overview

The focus of this thesis is on the synthesis, electrical characterisation, and structural origin of the physical properties of $\text{Bi}_{1-x}\text{RE}_x\text{FeO}_3$. Two systems have been studied doping, BiFeO_3 with lanthanum and neodymium ($\text{Bi}_{1-x}\text{RE}_x\text{FeO}_3$ RE= La, Nd).

Relevant experimental techniques are described in chapter 2, with particular attention on powder diffraction and ac-impedance. Data from these techniques has been analysed and presented in all subsequent results chapters. An outline of the synthesis conditions used to prepare samples *via* standard solid-state methods is also included within chapter 2.

Specific examples are highlighted in chapter 3 for $\text{Bi}_{1-x}\text{La}_x\text{FeO}_3$ and chapter 4 for the neodymium analogue. These chapters highlight changes in the bulk electrical properties, which are associated with isostructural atomic displacements within the respective orthorhombic perovskite phases (space group $Pnma$). These isostructural displacements occur due to a changing balance between magnetic properties and other bonding contributions in the respective systems as a function of temperature. This results in changes in the magnitude of the octahedral tilts, and more specifically A-site displacements, with corresponding changes in the unit cell parameters leading to phenomena such as negative thermal expansion and invariant lattice parameters *i.e.*, the invar effect.

Chapter 5 describes the effects of processing on the electrical properties of samples. An initial batch of the composition $\text{Bi}_{0.6}\text{La}_{0.4}\text{FeO}_3$ was used from which changes in the synthesis temperature and atmosphere in the second step of the reaction result in significant changes to the conductivity of the samples. Similar electrical behaviour is found at other compositions such as in $\text{Bi}_{0.75}\text{La}_{0.25}\text{FeO}_3$.

The thesis is concluded with a final section, chapter 6 which serves as an overview for the results chapters combing the conclusions reached in the individual results chapters and goes on further to suggest directions for future research into $\text{Bi}_{1-x}\text{RE}_x\text{FeO}_3$.

1.16 Aims and objectives

BiFeO_3 is a multiferroic material and a promising candidate for research owing to a high ferroelectric (high $T_C \sim 810 - 830 \text{ }^\circ\text{C}$)^{25, 26} and antiferromagnetic ($T_N \sim 370 \text{ }^\circ\text{C}$) ordering temperature.²⁷ Through further research, these physical properties may be utilised in devices. However, there are problems with synthesis of BiFeO_3 due to volatility of Bi_2O_3 , secondary phases and electrical conductivity due to non-stoichiometry and thermal metastability. Substitution of Bi^{3+} with non-volatile rare earth elements on the A-site ($\text{Bi}_{1-x}\text{RE}_x\text{FeO}_3$) will affect the physical properties and may reduce the electrical conductivity. A-site substitution will also affect the observed phase.

Therefore, the initial aims of the research were to investigate the electrical and structural phase transitions within $\text{Bi}_{1-x}\text{RE}_x\text{FeO}_3$ with the objective of creating a phase diagram. To investigate this with impedance spectroscopy predominantly single-phase insulating samples are required. Having single-phase samples also simplifies structural characterisation. Doping BiFeO_3 with lanthanum and neodymium were selected based on the RE^{3+} ionic radii and on the absorption and scattering cross section of the nucleus for PND experiments.

Therefore the initial aim is:

- Investigate the electrical and structural phase transitions within $\text{Bi}_{1-x}\text{RE}_x\text{FeO}_3$ – specifically with $\text{RE} = \text{La}$ and Nd

To achieve the primary aim the following objectives are required:

- Produce single-phase samples where possible for the $\text{Bi}_{1-x}\text{RE}_x\text{FeO}_3$ ($\text{RE} = \text{La}, \text{Nd}$) systems *i.e.*, where $\text{Bi}_{25}\text{FeO}_{39}$ and $\text{Bi}_2\text{Fe}_4\text{O}_9$ are not present.
- Produce electrically homogeneous samples
- Perform electrical characterisation of the samples
- Investigate potential structural transformations highlighted through the use of ac-impedance spectroscopy with powder neutron diffraction and other techniques, such that an understanding of the physical properties can be achieved.
- Develop a phase diagram based on information collected

1.17 References

1. V. M. Goldschmidt, *Naturwissenschaften*, 1926, **14**, 477.
2. N. W. Thomas, *Acta Crystallogr. Sect. B: Struct. Sci.*, 1996, **B56**, 16 - 31.
3. C. J. Howard and H. T. Stokes, *Acta Crystallogr. Sect. B: Struct. Sci.*, 1998, **54**, 782-789.
4. P. Woodward, *Acta Crystallogr. Sect. B: Struct. Sci.*, 1997, **53**, 32-43.
5. P. Woodward, *Acta Crystallogr. Sect. B: Struct. Sci.*, 1997, **53**, 44-66.
6. A. Glazer, *Acta Crystallogr. Sect. B: Struct. Sci.*, 1972, **28**, 3384-3392.
7. A. R. West, *Solid State Chemistry and Its Applications*, Wiley, Chichester, 1984.
8. L. E. Smart and E. A. Moore, *Solid state chemistry: an introduction. 3rd edition*, Taylor & Francis CRC Press, 2005.
9. V. Pecharsky and P. Zavalij, *Fundamentals of Powder Diffraction and Structural Characterization of Materials*, Springer US, 2005.
10. V. K. Pecharsky and P. Y. Zavalij, *Fundamentals of Powder Diffraction and Structural Characterization of Materials*, Springer US, 2009.
11. J. Cui, Q. Huang and B. H. Toby, *Powder Diffr.*, 2006, **21**, 71-79.
12. G. Donnay, L. M. Corliss, J. D. H. Donnay, N. Elliott and J. M. Hastings, *Phys. Rev.*, 1958, **112**, 1917-1923.
13. R. B. Von Dreele and J. Rodriguez-Carvajal, in *Powder Diffraction: Theory and Practice*, The Royal Society of Chemistry, 2008, pp. 58-88.
14. A. C. Larson and R. B. Von Dreele, Los Alamos National Laboratory 1994.
15. B. Jaffe, W. R. J. Cook and J. H., *Piezoelectric Ceramics*, Academic Press London and New York, 1971.
16. K. M. Ok, E. O. Chi and P. S. Halasyamani, *Chem. Soc. Rev.*, 2006, **35**, 710-717.
17. V. V. Shvartsman, W. Kleemann, R. Haumont and J. Kreisel, *Appl. Phys. Lett.*, 2007, **90**, 172115.
18. N. A. Spaldin and M. Fiebig, *Science*, 2005, **309**, 391-392.
19. G. H. Haertling, *J. Am. Ceram. Soc.*, 1999, **82**, 797-818.
20. S. Priya, *J. Electroceram.*, 2007, **19**, 167-184.
21. L. W. Martin, *Dalton Transactions*, 2010, **39**, 10813-10826.
22. G. Catalan and J. F. Scott, *Adv. Mater.*, 2009, **21**, 2463-2485.
23. J. D. Bucci, B. K. Robertson and W. J. James, *J. Appl. Crystallogr.*, 1972, **5**, 187-191.
24. D. Khomskii, *Physics*, 2009, **2**, 20.
25. Yu. E. Roginskaya, Yu. E. Venevtsev, S. A. Fedotov and G. S. Zhdanov, *Sov. Phys. Crystallogr.*, 1964, **8**, 490.
26. M. Polomska, W. Kaczmarek and Z. Pajak, *Phys. Status Solidi*, 1974, **23**, 567.
27. G. A. Smolenskii and V. M. Yudin, *Sov. Phys. Solid State* 1965, **6**, 2936.
28. R. Palai, R. S. Katiyar, H. Schmid, P. Tissot, S. J. Clark, J. Robertson, S. A. T. Redfern, G. Catalan and J. F. Scott, *Phys. Rev. B*, 2008, **77**, 014110.
29. M. Valant, A.-K. Axelsson and N. Alford, *Chem. Mater.*, 2007, **19**, 5431-5436.

30. J. M. Moreau, C. Michel, R. Gerson and W. J. James, *J. Phys. Chem. Solids*, 1971, **32**, 1315-1320.
31. S. J. Clark and J. Robertson, *Appl. Phys. Lett.*, 2007, **90**, 132903-132903.
32. P. Fischer, M. Polomska, I. Sosnowska and M. Szymanski, *J. Phys. C*, 1980, **13**, 1931.
33. I. Sosnowska, R. Przeniosło, P. Fischer and V. A. Murashov, *J. Magn. Magn. Mater.*, 1996, **160**, 384-385.
34. I. Sosnowska, T. P. Neumaier and E. Steichele, *J. Phys. C*, 1982, **15**, 4835.
35. D. C. Arnold, K. S. Knight, F. D. Morrison and P. Lightfoot, *Phys. Rev. Lett.*, 2009, **102**, 027602.
36. I. A. Kornev, S. Lisenkov, R. Haumont, B. Dkhil and L. Bellaiche, *Phys. Rev. Lett.*, 2007, **99**, 227602.
37. S. M. Selbach, T. Tybell, M.-A. Einarsrud and T. Grande, *Adv. Mater.*, 2008, **20**, 3692-3696.
38. R. Haumont, I. A. Kornev, S. Lisenkov, L. Bellaiche, J. Kreisel and B. Dkhil, *Phys. Rev. B*, 2008, **78**, 134108.
39. D. C. Arnold, K. S. Knight, G. Catalan, S. A. T. Redfern, J. F. Scott, P. Lightfoot and F. D. Morrison, *Adv. Funct. Mater.*, 2010, **20**, 2116-2123.
40. R. D. Shannon, *Acta Crystallogr. Sect. A: Found. Crystallogr.*, 1976, **32**, 751-767.
41. D. A. Rusakov, A. M. Abakumov, K. Yamaura, A. A. Belik, G. Van Tendeloo and E. Takayama-Muromachi, *Chem. Mater.*, 2011, **23**, 285-292.
42. I. O. Troyanchuk, M. V. Bushinsky, D. V. Karpinsky, O. S. Mantytskaya, V. V. Fedotova and O. I. Prochnenko, *Phys. Status Solidi B*, 2009, **246**, 1901-1907.
43. I. O. Troyanchuk, D. V. Karpinsky, M. V. Bushinsky, O. S. Mantytskaya, N. V. Tereshko and V. N. Shut, *J. Am. Ceram. Soc.*, 2011, n/a-n/a.
44. I. O. Troyanchuk, D. V. Karpinsky, M. V. Bushinsky, V. A. Khomchenko, G. N. Kakazei, J. P. Araujo, M. Tovar, V. Sikolenko, V. Efimov and A. L. Kholkin, *Phys. Rev. B*, 2011, **83**, 054109.
45. J. H. Lee, H. J. Choi, D. Lee, M. G. Kim, C. W. Bark, S. Ryu, M. A. Oak and H. M. Jang, *Phys. Rev. B*, 2010, **82**, 045113.
46. I. Levin, S. Karimi, V. Provenzano, C. L. Dennis, H. Wu, T. P. Comyn, T. J. Stevenson, R. I. Smith and I. M. Reaney, *Phys. Rev. B*, 2010, **81**, 020103.
47. S. Karimi, I. M. Reaney, I. Levin and I. Sterianou, *Appl. Phys. Lett.*, 2009, **94**, 112903.
48. T. Peterlin-Neumaier and E. Steichele, *J. Magn. Magn. Mater.*, 1986, **59**, 351-356.
49. S. Geller and E. A. Wood, *Acta Cryst.*, 1956, **9**, 563-568.
50. S. Acharya, J. Mondal, S. Ghosh, S. K. Roy and P. K. Chakrabarti, *Mater. Lett.*, 2010, **64**, 415-418.
51. S. Karimi, I. Reaney, Y. Han, J. Pokorny and I. Sterianou, *Journal of Materials Science*, 2009, **44**, 5102-5112.
52. V. L. Mathe, K. K. Patankar, R. N. Patil and C. D. Lokhande, *J. Magn. Magn. Mater.*, 2004, **270**, 380-388.

53. K. Kalantari, I. Sterianou, S. Karimi, M. C. Ferrarelli, S. Miao, D. C. Sinclair and I. M. Reaney, *Adv. Funct. Mater.*, 2011, **21**, 3737-3743.
54. I. Levin, M. G. Tucker, H. Wu, V. Provenzano, C. L. Dennis, S. Karimi, T. Comyn, T. Stevenson, R. I. Smith and I. M. Reaney, *Chem. Mater.*, 2011, **23**, 2166-2175.
55. V. A. Khomchenko, D. V. Karpinsky, A. L. Kholkin, N. A. Sobolev, G. N. Kakazei, J. P. Araujo, I. O. Troyanchuk, B. F. O. Costa and J. A. Paixão, 2010, **108**, 074109.
56. C. Sun, Y. Yang, G. Yuan, J. Yin and Z. Liu, *Mater. Lett.*, **72**, 160-163.

Experimental Methods

2.1 Synthesis

The following section describes the solid-state synthesis of BiFeO_3 , which was the starting point for the development of the methods for the synthesis of rare earth doped bismuth ferrite mentioned hereafter. Temperatures and procedures were gradually changed and adapted depending on requirements - typically to produce robust, dense, electrically insulating, single-phase samples.

The reagents used in the following methods were sourced from the following companies outlined in Table 2.1.

Table 2.1: Source for the chemical reagents

Chemical	Source
Bi_2O_3	Johnson Matthey co. Ltd.
Fe_2O_3	Johnson Matthey co. Ltd.
La_2O_3	Hopkins & Williams Ltd.
Nd_2O_3 ($\geq 99.9\%$)	Sigma Aldrich
$\text{La}(\text{NO}_3)_3 \cdot 6\text{H}_2\text{O}$ ($\geq 99.0\%$)	Fluka
$\text{Nd}(\text{NO}_3)_3 \cdot 6\text{H}_2\text{O}$ ($\geq 99.9\%$)	Sigma Aldrich

2.1.1 Solid state synthesis - BiFeO_3 ¹

BiFeO_3 was made with 6% molar excess of Bi_2O_3 . The oxides, Bi_2O_3 and Fe_2O_3 , were ground with a mortar and pestle, in acetone. The ground powder was heated to 800 °C in air for a period of 5 hrs. The product was then reground and stirred in nitric acid (2.5 M) for 2 hours to leach the secondary phase - Sillenite ($\text{Bi}_{25}\text{FeO}_{39}$). The filtered product was dried at 400 °C for 1 hr. The dry product was then pressed into pellets and fired at 800 °C (2 hrs.) covered in a protective sacrificial BiFeO_3 powder. The pellets were then suitable for structural and electrical characterisation.

2.1.2 Synthesis of $\text{Bi}_{1-x}\text{RE}_x\text{FeO}_3$ (RE = La, Nd)

The synthesis of $\text{Bi}_{1-x}\text{RE}_x\text{FeO}_3$ (RE = La, Nd) was performed *via* conventional solid-state methods. Conditions were adapted depending on the rare earth and composition (x). The following methods outline the final synthesis conditions best suited for the preparation of samples. Platinum foil was used as a surface lining for the alumina boats used in calcination steps. Rare earth doped bismuth ferrite precursors and powders were always pressed into pellets prior to heating. The powders were ball milled in ethanol between each calcination step (600rpm, 1 hr.). Cylindrical pellets were pressed with a uniaxial press to a pressure of *ca.* 70 MPa.

2.1.3 Synthesis of $\text{Bi}_{1-x}\text{RE}_x\text{FeO}_3$ (RE = Nd $x \leq 0.2$, La $x \leq 0.25$)

Stoichiometric amounts of Bi_2O_3 and Fe_2O_3 were mixed with the appropriate rare earth oxide (RE_2O_3) which was dried at 1000 °C prior to weighing. The mixed powders were ball milled in ethanol using a Fritsch Pulverisette 7 planetary micro ball mill (600rpm, 1 hr.). The dry powders were then calcined in a two-step reaction. The atmosphere could be enriched with oxygen or nitrogen during the calcination steps.

In the initial step, the samples were pressed into pellets and heated to 800 °C, where they remained at temperature for 5hrs. The pellets were then reground into a fine powder and milled in ethanol under the same milling conditions (600 rpm 1 hr.).

The second dwell temperature was varied depending on the melting point of the samples. Compositions outlined in this section were heated to 1000 °C and were held at temperature for 5 hrs. The pellets were then suitable for electrical characterisation.

Regarding the lanthanum series, samples were synthesised under a nitrogen atmosphere to make the samples more resistive.

2.1.4 Synthesis of $\text{Bi}_{1-x}\text{RE}_x\text{FeO}_3$ (RE = Nd $x > 0.2$, La $x > 0.25$)

The method for the formation of samples within the composition range RE = Nd $0 < x < 0.2$, La $0 < x < 0.25$ was adapted from the previous method.

Rare earth nitrates ($\text{RE}(\text{NO}_3)_3 \cdot 6\text{H}_2\text{O}$) were mixed with Bi_2O_3 and Fe_2O_3 in stoichiometric amounts. The nitrates were dissolved in ethanol prior to the first ball milling step ensuring better homogeneity. The dry powders were pressed into loose pellets before slowly heating to $800\text{ }^\circ\text{C}$ (allowing for the slow decomposition of the nitrate and evolution of gas) and dwelling for 5 hrs.

The second step synthesis temperature for lower doped samples was adapted to avoid melting and secondary phases. Compositions where $x \leq 0.15$ were heated to $900\text{ }^\circ\text{C}$ for 5 hrs. Samples where $x > 0.15$ were heated to $1000\text{ }^\circ\text{C}$. After the second heating step, pellets were suitable for electrical characterisation.

Again, in the lanthanum series, it was found that the electrical properties were more resistive when synthesised under nitrogen. Therefore, synthesis of the lanthanum-doped samples was performed under an enriched nitrogen atmosphere. Following synthesis, the samples were characterised using a variety of different techniques outlined below.

2.2 Powder x-ray diffraction

Following the sample synthesis, the initial characterisation was performed at ambient temperature using powder x-ray diffraction (PXRD). X-ray diffraction patterns were collected from the powder samples and were initially compared to known standards. Standards were obtained from the Inorganic Crystal Structure Database (ICSD).² Data were initially collected on a STOE StadiP Powder diffractometer with a Fe source (Fe $K\alpha_1$ 1.9373 \AA). This presented the benefit of a lower background response relative to the equivalent instrument using a Cu source due to fluorescence from the sample. It was found that better results could be obtained with the Phillips diffractometer with a Cu $K\alpha_{1+2}$ source in reflection geometry. A secondary monochromator was used to solve issues with fluorescence.

2.2.1 Fundamentals of x-ray diffraction^{3,4}

X-rays are part of the electromagnetic spectrum, consisting of a transverse wave with an electrical and magnetic component, which means they are able to interact with matter (electron cloud). This interaction can occur in a number of different ways: coherently (elastic) scattering, *i.e.*, the energy of the radiation is unchanged from the incident beam; incoherent, Compton scattering caused by inelastic interactions where energy is lost; and finally by absorption where the energy of the photons are changed by means of the ejection of electrons from the atom.

X-rays have a wavelength (λ) with a range ~ 0.1 to ~ 100 Å, which encompasses the range of interatomic bonds. In the case of the copper source diffractometers, the radiation has a wavelength of 1.541 Å ($K\alpha_1$) and 1.544 Å ($K\alpha_2$). This allows for a phenomenon called diffraction *i.e.*, the interaction of the electromagnetic wave with the electronic cloud resulting in the apparent bending of the electromagnetic radiation and consequential superposition of waves with constructive and destructive interference.

This superposition of electromagnetic radiation with a similar wavelength to that of the interatomic distance gives rise to Bragg's law (Equation 2.1) which describes the condition for constructive interference of waves.

$$n\lambda = 2d_{hkl} \sin \theta \quad \text{Equation 2.1}$$

Bragg's Law where n = the order of diffraction (a positive integer), λ = wavelength, d_{hkl} is the spacing between lattices planes (hkl) and $\sin \theta$ is the angle of incidence.

As described in the section on crystallography 1.2, a crystal can be regarded as layers of atoms or parallel planes of equally spaced atoms. These planes are referred to as Miller planes. The distance between these planes is the d-spacing (d_{hkl}). The incident radiation has a wavelength (λ) and interacts with these layers of atoms. The diffracted radiation from multiple layers will then interact producing an interference pattern, which is dependent on the path difference between the layers. Simple geometry relates the angle of incidence (θ) and the spacing between the layers (d_{hkl}) to this path difference, which produces the Bragg equation.

A schematic showing the incident radiation and path difference in the Bragg equation is shown in Figure 2.1.

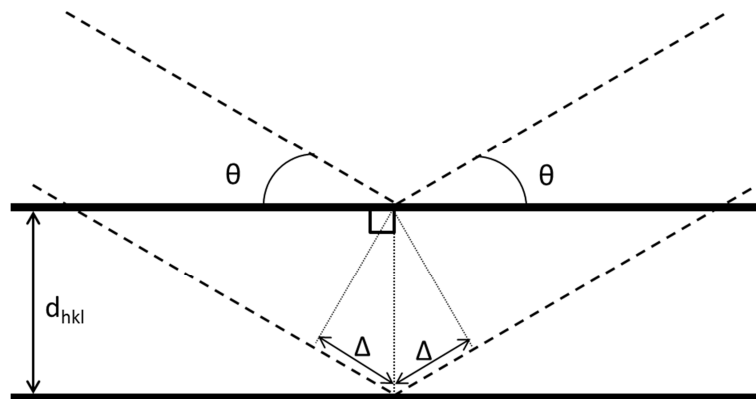


Figure 2.1: A diagram showing the path difference for two incident beams resulting in constructive interference. ($\Delta = d_{hkl} \sin \theta$)

The order of diffraction is typically taken to have a value of one which means that there are equivalent reflection conditions *i.e.*, second order diffraction from the (100) plane will be equivalent to first order diffraction from the (200) plane.

2.2.2 Reciprocal lattice and Ewald's sphere³⁻⁵

As described in the previous section on fundamentals of diffraction (2.2.1), the scattering angle of the diffracted beam is dependent on the spacing between the Miller planes. The incident beam of known wavelength interacts elastically with a single crystal and the beam is diffracted through an angle 2θ . An alternate representation is Ewald's representation, which considers the lattice in reciprocal space. The reciprocal lattice is a useful construct as it allows a lattice plane in real space to be described by a single point in reciprocal space and relates to the spots produced by a diffraction pattern of a single crystal.

The real and reciprocal lattices are related *via* a transformation between real and reciprocal space. The cross product of two vectors gives a third vector perpendicular to the plane of the initial vectors following a right hand rule.

The lattices share the same origin and the lattices parameters a , b , c and volume V have equivalent parameters a^* , b^* , c^* , and V^* in reciprocal space and satisfy the following conditions:

$$ab^* = ac^* = bc^* = a^*b = a^*c = b^*c = 0 \quad \text{Equation 2.2}$$

$$a^*a = b^*b = c^*c = 1 \quad \text{Equation 2.3}$$

These conditions lead on to further conclusions, for instance, as a^* is perpendicular to b and c such that the parameters are related via:

$$a^* = x(b \cdot c) = bc \cdot \sin(\alpha)$$

$$a^*a = x(bc \cdot a) = xV \Rightarrow x = \frac{1}{V} \quad \text{Equation 2.4}$$

$$a^* = \frac{1}{V}(b \cdot c)$$

These relations can be used to extract information from diffraction patterns relating to the real lattice.

Ewald's representation uses the reciprocal lattice to describe where points in the diffraction pattern are observed. The representation describes the incident beam with a vector, k_0 , and a wavelength that is unchanged by elastic interactions with a single crystal. The scattered wave has a different vector, k_1 . The absolute magnitudes of the vectors are equal to the reciprocal wavelength $|k_0| = |k_1| = 1/\lambda$. The vectors k_0 and k_1 are connected by a single origin from which a sphere, the Ewald's sphere, with a radius $1/\lambda$ can be drawn (Figure 2.2).

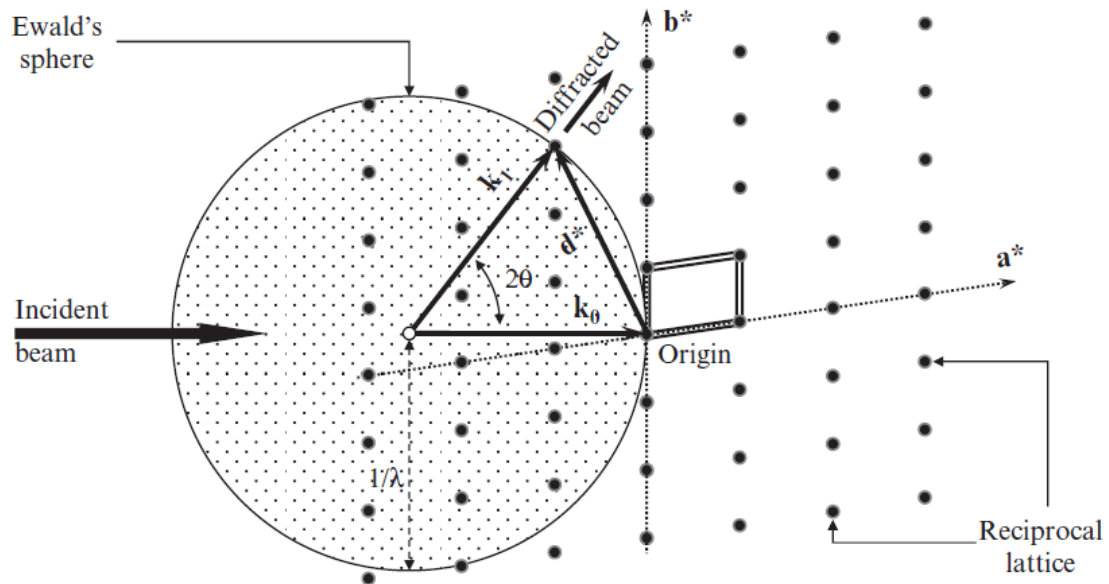


Figure 2.2: The visualization of diffraction using the Ewald's sphere with radius $1/\lambda$ and the two dimensional reciprocal lattice with unit vectors a^* and b^* .⁴

A vector connecting points from the reciprocal lattice on the surface of this sphere (where k_0 and k_1 intercept) is d_{hkl}^* . This vector is related to the d_{hkl} spacing by $d_{hkl}^* = 1/d_{hkl}$. The angle between k_0 and k_1 is 2θ . A point in the diffraction pattern is only observed when a reciprocal lattice point other than the origin intersects with the surface of the Ewald's sphere.³

2.3 Generation of x-rays^{3,4}

X-rays were generated using a lab based x-ray vacuum tube with a copper or iron target. Electrons are liberated from a tungsten filament and are accelerated towards the copper target under a 40 kV potential. Electrons from the tungsten cathode hit the copper/iron anode. Multiple inelastic collisions result in a reduction in the velocity of the accelerated electrons and the generation of x-rays. The random deceleration and "braking" of electrons give rise to a broad range of wavelengths called bremsstrahlung radiation (from the German).

Electrons can be excited from the core shell of the metal target. This allows electrons in the higher energy levels to relax and consequently emit radiation at very specific wavelengths, *i.e.*, $K\alpha_1$ and $K\alpha_2$, corresponding to the relaxation from $2p_{1/2} \rightarrow 1s_{1/2}$ and $2p_{3/2} \rightarrow 1s_{1/2}$, respectively. This radiation of known wavelength is used for diffraction experiments

and is shown in Figure 2.3, a schematic of the emitted radiation. The primary beam is passed through a monochromator, which selects a band of wavelengths predominately associated with the $K\alpha$ radiation removing unwanted wavelengths associated with inelastic collisions.

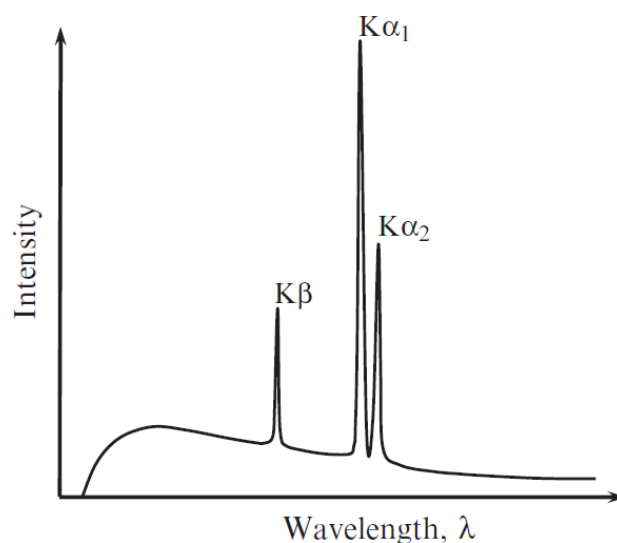


Figure 2.3: Emitted radiation intensity as a function of wavelength; showing intense emission of $K\alpha_1$, $K\alpha_2$ and $K\beta$ radiation ($3p \rightarrow 1s$)⁴

2.4 Powder neutron diffraction (c.f. PXRD)

Powder neutron diffraction (PND) patterns were collected using the high-resolution powder diffraction (HRPD) instrument at the ISIS neutron spallation source, Rutherford Appleton Laboratories.

Sample preparation for the PND experiments depended on the environmental conditions. High temperature furnace work and room temperature readings were taken using cylindrical vanadium cans. K-type thermocouples were placed in contact with the top of the can as close as possible to the sample.

Low temperature measurements used flat plate cuboidal aluminium cans with vanadium windows. The aluminium was covered with a cadmium metal mask such that it was not visible to the neutrons. A RhFe thermocouple was mounted in the wall of the aluminium can. The sample temperature was controlled by a heating element mounted in the opposite wall to the thermocouple ensuring that the recorded temperature is not local just to the heating element.

2.4.1 Fundamentals of neutron diffraction ^{4,6}

Neutrons are scattered by the atomic nuclei rather than the electrons. This is different to XRD where the x-rays scatter from the interaction with all the electrons in the atom. This means that neutrons are more sensitive than x-rays to lighter atoms with few electrons. Neutrons have a non-zero spin ($s = \frac{1}{2}$) which means that they are able to interact with unpaired electrons in the valence band. When unpaired electrons have long-range (magnetic) order, it gives rise to coherent scattering of the neutrons. This means that there are two origins of scattering of neutrons - magnetic diffraction and nuclear diffraction. These contributions can be de-convoluted using Rietveld refinement as described in section 2.6.

2.4.2 Generation of neutrons ⁷

Powder neutron diffraction uses neutrons from a reactor or spallation source. At ISIS, a spallation source generates a beam of neutrons. This involves producing a source of H^- ions from a plasma that is then channelled in a pulsed stream through magnets which removes free electrons. The stream of H^- ions is then accelerated and focused before it is passed into a radio frequency quadrupole (RFQ). This RFQ uses intense electric fields in the radio frequency range to focus the particles and bunches them before passing them into the linear accelerator (Linac). The Linac significantly accelerates the particles in pulses before they are held in the synchrotron. Upon entering the synchrotron, the H^- ions are stripped of their electrons and the proton beam is accelerated. The proton beam is then sent towards the target (spallation source). This target consists of a water-cooled metal tungsten plate. High-energy neutrons are produced when the proton beam hits the target. The beam is then moderated for use in diffraction experiments by passing it through different media at a range of different temperatures, slowing the neutron beam.

2.5 HRPD instrument ⁸

The HRPD instrument consists of three arrays/banks of detectors at fixed angles: a ‘backscattering’ bank, a 90° bank, and a 30° ‘low angle’ bank. As the detectors are at a fixed angle, the instrument utilises time of flight rather than angular-dispersive diffraction.

The wavelength and consequently the d-spacing *via* Bragg’s law (Equation 2.1) are determined from the time it takes for a neutron to travel over a known flight path *i.e.*, the time of flight. Using the de Broglie relationship and the kinetic energy of a particle the wavelength is related to the energy of the neutron by:

$$\lambda = \sqrt{h^2/2mE} \quad \text{Equation 2.5}$$

where h is Planck’s constant, m is the rest mass of a neutron, and E is the kinetic energy.

The spallation source produces neutrons with a range of different energies and consequently velocities that cover the flight path, L , over a range of different times, t . This means the wavelength is varied rather than the angle of incidence.

Combining Bragg’s law Equation 2.1 with Equation 2.5 gives the energy relationship with d-spacing from which the velocity and time of flight can be calculated.

$$\sqrt{h^2/2mE} = 2d_{hkl} \sin \theta = ht/mL \quad \text{Equation 2.6}$$

The three banks at different angles allow the instrument to cover a larger range of d-spacings for a given range of energies. The backscattering bank at 168° from the incident beam is based on a ZnS scintillator and can collect data from 0.6 – 4.6 Å d-spacing. The data from the backscattering bank has been used for Rietveld refinements (see section 2.6). The detectors at 90° also use ZnS scintillators and collect data from 0.9- 6.6 Å d-spacing. The low angle bank uses ³He-based detectors collecting from 2.2 – 16.5 Å. The 90° and low angle banks have slightly lower resolution. However, the accessibility of higher d-spacings in these banks can be useful to detect the presence of predominantly magnetic reflections that are not obscured by structural intensity. The arrangement of the banks is shown in Figure 2.4.

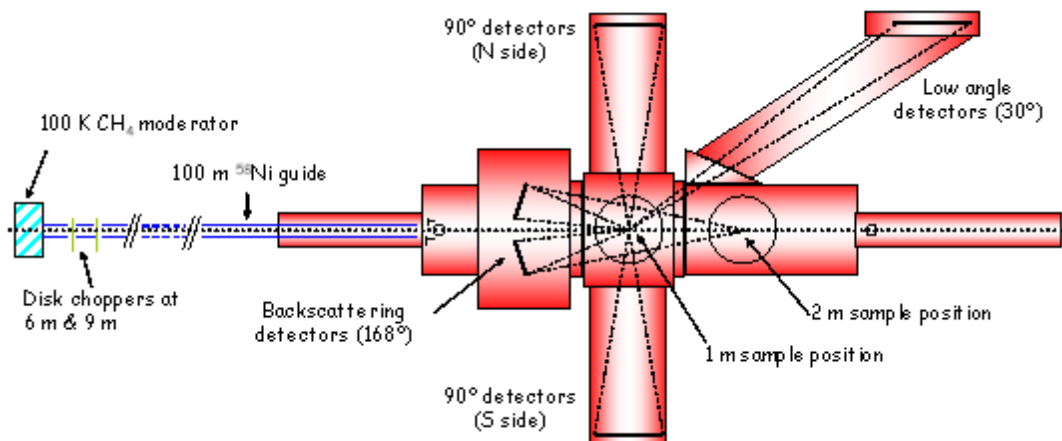


Figure 2.4: A schematic of HRPD showing the three detectors: backscattering, 90° banks and a low angle 30° bank.⁸

2.6 Rietveld refinement⁹⁻¹²

Powder patterns from neutron and XRD experiments were analysed using the Rietveld method to structurally categorise the different samples. Refinements were carried out using the general structural analysis system (GSAS) and its associated graphical user interface program (EXPGUI).^{11, 13}

The Rietveld method was developed in the 1960s for the analysis of polycrystalline samples.⁴ It is an invaluable tool due to its ability to analyse complex diffraction patterns with overlapping Bragg peaks. The method is outlined in Rietveld's 1969 paper on "least-squares refinement based on profile intensities for the refinement of nuclear and magnetic structures".¹⁴ The method aims to minimise the difference by least squares refinement between a calculated model and the experimental data. It does this by making small incremental changes to the model. The technique developed by Rietveld has subsequently been adapted to allow for different peak profiles found in XRD patterns.⁴

In order to understand what Rietveld refinement is attempting to model, an understanding of the origins of the intensities produced from a powder pattern is required. A single crystal produces a diffraction pattern comprised of a number of spots relating to the Miller planes by the Ewald's representation, as described in section 2.2.2. Single crystal diffraction patterns are collected across a surface relative to this sphere and are comprised of a

number of points. The powder diffraction pattern is complicated by the fact a powder is comprised of a number of crystallites randomly orientated such that multiple spots are generated from a single reflection and cones are generated from the Ewald's representation. The cumulative intensities of the reflections are therefore typically measured from a cross section of the Ewald's sphere producing the powder diffraction pattern. If the powder is comprised of a number different crystallites *i.e.*, secondary phases or the single phase has similar d-spacings there may be a number of overlapping cones and the origin of the intensities in the pattern can be resolved using the Rietveld method.

The intensity of any reflection (I_{hkl}) that the Rietveld method attempts to model at a given angle is dependent on a number of other factors such as the ability of the atoms to scatter, the summation of this scattering ability within the unit cell for a given Miller plane, and the distribution of intensity due to thermal motion. These parameters are described by the atomic scattering factor *i.e.*, the scattering power of the atoms or electron cloud; the structure factor is the resultant intensity from all the atoms in the unit cell for any given Miller plane; and finally, the temperature factor which corrects for the thermal motion of atoms.

The structure factor, F_{hkl} , is related to the intensity (I_{hkl}) of the radiation by a squared relationship.

$$I_{hkl} = |F_{hkl}|^2 \quad \text{Equation 2.7}$$

Numerically the structure factor for x-rays is comprised of the following terms:

$$F_{hkl} = \sum_i f_i \exp[2\pi j(hx_i + ky_i + lz_i)] \exp T' \quad \text{Equation 2.8}$$

where f_i is the atomic scattering factor of atom i , x_i y_i and z_i are the atoms atomic coordinates and T' is the temperature factor where T' for isotropic refinements is given by

$$T' = - \left[8\pi^2 U_{iso} \sin^2 \theta / \lambda^2 \right] \quad \text{Equation 2.9}$$

U_{iso} is a refinable numerical parameter where θ is the Bragg angle and λ is the wavelength.

In PND, there can be additional intensity from a magnetic component (F_{mag}^2) that is accounted for in the structure factor.

$$F^2 = F_{nuc}^2 + F_{mag}^2 = F_{nuc}^2 + \sum_i q_i p_i \exp[2\pi i h x_i] \quad \text{Equation 2.10}$$

p_i is the magnetic cross section, q_i is the magnetic interaction vector.

In powder diffraction there are additional factors that affect peak intensities due to reflections with similar d-spacings and equivalent Miller planes. This means that the minimisation function for powder diffraction is based on the intensity at a given angle. The minimisation function used in least squares refinement is outlined in Equation 2.11 where M_p is the term minimized for powder diffraction, w_i is a weighting factor, y_{oi} is observed intensity for the i^{th} step, and y_{ci} is the calculated intensity for the i^{th} step.

$$M_p = \sum_i w_i (y_{oi} - y_{ci})^2 \quad \text{Equation 2.11}$$

The weighting factor (w_i) is comprised of several terms and is based on the variance between the total peak intensity, $\sigma^2(y_{oi})$, and that of the background, $\sigma^2(B_i)$, which is arbitrarily set to zero. This means the weighting factor reduces to the reciprocal of the variance in the peak intensity:

$$w_i = \frac{1}{\sigma^2(y_{oi}) + \sigma^2(B_i)} = \frac{1}{y_{oi}} \quad \text{Equation 2.12}$$

As well as visually assessing the quality of the refinement, *i.e.*, checking the residual between the observed and calculated profile is minimal and all the reflections are accounted for between the model and observation, there are also numerical terms that describe the quality of the fit.

The residual function (R_p), Equation 2.13, is a measure of how well the calculated pattern fits the observed pattern by assessing the absolute difference between the predicted and calculated intensities.

$$R_p = \frac{\sum |y_o - y_c|}{\sum y_o} \quad \text{Equation 2.13}$$

However, this term is biased towards peaks with the most intensity and can be modified in a similar fashion to the minimisation function by weighting the residual function. This weighted residual function (wR_p) is given by:

$$wR_p = \sqrt{\frac{\sum w_i(y_o - y_c)^2}{\sum w_i y_o^2}} \quad \text{Equation 2.14}$$

As the quality of the model improves the difference (numerator term in the equations) tends towards zero meaning that the values of R_p and wR_p also tend towards zero. Therefore, a value close to zero is desired and represents a close approximation of the model to the observed reality.

The final commonly used numerical term to represent the “goodness-of-fit” is χ^2 . This term can take into account multiple diffraction patterns *i.e.*, from different banks of crystallographic data. N_{obs} and N_{var} are the number of observations and variables, respectively.

$$\chi^2 = \frac{\sum w_i(y_{oi} - y_{ci})^2}{(N_{obs} - N_{var})} \quad \text{Equation 2.15}$$

In a good refinement, the value of this parameter should be close to 1.0.

2.7 ac - Impedance spectroscopy

Alternating current impedance spectroscopy (ac-IS) was used to measure the electrical behaviour of samples. The technique applies a small oscillating potential difference to the sample and monitors the time dependent current response.¹⁵ Typically, data are collected over a wide frequency range *e.g.* 10^{-2} to 10^7 Hz.¹⁶

The electrical properties are closely related to the microstructure and homogeneity of a sample. The structure of ceramic materials can be electrically inhomogeneous. In a single-phase material, several electrically active components may exist which relate to various regions within the sample, *i.e.*, grain boundaries. These regions have different resistive (R) and capacitive (C) behaviour, which represent the various charge transfer and polarisation processes, respectively. These processes typically occur in parallel and so can be represented by the electrical component (equivalent circuit) shown in Figure 2.5.

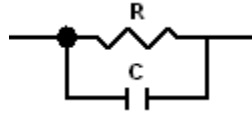


Figure 2.5: A parallel resistor and capacitor (*RC* element) representing an electroactive region.

The resistive behaviour of each region contributes to the total resistance of the sample. This total resistance is measured in many direct current techniques. Ac immittance is a powerful technique and has a significant advantage over DC measurements as it allows for the separation of these electrically active components. This separation is based on different relaxation times and their interaction with the applied alternating ac field. The relaxation time (τ) for any given electroactive region is given by the product of resistive and capacitive terms as described by in Equation 2.16.

$$\tau = RC = \frac{1}{2\pi f_{max}} \quad \text{Equation 2.16}$$

This relationship with the relaxation time and frequency of the applied voltage will be explained in detail in the following sections with relation to the four interrelated immittance formalisms: electric modulus (M^*), impedance (Z^*), admittance (Y^*), and permittivity (ϵ^*). Appropriate use of the formalisms allows for the temperature dependent analysis and separation of the different electrical components.

2.7.1 The immittance formalisms

The complex impedance (Z^*) shown in the Equation 2.17 is an adaptation of Ohms law and relates to the impedance of a resistor with an applied alternating field.¹⁵ This alternating current results in an angular term the phase angle (ω).

$$Z^* = \frac{U_{max} \sin(\omega t + \phi_U)}{I_{max} \sin(\omega t + \phi_I)} = Z' - jZ'' \quad \text{Equation 2.17}$$

The phase difference (ϕ) between the current (I) and voltage (U) response is dependent on the circuit component. For a pure resistor the current and voltage is in-phase, $\phi=0^\circ$. In a pure capacitor the phase difference is $\phi = -90^\circ$ and in an inductor $\phi = 90^\circ$.¹⁵

As the impedance formulism has a phase angle and vector based term, it can be plotted in terms of a complex plane plot utilising the Euler relationship.¹⁰ This separates the complex

impedance into real and imaginary components: the resistance (Z') and reactance (Z''). This is the case for all of the immittance formalisms – they are complex numbers with real and imaginary components with each describing either the resistive or capacitive component.

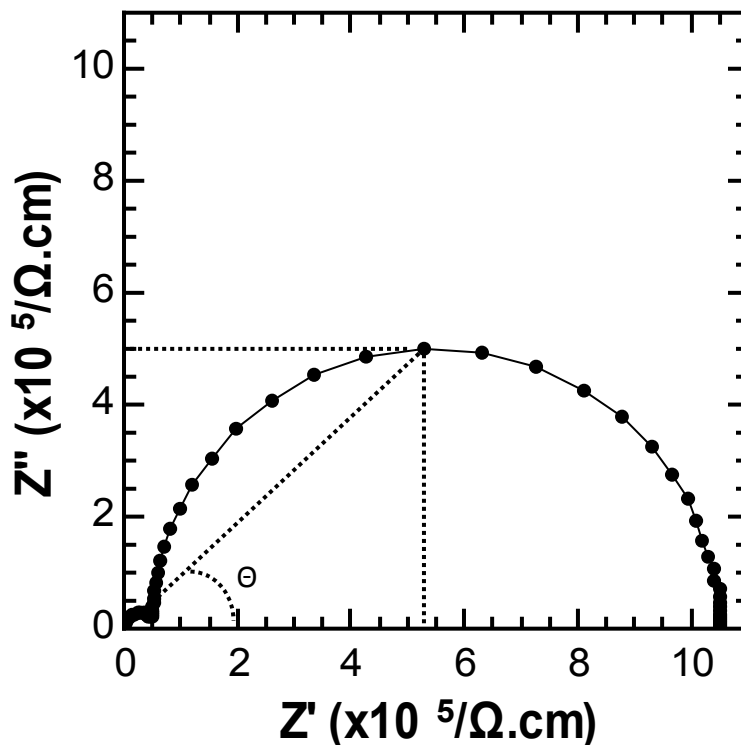


Figure 2.6 A complex plane plot of Z^* showing the real Z' and imaginary component Z'' of the complex impedance for two parallel RC elements in series.

The phase angle varies as the applied potential changes and can be plotted in terms of a frequency spectrum ($\omega = 2\pi f$ where f is the frequency in Hz). Typically, the imaginary component of the complex plane plot is plotted *i.e.*, the reactance which produces a Debye-like response in the frequency spectra. The Debye-like response should be symmetric in shape and have a full width half maximum (FWHM) of approximately 1.144 decades.¹⁷ This response is obtained if dipole interactions are ideal (non-interacting) and have the same time between transitions.¹⁷ This perfect Debye response, however, is rarely found experimentally and the response tends to be broader. The Debye peaks may be broadened or overlapping due to the presence of domains with similar relaxation times.

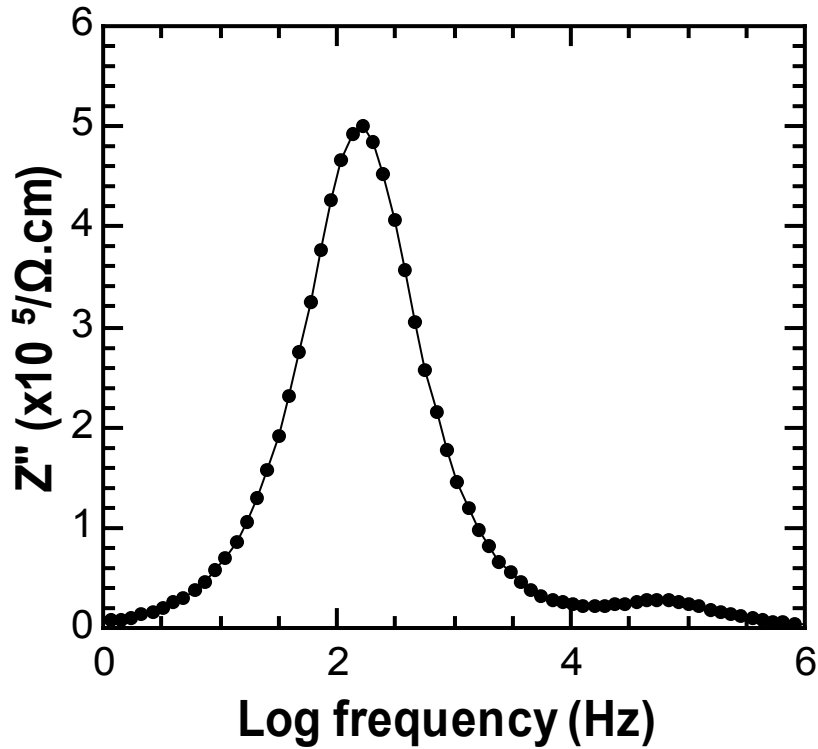


Figure 2.7: A spectroscopic plot of imaginary component Z''

The other immittance formalisms are interrelated with the complex impedance. The admittance, Y^* , for example is related to the complex impedance by taking its reciprocal (Equation 2.18). In electrical terms, rather than being a measure of the components ability to resist electrical flow (impedance), the admittance is a measure of the ability of the sample to allow the flow of electrical current. The use of the other formalisms can highlight features in the electrical response of the sample that would have otherwise been missed due to their weightings with the angular frequency (ω). Generally, it is considered that more than one formulism should be used in graphical interpretation of electrical data.¹⁸

The interrelations between the formalisms are shown below with the tabulated terms (Table 2.2):

$$Z^* = \frac{U_{max} \sin(\omega t + \phi_U)}{I_{max} \sin(\omega t + \phi_I)} = Z' - jZ'' \quad \text{Equation 2.17}$$

$$Y^* = \frac{1}{Z^*} = Y' + jY'' \quad \text{Equation 2.18}$$

$$M^* = M' + jM'' = j\omega C_0 Z^* \quad \text{Equation 2.19}$$

$$\varepsilon^* = \varepsilon' - j\varepsilon'' = \frac{1}{M^*} = \frac{1}{j\omega C_0 Z^*} \quad \text{Equation 2.20}$$

Table 2.2: A list of scientific (and engineering) symbols with their corresponding terms.

Symbol	Term
$Z^*, Z' (R), Z'' (X)$	Impedance, Resistance, Reactance
$Y^*, Y' (G), Y'' (B)$	Admittance, Conductance, Susceptance
M^*, M', M''	Complex modulus
$\varepsilon^*, \varepsilon', \varepsilon''$	Complex permittivity, Permittivity, Dielectric loss
$\tan \delta (D)$	Loss or Dissipation

In addition to the four immittance formalisms, there is an additional related term: $\tan \delta$ or the dissipation factor (D) where:

$$\tan \delta = D = \frac{\varepsilon''}{\varepsilon'} = \frac{Z'}{Z''} = \frac{Y'}{Y''} = \frac{M''}{M'} \quad \text{Equation 2.21}$$

Considering Equation 2.21 and the graphical plot of the complex impedance (Figure 2.6), $\tan \delta$ is shown to be a varying angular term describing the tangent of the vector immittance response. Its values typically range from zero (perfectly capacitive) to one (perfectly resistive). In physical terms, therefore, $\tan \delta$ represents the ratio between the resistive and its capacitive behaviour, *i.e.*, charge dissipated relative to charge stored per cycle of ac electric field.

2.7.2 Sample preparation

In order to test the electrical properties of a sample metal contacts or electrodes are required. The electrodes are applied to the cylindrical pellets that have been formed during the final calcination step. This final calcination results in a dense pellet with a geometrically regular cross section. These electrodes are typically placed parallel to each other on the circular faces of the cylinder covering the whole area – as indicated in Figure 2.8.

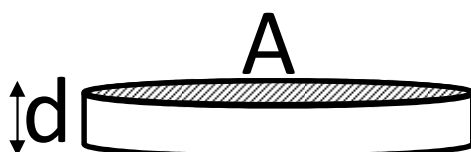


Figure 2.8: Measurements of the diameter and thickness (d) of the pellet correspond to the area (A) and separation of the electrodes.

A number of different types of metal electrodes were available including: gold, silver, platinum, and an indium/gallium alloy. Prior to applying electrodes, the cylindrical surfaces are polished to reduce surface roughness. The method used to apply the electrodes varies depending on the metal. Typically silver electrodes were applied by painting an organometallic silver layer (RS Components: silver-loaded electrically conductive paint) onto the surfaces of the pellet before curing at 120 °C (15 minutes) thus improving the electrical conductivity of the electrode surface. Other metals such as Pt, In/Ga, were applied in a similar fashion *i.e.*, application of a metallic paste (Sigma Aldrich: In powder 99.99%, Ga metal 99.9995%). The platinum electrodes are cured for 15 minutes at 1000 °C (Gwent electronic materials Ltd: Platinum paste).

Electrodes could be applied to exposed surfaces with sputtered metal (Pt, Au), *via* vapour deposition. The side of the pellet is masked to avoid creating an electrical pathway with low resistivity between the electrodes. The samples are then suitable for vapour deposition and are placed into a vacuum chamber where the atmosphere is exchanged with argon at sub-atmospheric pressure. A metal plasma generated above the sample cools and deposits metal onto the sample surfaces.

Selection of the electrode material depended on requirements. Typically, application of an electrode at low temperature is desired as it avoided potential sample decomposition.

Other considerations are the durability of the electrodes to resist scratching and high temperature. The pellet is exposed to a wide range of temperatures during analysis and the electrodes need to be durable enough such that the electrode area does not change.

2.7.3 Ceramics and the brick layer model

There needs to be an underlying understanding of the microstructure of a ceramic material to interpret electrical data successfully. An idealised model of a ceramic microstructure is composed of grains of (relatively) conducting ceramic material that are connected by a grain boundary with a different resistance.

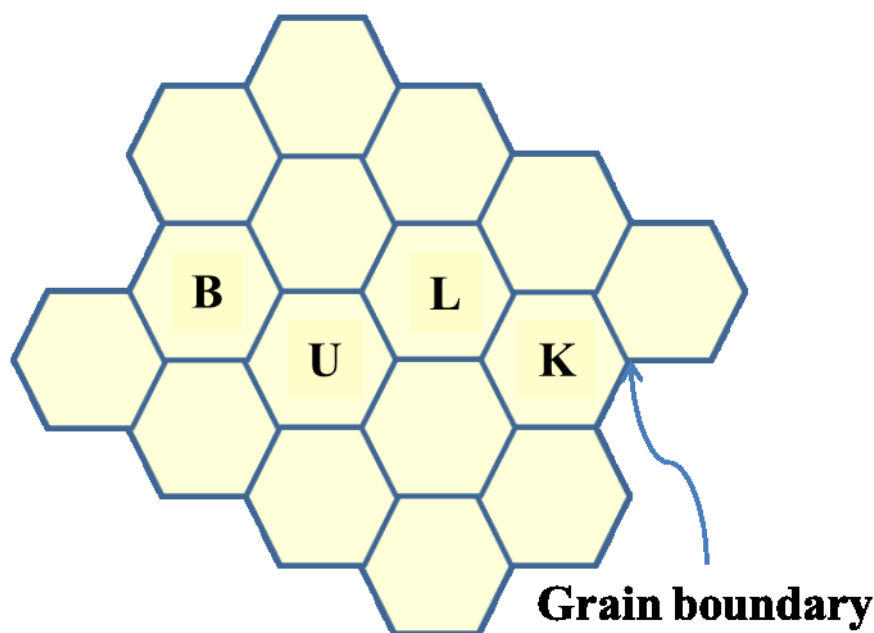


Figure 2.9: Idealised ceramic microstructure consisting of bulk ceramic and grain boundary.

The electrical path through this model will take the current through both the grain and grain boundary regions. Separation of the electrical responses is based on the time constant ($\tau = RC$) which will be explained in the following section.

Current standard practice, discussed in a number of reviews, is to interpret the collected data in terms of an equivalent electrical circuit.^{15, 16, 18} This should be the simplest sensible model that fits the data. In the case of the ceramic samples described in this thesis, they are considered to be a number of parallel RC elements placed in series (Figure 2.10). Each RC element represents a microstructural region *e.g.* bulk, grain boundary etc. This configuration

of RC elements is known as the brick layer model and represents the shortest electrical path through bulk and grain boundary (Figure 2.9).

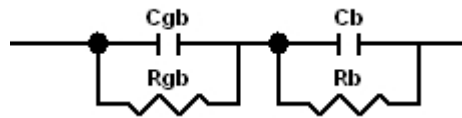


Figure 2.10: Typical RC circuit consisting of a series of capacitor and resistors signifying bulk (R_b, C_b) and grain boundary (R_{gb}, C_{gb}) resistances and capacitances.

The resistance of an electroactive region can vary significantly but the capacitive behaviour of each region is likely to fit within specific orders of magnitude, which are associated with the type of region. The magnitude of the capacitive response forms the basis for assigning electroactive regions to the electrical response.¹⁶

A parallel plate capacitor is formed by following the sample preparation procedure (2.7.2) *i.e.*, two parallel plate electrodes separated by the thickness of the sample (Figure 2.8). The material can be polarised on the application of an applied field. The capacitance of a parallel plate capacitor is given by Equation 2.22 where ϵ' is the relative permittivity (or dielectric constant), ϵ_0 is the permittivity of free space (8.854×10^{-14} F cm⁻¹), A is the electrode area, and d is the separation between parallel plates.

$$C = \epsilon' \epsilon_0 \frac{A}{d} \quad \text{Equation 2.22}$$

By substituting typical values for a material with a geometric term $d/A = 1$ cm⁻¹ and a permittivity *circa* 10 as described by Irvine *et al.*¹⁶, it can be shown that the bulk capacitances are around 1×10^{-12} Fcm⁻¹.

$$\frac{C_b}{C_{gb}} = \frac{d_{gb}}{d_b} \quad \text{Equation 2.23}$$

As a consequence of the relationship shown in Equation 2.22, the capacitance of the grain boundary are based on the reciprocal of the boundaries thickness. In a well-sintered sample, the grains will have grown and the grain boundaries are relatively thin. Consequently, the boundary has a higher capacitance than that of the bulk ($C_{gb} \gg C_b$). Lower grain boundary capacitive values are often found in poorly sintered samples that may contain narrow contacting 'necks' between grains.¹⁹ These differences in the ceramic microstructure result

in a large range of grain boundary capacitive responses ranging from 10^{-8} - 10^{-11} Fcm^{-1} , Table 2.3., as outlined by Irvine *et al.*¹⁶

Table 2.3: Capacitance values and there possible interpretations.¹⁶

Capacitance (Fcm^{-1})	Phenomenon Responsible
10^{-12}	Bulk
10^{-11}	Minor secondary phases
10^{-11} - 10^{-8}	Grain boundary
10^{-10} - 10^{-9}	Bulk ferroelectric
10^{-9} - 10^{-7}	Surface layer
10^{-7} - 10^{-5}	Sample-electrode interface
10^{-4}	Electrochemical reactions

Having established the relative differences in capacitive response between the regions and the typical electrical circuit from the brick layer model the capacitive response as a function of frequency can be evaluated. The total parallel capacitance of an equivalent circuit consisting of two parallel RC elements in series as a function of frequency results in two frequency independent plateaus.¹⁸ The total parallel capacitance (C_p) measured on the high frequency plateau contains contributions from both the bulk (C_b) and grain boundary (C_{gb}) capacitances according to Equation 2.24:

$$C_{p(\omega \rightarrow \infty)hf} = \left[(C_b)^{-1} + (C_{gb})^{-1} \right]^{-1} \quad \text{Equation 2.24}$$

Assuming that the resistance and capacitance of the bulk are significantly lower ($R_b \ll R_{gb}$ and $C_b \ll C_{gb}$) than that of the grain boundary, the high frequency plateau is dominated by that of the bulk. This means that the high frequency capacitance can be taken to approximately equal to that of the bulk ($C_{hf} \approx C_b$). On confirmation of the assumptions with isothermal measurements, total capacitance measurements can be performed with a temperature sweep. The analysis procedure of such isothermal readings is described in section 2.7.6.

Typically, a frequency of 1 MHz is at a sufficiently high frequency such that Equation 2.24 is valid and the measurements taken on the high frequency plateau of the total capacitance vs. frequency plot represent the bulk behaviour. However, there are other effects, which are not intrinsic to that of the bulk. These can be caused by depletion layers between metal-insulator boundaries such as the electrode and the ceramic, non-stoichiometry, or accumulation of defects *i.e.*, oxygen deficiency.²⁰ These effects such as depletion layers can artificially enhance the perceived values obtained for the relative permittivity of the bulk based on Equation 2.24. For semiconducting samples, Schottky barriers may form at an interface if the work function of the metal electrode is higher than that of the sample such that the electron concentration is suppressed and a depletion layer is formed.²⁰ This creates a region of high resistivity and high capacitance. Isothermal ac-impedance measurements can identify if such effects are present in samples.

2.7.4 Data collection

The preparation of the samples for ac impedance spectroscopy is outlined in 2.7.2. There are a number of different methods available for the electrical analysis of samples with electrodes. The two methods outlined in the following sections are based on isothermal measurements and temperature sweeps.

The samples were mounted in one of two custom-made frameworks designed for sub-ambient analysis and work at elevated temperatures. A thermocouple/diode is mounted within close proximity of the two platinum wires that make contact with electrodes of the prepared sample. High temperature (above ambient) measurements were performed in a jig represented in Figure 2.11:

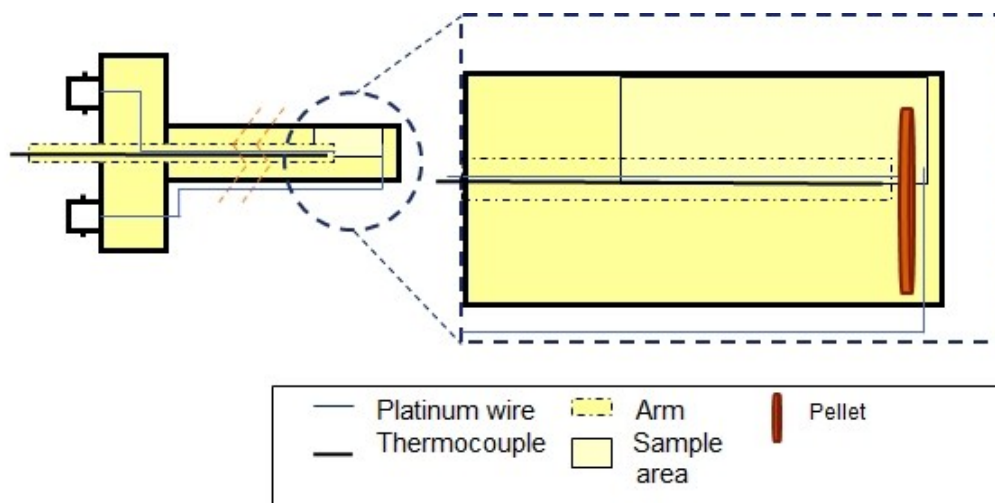


Figure 2.11: High temperature jig for electrical measurements: showing a truncated view of the jig with an enlarged view of the sample area

The sample is mounted in the indicated sample area and the movable arm is adjusted to make contact with the pellet. The platinum wires are connected to BNC terminals that are connected to the impedance analyser. Temperature control is achieved by mounting the jig in a Carbolite tube furnace and altering the set temperature.

Low temperature (sub-ambient) work was performed in a similar framework housed in a Sumitomo HC-2 cryogenics system and mounted within close proximity of the cold head. Temperature control of the cryogenics system was governed by a Scientific Instruments 9700 temperature controller.

Isothermal readings were taken on the Hewlett Packard 4192A LF impedance analyser. Readings are considered isothermal when there is no longer a significant fluctuation in the temperature while the impedance analyser is taking its readings. The temperature is then changed stepwise, gradually moving the electrical responses through the analysers frequency window (5 to 10^7 Hz).

2.7.5 Total capacitance and loss sweeps

Two programs were developed for the automated collection of capacitance and loss information during a temperature-controlled sweep. This data represents the total capacitance of the sample response, which at sufficiently high frequencies approximated to that of the bulk response (see section 2.7.3). It is then used for the calculation of dielectric constant and loss as a function temperature. The dielectric constant is calculated from the

total capacitance (C_p) measurement using Equation 2.22 and the loss (D) is the instrument other output.

The automated systems developed as part of this work control the cryostat in conjunction with an Agilent 4294A impedance analyser and a Carbolite furnace with a Wayne Kerr 6500B impedance analyser. They allow for the collection of many points, giving high temperature resolution, critical to the detection of phase transitions. Isothermal measurements would have taken significantly longer to achieve the same.

Temperature readings from a thermocouple situated next to the sample (henceforth called the sample temperature) were taken every 2 seconds. These readings are compared to trigger temperatures that are generated from a temperature start point and sampling temperature interval. Acceptable temperature values for the system to trigger the impedance analyser are ± 0.1 °C of any given target temperature. After data collection the software will wait *circa* 20 seconds for the temperature to change outside of the temperature window to avoid repeat readings.

Frequency readings are taken quickly to avoid significant temperature changes. The furnace and cryostat controllers govern the rate at which the sample changes temperature reaching the programmed target temperature; typically heating/cooling rates were 2 °C min^{-1} .

2.7.6 (ac-IS) Data analysis of isothermal data

Data analysis of isothermal immittance readings can be used to determine the magnitudes of bulk and grain boundary resistive and capacitive responses. These reading validate the use of total capacitance measurements performed during a temperature sweep. The validation confirms the assumptions about the relative magnitudes of the bulk and grain boundary responses $R_b \ll R_{gb}$ and $C_b \ll C_{gb}$ and confirms which frequencies are on the high frequency plateau where Equation 2.24 is valid. Activation energies of the various conduction process(es) can also be determined (see section 2.7.7)

Data analysis was performed using ZView version 2.9 produced by Scribner Associates Inc.²¹ This program provides the user with a number of different complex plane and frequency dependent (spectroscopic) plots. The resistance and capacitance of the components are extracted from the interpretation of these plots, as discussed below.

Electrical analysis used a combined approach of utilising electric modulus (M^*) and impedance (Z^*) data where appropriate. Resistive components dominate the impedance spectra and the electrical modulus is dominated by the smallest capacitive component *i.e.*, the bulk.

For the purposes of discussion, the electrical circuit that will be considered will be that of the circuit represented in Figure 2.10. Each parallel RC element will give rise to a semi-circular arc in the complex modulus and impedance plots as well as a Debye peak in the Z'' and M'' spectroscopic (frequency domain) plots. Before going further with the methodology, it should be noted that the Debye response should have a FWHM of approximately 1.14 decades, however, this is rarely observed; as long as the response does not exceed *ca.* 1.5 decades, however, approximate R and C values can be obtained using the following methodology.²²

M'' is the imaginary part of the complex modulus and relates to the resistive and capacitive behaviour of a parallel RC element (Figure 2.5) by:

$$M'' = \frac{\epsilon_0}{C} \left[\frac{\omega RC}{1 + (\omega RC)^2} \right] \quad \text{Equation 2.25}$$

(where ω is the angular frequency and ϵ_0 is the permittivity of free space, $8.854 \times 10^{-12} \text{ Fm}^{-1}$)

The term, $\frac{\epsilon_0}{C}$, means that the modulus plots (M^* and M'') are dominated by the RC elements with the smallest capacitance. The reactance (Z'') is related to the RC components *via*:

$$Z'' = R \left[\frac{\omega RC}{1 + (\omega RC)^2} \right] \quad \text{Equation 2.26}$$

In this case the R term means that the impedance (Z^*) and reactance spectra (Z'') are dominated by the most resistive component.

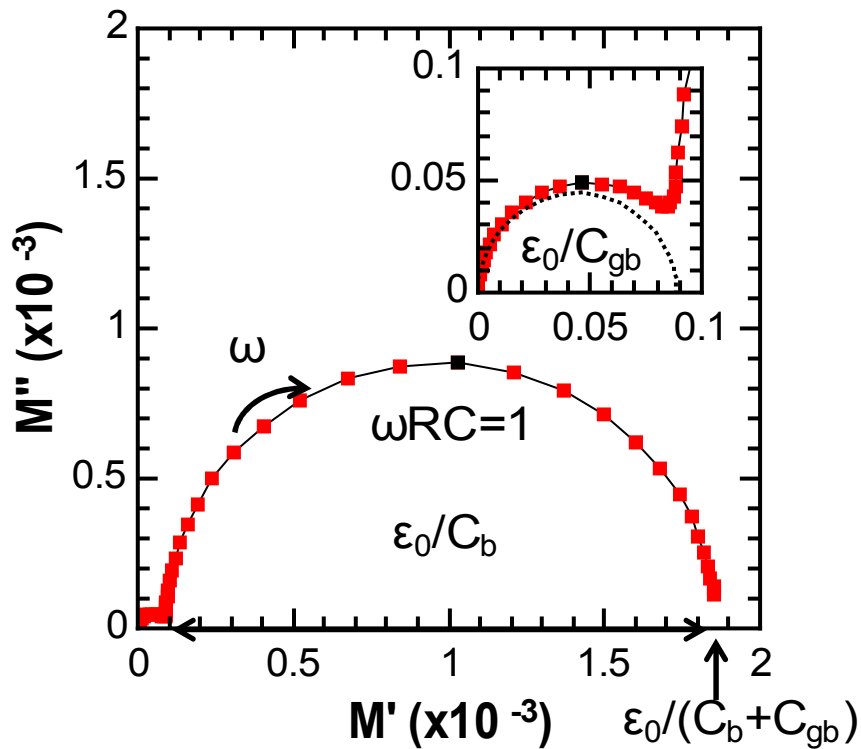


Figure 2.12: A simulated plot of the complex plot, M^* showing two electrical components comprising of the grain boundary and bulk. The values of C_b, C_{gb}, R_b and R_{gb} were selected such that there is a clear separation in the frequency domain.

The simulated data (Figure 2.12) is based on a bulk resistance of 50 k Ω with a grain boundary resistance of 1 M Ω . The bulk capacitance is 50 pF with a grain boundary capacitance of 1 nF. These capacitive values are based on the order of magnitude expected for the types of processes that occur within the grain boundary and bulk as tabulated by the authors Irvine *et al.*¹⁶ The different orders of magnitude for the capacitive components within the circuit means that the largest response in the complex modulus can be easily identified as belonging to the bulk as it represents the smallest capacitive component. The smaller semi-circular response belongs to that of the grain boundary.

Employing, ac-IS there is an angular frequency (ω) which is given by $\omega = 2\pi f$ (where f is the frequency in Hz). Each component has a different time constant, as discussed earlier, given by the product of resistance and capacitance of the components (Equation 2.16). The frequency associated with the maxima in each semicircle is related to this time constant. This M'' maximum is also observed in the frequency domain in the M'' spectra.

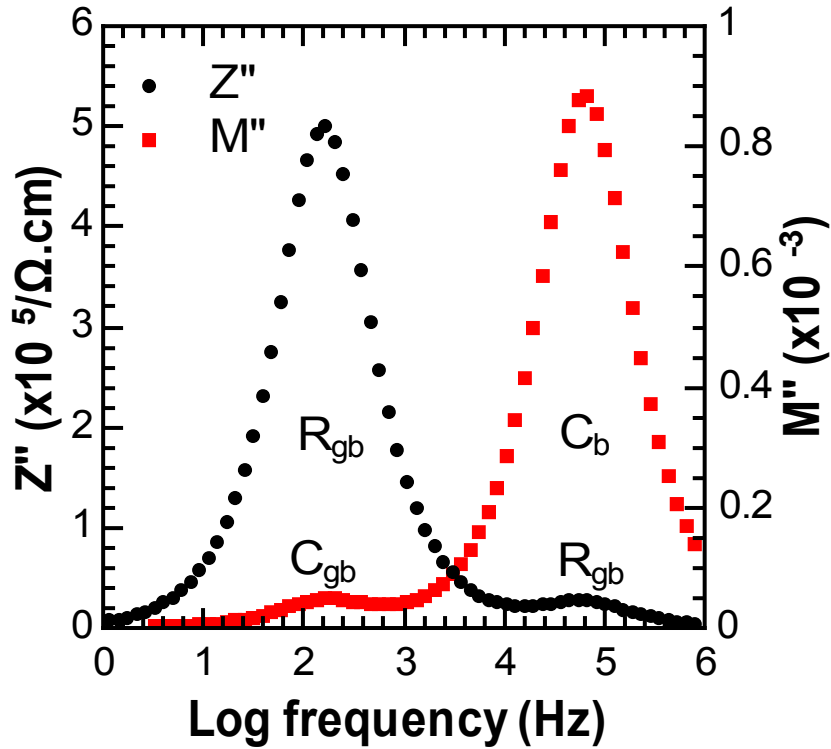


Figure 2.13: The corresponding Debye responses show in the frequency domain for M'' and Z'' vs. frequency

The frequency associated with the maxima in the complex modulus and corresponding maxima in the M'' spectra is related to ω_{max} by the relationship:

$$\omega_{max} = 2\pi f_{max} = (RC)^{-1} = \tau^{-1} \quad \text{Equation 2.27}$$

This means at the peak maximum in the complex modulus and spectra that:

$$\omega_{max}RC = 1 \quad \text{Equation 2.28}$$

And consequently by simplifying Equation 2.25 the capacitance of the RC element can be determined from the magnitude of the imaginary M''_{max} by $M''_{max} = \frac{\epsilon_0}{2C}$.

In summary, this gives a number of different methods for quickly determining the capacitance of a sample *i.e.*, by fitting the M^* and determining the reciprocal of the diameter of each component (M'), determining the magnitude of the imaginary component at M''_{max} or by evaluating the M' intercepts for each component.

Based on the capacitance of each RC element and the relationship with the peak maximum (Equation 2.28) the resistance of the RC element also can be estimated assuming a Debye-like response.

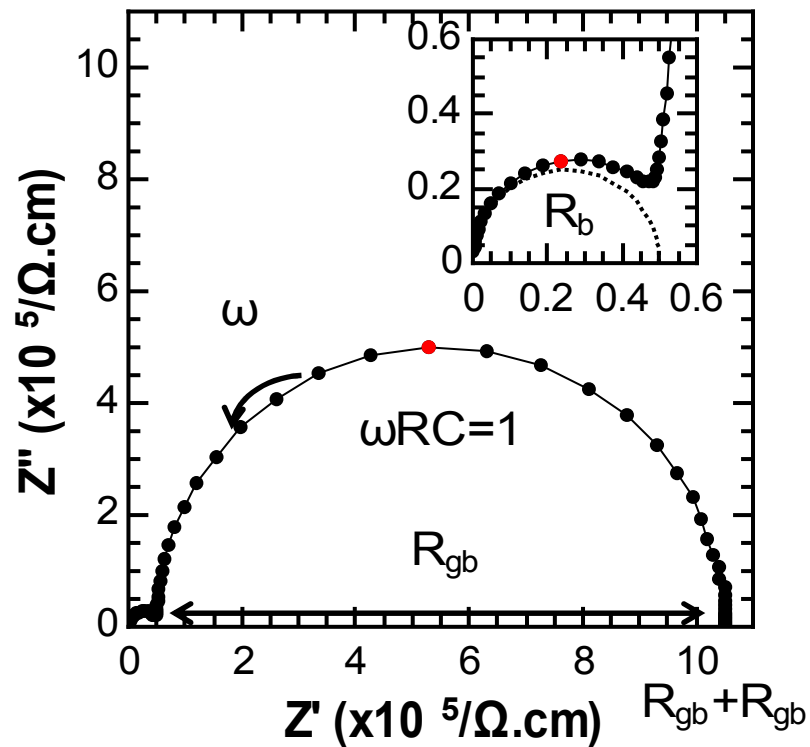


Figure 2.14: A simulated plot of the complex plot, Z^* showing two electrical components comprising of the bulk and grain boundary

In this case, the complex impedance plot (Figure 2.14), shows two semi-circular arcs that relate to the two resistive components in Figure 2.10. The larger semicircle relates to the larger more resistive grain boundary and the smaller that of the bulk (Equation 2.26). The diameter each semicircle represents the resistance of each component. Thus, the high intercept on the x-axis represents the resistance of all the components (*i.e.* $R_{gb}+R_b$) and the total sample resistance.

Reiterating for the Z^* case, each component has a different time constant which related to the angular frequency (ω), as discussed earlier (Equation 2.16 and Equation 2.27) and Z'' maximum is also observed in the frequency domain in the Z'' spectra (Figure 2.13).

Equation 2.26 can be simplified due to the relationship expressed in Equation 2.28 and consequently the resistance of the RC element can be determined from the magnitude of the imaginary Z''_{max} by $Z''_{max} = R \left[\frac{1}{2} \right]$.

In summary, this gives a number of different methods for quickly determining the resistance of a sample *i.e.* by fitting the Z^* and determining the diameter of each component (Z'), determining the magnitude of the imaginary component at Z''_{max} or by evaluating the Z' intercepts for each component.

Based on the resistance of each RC element and the relationship with the peak maximum (Equation 2.28) the capacitance of the RC element also can be estimated assuming a Debye-like response.

2.7.7 Activation energies

The conductivity (σ) of an electroactive region can be determined by taking the reciprocal of the associated resistance ($\sigma = 1/R$). Activation energies (E_a) associated with the conduction processes can then be determined utilizing the Arrhenius type behaviour of the conductivity of the samples:

$$\sigma = \sigma_0 e^{-\frac{E_a}{kT}} \quad \text{Equation 2.29}$$

σ_0 is a pre-exponential factor, k is the Boltzman constant and T is the absolute temperature in Kelvin. Often in the literature the $\log_{10} \sigma$ vs. $1000/T$ in Kelvin is plotted therefore the activation energy of a single process can be calculated from multiplying the gradient by -0.1984.

2.8 Scanning electron microscopy with energy-dispersive x-rays

The microstructure of the samples was observed using Jeol JSM-5600 scanning electron microscope (SEM) fitted with an energy dispersive x-ray system (EDX) and a Jeol JSM-6700 F scanning electron microscope with a backscattering electron (BSE) detector. This allowed for the determination of the grain size, grain size distribution, and assessment of the homogeneity of the sample.

2.9 References

1. D. C. Arnold, K. S. Knight, F. D. Morrison and P. Lightfoot, *Phys. Rev. Lett.*, 2009, **102**, 027602.
2. P. Hewat and C. Buchsbaum, Fachinformationszentrum (FIZ) Karlsruhe National Institute of Standards and Technology (NIST), 2008.
3. V. Pecharsky and P. Zavalij, *Fundamentals of Powder Diffraction and Structural Characterization of Materials*, Springer US, 2005.
4. V. K. Pecharsky and P. Y. Zavalij, *Fundamentals of Powder Diffraction and Structural Characterization of Materials*, Springer US, 2009.
5. in *Powder Diffraction: Theory and Practice*, eds. R. E. Dinnebier and S. J. L. Billinge, The Royal Society of Chemistry, 2008, pp. p001-p004.
6. J. Cui, Q. Huang and B. H. Toby, *Powder Diffr.*, 2006, **21**, 71-79.
7. How ISIS works - in depth, <http://www.isis.stfc.ac.uk/about-isis/how-isis-works---in-depth4371.html>, Accessed 03/08/2012, 2012.
8. S. Webb, Science and Technology Facilities Council ISIS, Rutherford Appleton Laboratory, 2009, p. 25.
9. A. Albinati and B. T. M. Willis, *J. Appl. Crystallogr.*, 1982, **15**, 361-374.
10. R. J. D. Tilley, *Crystals and Crystal Structures*, John Wiley & Sons, 2006.
11. A. C. Larson and R. B. Von Dreele, Los Alamos National Laboratory 1994.
12. R. A. Young, *The Rietveld method*, Oxford University Press, Chester, England, 1995.
13. B. Toby, *J. Appl. Crystallogr.*, 2001, **34**, 210-213.
14. H. Rietveld, *J. Appl. Crystallogr.*, 1969, **2**, 65-71.
15. N. J. Kidner, N. H. Perry, T. O. Mason and E. J. Garboczi, *J. Am. Ceram. Soc.*, 2008, **91**, 1733-1746.
16. J. T. S. Irvine, D. C. Sinclair and A. R. West, *Adv. Mater.*, 1990, **2**, 132-138.
17. K. J. Andrew, *J. Phys. D: Appl. Phys.*, 1999, **32**, R57.
18. A. R. West, D. C. Sinclair and N. Hirose, *J. Electroceram.*, 1997, **1**, 65-71.
19. P. G. Bruce and A. R. West, *J. Electrochem. Soc.*, 1983, **130**, 662-669.
20. P. Lunkenheimer, V. Bobnar, A. V. Pronin, A. I. Ritus, A. A. Volkov and A. Loidl, *Phys. Rev. B*, 2002, **66**, 052105.
21. D. Johnson, Scribner Associates, Inc, 1990.
22. F. D. Morrison, *Synthesis and Electrical Characterisation of Lanthanum Doped Barium Titanate*, PhD Thesis, University of Aberdeen, 1999

A Magnetically driven dielectric: $\text{Bi}_{0.5}\text{La}_{0.5}\text{FeO}_3$

3.1 Introduction

The focus of this chapter is on the detailed structural analysis of the lanthanum doped bismuth ferrite $\text{Bi}_{0.5}\text{La}_{0.5}\text{FeO}_3$ (BLFO50). The analysis is based on variable temperature powder neutron diffraction (PND) and impedance spectroscopy (ac-IS). The analysis shows BLFO50 adopts the Shubnikov space group $Pn'ma'$ with a G_2 -type magnetic unit cell. More importantly, the analysis has highlighted a structural distortion linked to the relative permittivity of the sample with an accompanied change in the magnitude of the FeO_6 octahedral tilt. The distortion of the octahedra corresponds to an A-site displacement along the c -axis with a “scissoring distortion” of the FeO_6 octahedra. The tilt behaviour is unusual due to an increasing in-phase tilt with temperature. The orthorhombic distortion within the system is driven by magnetostriction with the onset of antiferromagnetic ordering resulting in an invariant c -axis (Invar effect) and anisotropic displacement of the A-site Bi^{3+} and La^{3+} along the a -axis.

As highlighted in Chapter 1, BiFeO_3 is a widely studied multiferroic due to its ferroelectric (high $T_c \sim 1083 - 1103$ K) and (anti)ferromagnetic properties ($T_N \sim 643$ K).¹ However, applications and the study of bulk BiFeO_3 are hindered by electrical conductivity due to non-stoichiometry and thermal metastability.² The electrical properties and thermal stability of the perovskite phase can be improved by the substitution of the volatile Bi^{3+} with rare earths e.g. La^{3+} ($\text{Bi}_{1-x}\text{La}_x\text{FeO}_3$).

Prior research has shown that the substitution of Bi^{3+} with La^{3+} results in a diverse range of phases at lower doping levels (i.e., $x < 0.5$), which has been reported in a number of studies including those of Rusakov *et al.*³ and Troyanchuk *et al.*⁴ These experimental observations have been supported by first principle calculations showing that several of the $\text{Bi}_{1-x}\text{La}_x\text{FeO}_3$ phases are quasi-degenerate in energy over a wide compositional range.⁵ Rusakov *et al.* observed the following phase sequence under ambient conditions as a function of composition for samples prepared by solid-state methods: $R3c$ ($0 < x < 0.1$) \rightarrow ' $Pnam$ ' ($x = 0.18$) \rightarrow incommensurate ' $Imma$ ' ($0.19 < x < 0.30$) \rightarrow $Pnma$ ($x > 0.5$).³

This series of phase mixtures complicates the study of the materials at lower doping levels ($x < 0.5$) and has driven the current analysis to review a composition at higher La^{3+} content where the phase mixture is predominately single phase. A number of authors suggest that this critical concentration is $x \gtrsim 0.5$ where the $Pnma$ structure is adopted.^{3, 4} This is the GdFeO_3 -type structure adopted by the parent LaFeO_3 phase and indeed all rare earth orthoferrites.⁶ It is also the structure adopted by BiFeO_3 in the high temperature paraelectric phase.^{7, 8} This phase is commonly refined in the alternate crystallographic setting $Pbnm$.⁹⁻¹¹

To understand the effect of A-site doping and why a complex sequence of phases is observed at lower doping ($x < 0.5$), changes in the crystal structure as a function of composition must be fully understood. These structural changes affect the properties of the material and occur, in large part, due to the electronic difference between Bi^{3+} and La^{3+} i.e., the presence of the Bi^{3+} lone pair. The effects on the electronic and magnetic properties in the $\text{Bi}_{1-x}\text{La}_x\text{FeO}_3$ have been studied by a number of authors substituting Bi^{3+} with La^{3+} on the A-site with respect to A-site displacements that this causes.

The local, short-range magnetic order of BiFeO_3 is a G-type antiferromagnet with a weak canted moment.¹ However, the overall long-range magnetic order is more complicated and is based on an incommensurate spin cycloid of the antiferromagnetic sub-lattice.¹ The cycloid structure propagates along the $[110]$ direction and has a repeat distance of about 62-64 nm.^{12, 13} This repeat distance can be influenced by changes on the A-site. Le Bras *et al.* show that in polycrystalline samples, lanthanum substitution within the $R3c$ phase ($x > 0.15$) results in a destabilising effect on the spiral magnetic structure and an increased predisposition to change to a collinear magnetic structure.¹⁴

Density functional theory (DFT) calculations, corroborated by experimental evidence, also suggest that within the $R3c$ phase the degree of the ferroelectric off-centering along the c -axis of the unit cell (hexagonal setting) is reduced with increasing lanthanum content.¹⁵ This influences the ferroelectric properties, significantly reducing the ferroelectric polarisation with doping concentration. However, it does allow samples to sustain higher electric fields by reducing leakage currents.¹⁵

Another example of the effect of A-site substitution is the observation of the incommensurate '*Imma*' phase ($x = 0.25$) which has been suggested based on a synchrotron powder X-ray diffraction study.³ The incommensurate modulation is suggested to be due to competing dipole-dipole interactions caused by antipolar displacements of Bi^{3+} and octahedral tilting.³ Anisotropic refinements of the *Imma* phase suggest a displacement along the *b*-axis.³

3.2 Experimental Method

The sample preparation for the PND experiment is outlined in the chapter 2. PND experiments were performed on the HRPD diffractometer at the ISIS neutron spallation source using two different sample environments. The experimental temperature range was from 50 K to 900 K: measurements from 50 K to 550 K were carried out in a cryofurnace and those from 450 K up to 900 K were performed in a furnace, resulting in some temperature overlap. Patterns were collected at 450 K, 500 K, 550 K in the furnace and 550 K in the cryofurnace allowing for a comparison between the different sample environments. Rietveld refinements were carried out using the general structural analysis system (GSAS) and its associated graphical user interface program (EXPGUI).^{16, 17} Data from the 'backscattering' detector bank ($2\theta \sim 168^\circ$) on the HRPD instrument was used for refinements ($0.7 < d < 2.6 \text{ \AA}$), although 30° bank data was examined for evidence of persistence of magnetic ordering.

3.3 Preliminary structural analysis

The PND data show that BLFO50 occurs predominantly as the $Pnma$, $GdFeO_3$ -type phase (94 wt% at room temperature). The final Rietveld refinement at 300 K is shown in Figure 3.1. The major phase has been refined with a G_z -type magnetic structure with the moment constrained along the c -axis, described with the Shubnikov symmetry $Pn'ma'$. The unit cell parameters and atom positions for the main $Pn'ma'$ phase at 300 K are shown in Table 3.1

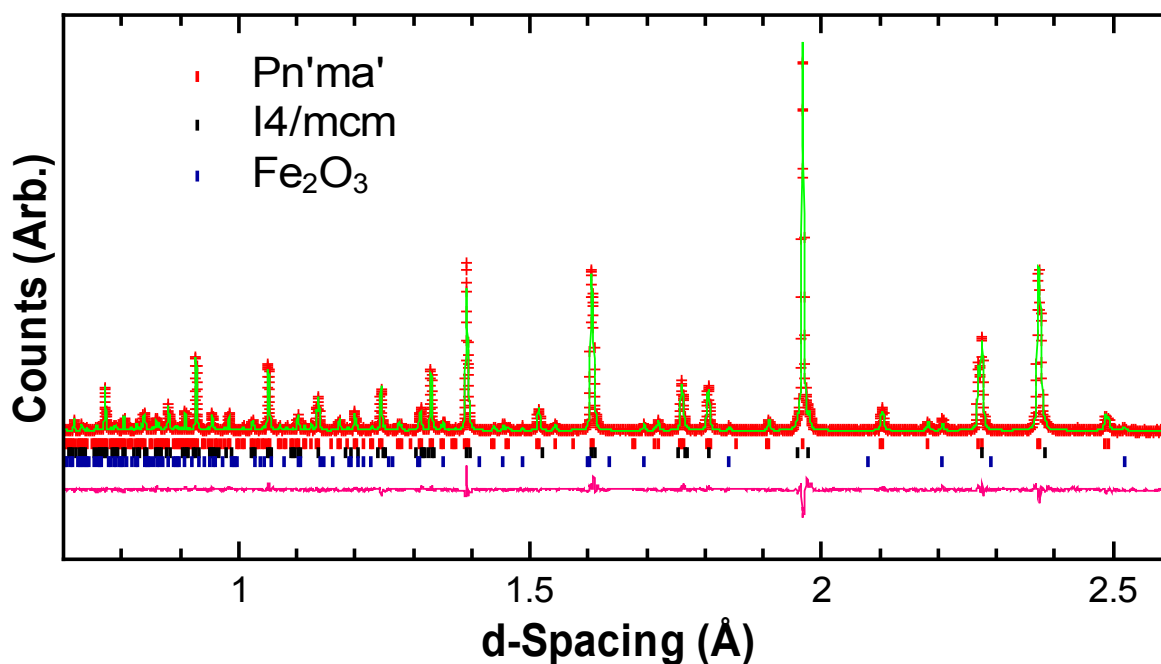


Figure 3.1: Rietveld refinement profile of PND data at 300 K; $\chi^2 = 5.157$, $wR_p = 0.0614$, $R_p = 0.0544$. Tick marks represent Bragg reflections for $Pn'ma'$ (top) and $I4/mcm$ (middle) $Bi_{0.5}La_{0.5}FeO_3$ phases and Fe_2O_3 (bottom).

Table 3.1 Atomic coordinates of the $Pn'ma'$ phase of $Bi_{0.5}La_{0.5}FeO_3$ refined from PND data at 300 K; $a = 5.5749(8)$ Å, $b = 7.8653(1)$ Å, $c = 5.5551(1)$ Å.

Site	x	y	z	U_{iso} (Å ²)
Bi/La	0.0233(3)	0.25	-0.0072(7)	0.0199(3)
Fe	0	0	0.5	0.00209(16)
O1	0.4872(5)	0.25	0.0741(6)	0.0118(3)
O2	0.2835(3)	0.0409(3)	-0.2834(3)	0.0118(3)

There are two minor secondary phases within the BLFO50 sample. The first is an I-centred phase (< 5 wt%), which transforms to *Pnma* as a function of temperature. The phase has been refined as tetragonal, *I4/mcm* ($a = b \sim \sqrt{2} a_p$, $c \sim 2 a_p$) although it is probably the incommensurate orthorhombic (*'Imma'*) phase reported at lower concentrations of lanthanum by Rusakov *et al.*³ This secondary phase gradually transforms to *Pnma* with temperature and is no longer present above *circa* 650 K. This gradual decrease in the phase fraction of the *I4/mcm* phase with temperature can be seen in Figure 3.2. The other minor secondary phase is a trace amount of Fe₂O₃ (*ca.* 1 wt%) remains constant in all refinements.

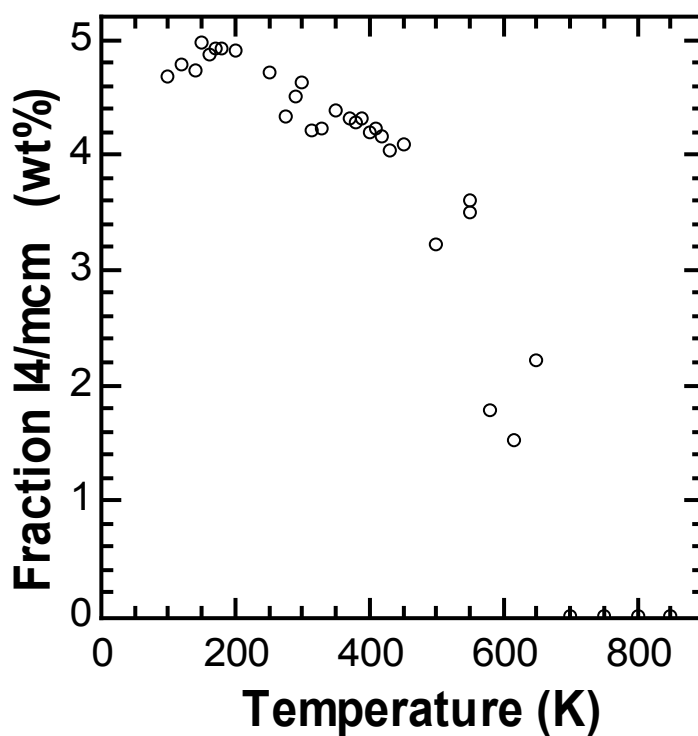


Figure 3.2: Phase fraction of the *I4/mcm* phase in wt% as a function of temperature showing gradual transformation to *Pn'ma'*. The phase fraction was determined from a 3-phase Rietveld refinement of PND data.

The following images of the ceramic microstructure of BLFO50 (Figure 3.3) were taken on a Jeol JSM-6700 F scanning electron microscope (SEM) where the images (a-c) correspond to a single area of a pellet selected for its concentration of Fe_2O_3 .

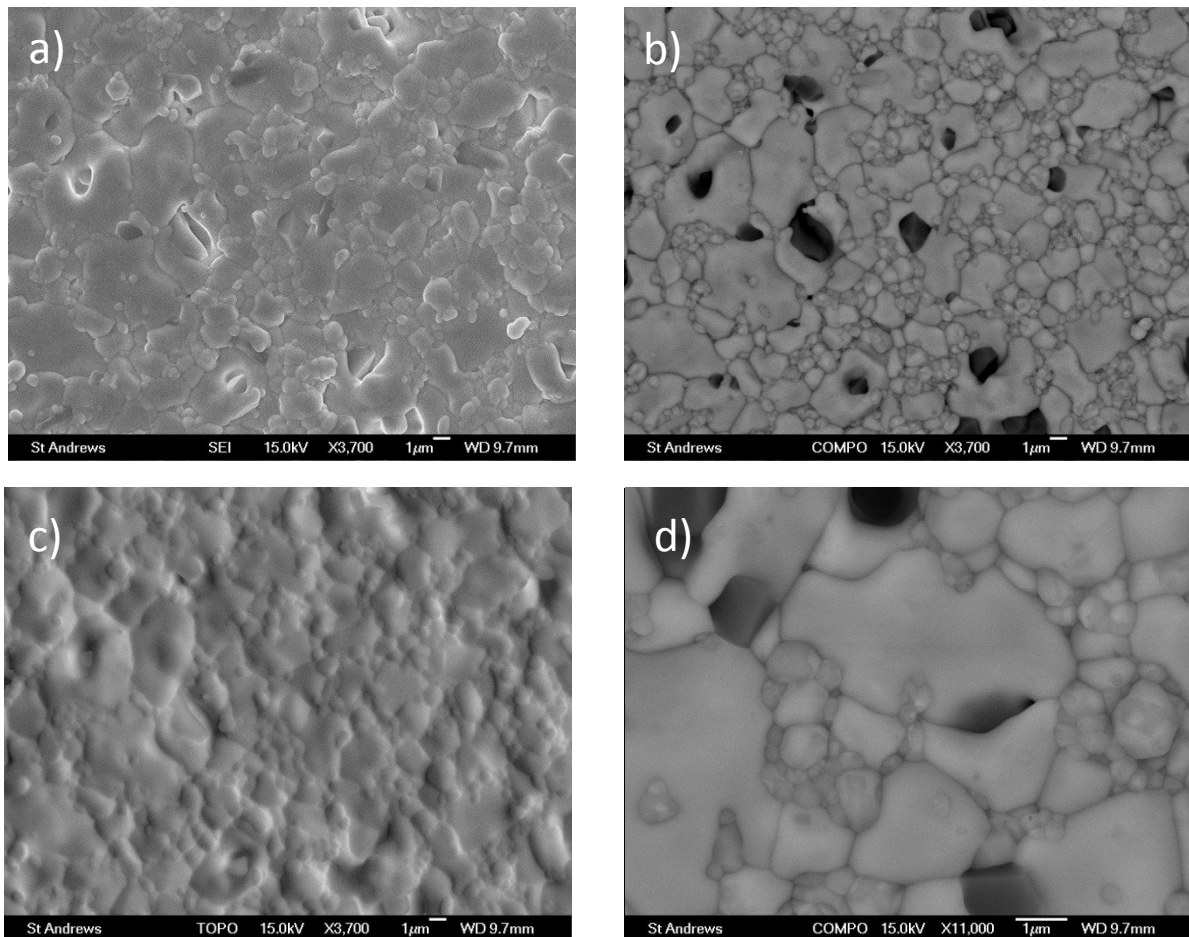


Figure 3.3: A standard SEM image (a), with the composition (b) and topography (c) highlighted with backscattering of a single area. (d) compositional analysis image of the grains .

In the standard SEM image, Figure 3.3 (a), the presence of the Fe_2O_3 is not clear, partly due to the build-up of surface charge. However, the compositional (COMPO) and topographical (TOPO) images, figures 3.3. (b) and (c), respectively, clearly show that what could have been interpreted as pores are actually grains of Fe_2O_3 . The micrographs also indicate a dense ceramic material with few pores has been formed. Figure 3.3 (d) also indicates that the composition does not change across the grains of the main phase indicated by a uniform coloration and the grain sizes are 1-10 μm across.

As stated previously, the major phase has been refined with a G_2 -type magnetic unit cell; however there is the possibility of a minor off-axis magnetic component which is typically found in rare earth orthoferrites.¹⁸ Attempts were made to refine any off-axis magnetic component but were unsuccessful. Direct measurement of a net moment due to spin canting using conventional *ac* susceptibility measurements are hampered by the trace presence of weakly ferromagnetic hematite. Hematite loses this magnetic order above 950 K¹⁹, which is above the Néel temperature of the $Pn'ma'$ phase.

The net magnetic moment of the $Pn'ma'$ phase was determined from the magnetic refinements of the PND data. The temperature dependence of this net magnetisation is shown in Figure 3.4.

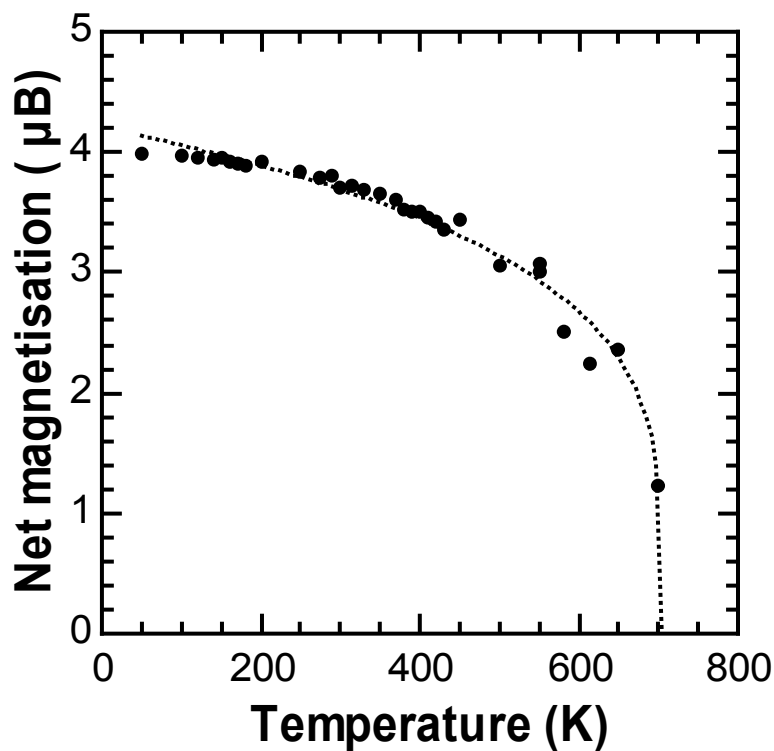


Figure 3.4: Net magnetisation (along c) as a function of temperature as determined from Rietveld refinement of PND data. Dotted black line represents a fit of the magnetic data to a power law.

The magnetic data was fitted using a power law, (Equation 3.1) assuming a mean field approximation giving a Néel temperature, $T_N = 704 \pm 3$ K and exponent $\alpha = 0.24 \pm 0.04$.

$$F(T) \propto (T_N - T)^\alpha \quad \text{Equation 3.1}$$

The loss of antiferromagnetic order *circa* 704 K is supported by the persistence of magnetic reflections up to 700 K and is consistent with previously reported values for this composition and is similar to the parent LaFeO_3 with $T_N \sim 743$ K as reported elsewhere.^{11, 20-22} A predominately magnetic reflection (110) can be seen in Figure 3.5 which has been shown to persist at least up to 700 K and is no longer present at 750 K i.e. above T_N .

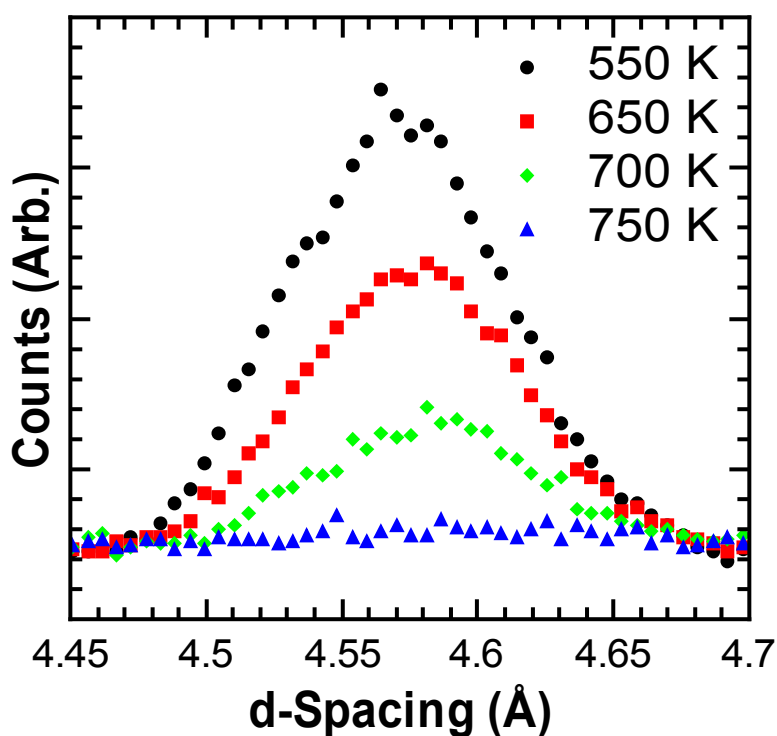


Figure 3.5: Magnetic reflection (110) at $d = 4.55$ Å which persists up to 700 K

Other magnetic models were tried at a range of temperatures to ensure that the direction of the magnetic moment was correctly assigned (G_x, G_y). All models included the $I4/mcm$ and Fe_2O_3 secondary phases.

Table 3.2: Summary of the magnetic and non-magnetic refinements of BLFO50 at 300 K.

	Space group	χ^2	wR_p	R_p
G_z	$Pn'ma'$	5.157	0.0618	0.0544
G_y	$Pn'm'a$	5.320	0.0628	0.0600
G_x	$Pnma$	5.922	0.0663	0.0622
(non-magnetic)	$Pnma$	8.488	0.0793	0.0810

The data presented in Table 3.2 shows that at 300 K the G_z model produces the best fit of the diffraction data and that the inclusion of a magnetic model significantly improves the quality of the fit. This contribution of the magnetic fit is shown in the Rietveld refinement plot in Figure 3.6 where the magnetic model has been removed and all other parameters are no longer refined.

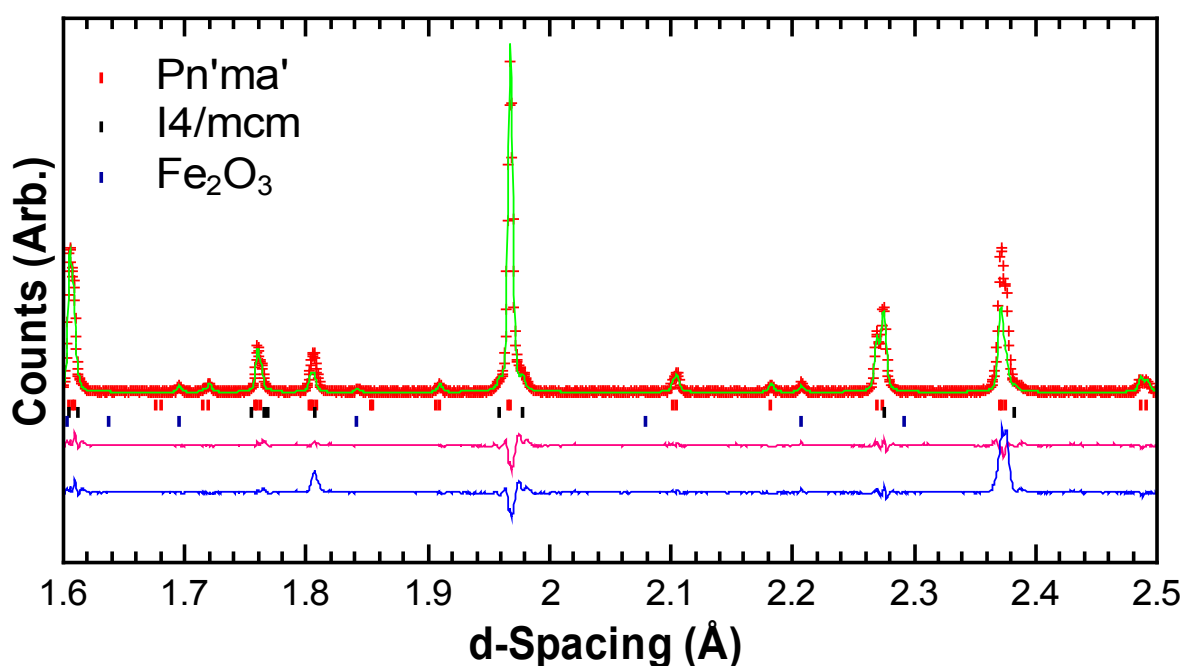


Figure 3.6: Rietveld refinement profile at 300 K with the main $GdFeO_3$ -type phase refined without ($Pnma$) and with the magnetic contribution ($Pn'ma'$). Tick marks represent: $Pnma$ (red); $I4/mcm$ (black); and Fe_2O_3 (blue). Residuals for fits with (top) and without (bottom) magnetic contributions are shown for comparison; goodness-of-fit parameters for the $Pnma$ fit are $\chi^2 = 9.914$, $wR_p = 0.0861$ and $R_p = 0.0853$ compared to $\chi^2 = 5.157$, $wR_p = 0.060$ and $R_p = 0.0544$ for $Pn'ma'$.

The unit cell parameters (Figure 3.7) clearly show an increasing orthorhombic distortion with increasing temperature up to ca. 700 K due to the invariant c -axis relative to the expansion of a and b .

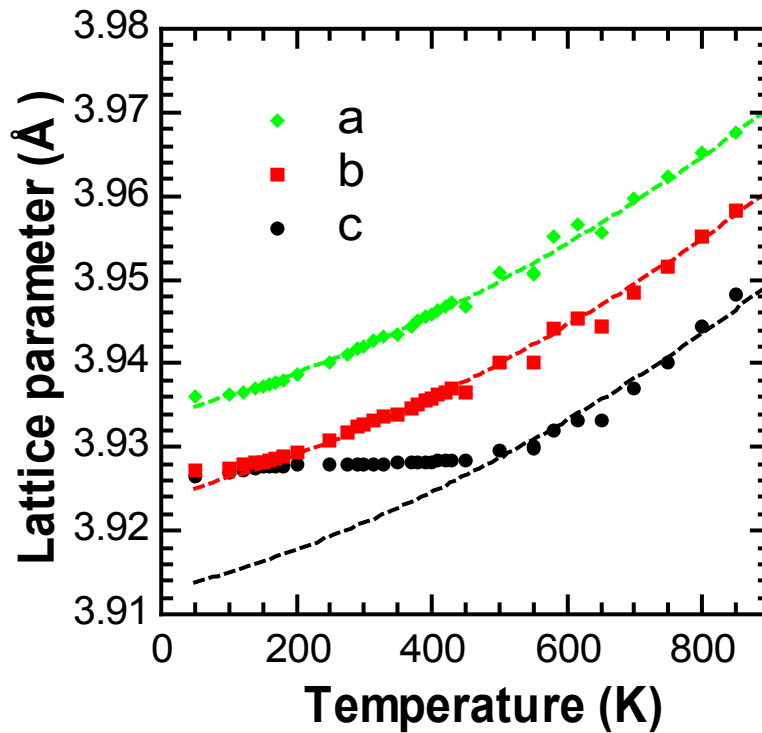


Figure 3.7: Reduced (pseudo cubic) cell lattice parameters as a function of temperature ($a = \sqrt{2} a_p$, $b = 2 a_p$, $c = \sqrt{2} a_p$, where a_p represents lattice parameter of the cubic aristotype); dashed lines represent fit to a second order polynomial.

This orthorhombic strain can be represented by the distortion parameter, D_o , defined as:

$$D_o = \frac{|a - c|}{2(a + c)} \quad \text{Equation 3.2}$$

Above ca. 700 K, the c -axis increases and D_o decreases (Figure 3.8.) This unusual behaviour of increasing orthorhombic strain with increasing temperature will be discussed further in light of the magnetic behaviour and the contributions of the various structural distortion modes allowed at both the A-site and involving the BO_6 octahedra which are presented below.

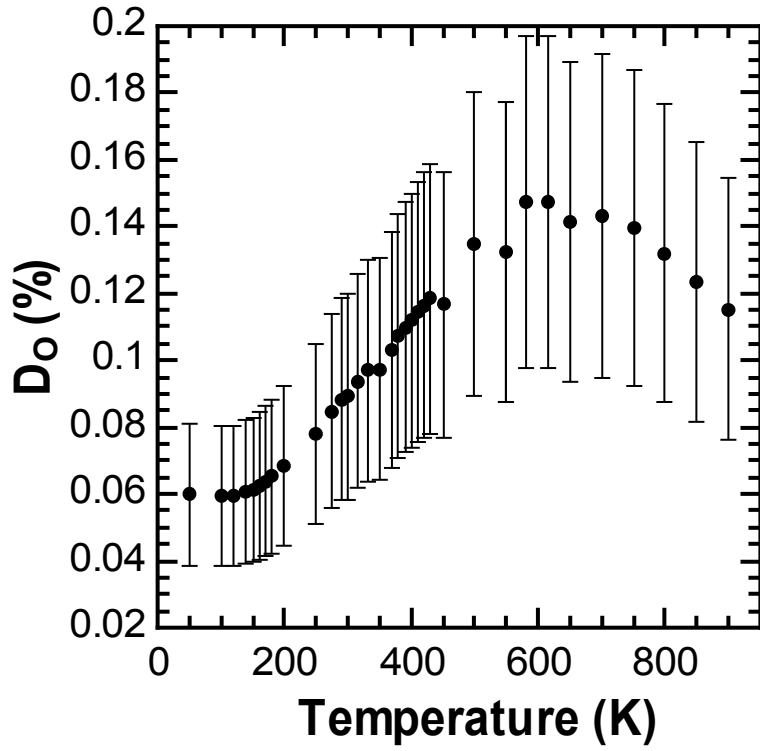


Figure 3.8: Orthorhombic strain, D_o , as a function of temperature.

3.4 Electrical Properties

Ac immittance spectroscopy of insulating BLFO50 samples reveals only a single electroactive region as shown by the presence of a single Debye peak in both the imaginary modulus and impedance spectra (Figure 3.9) and at the same (single) relaxation time (*i.e.*, the peak maxima occur at the same frequency).

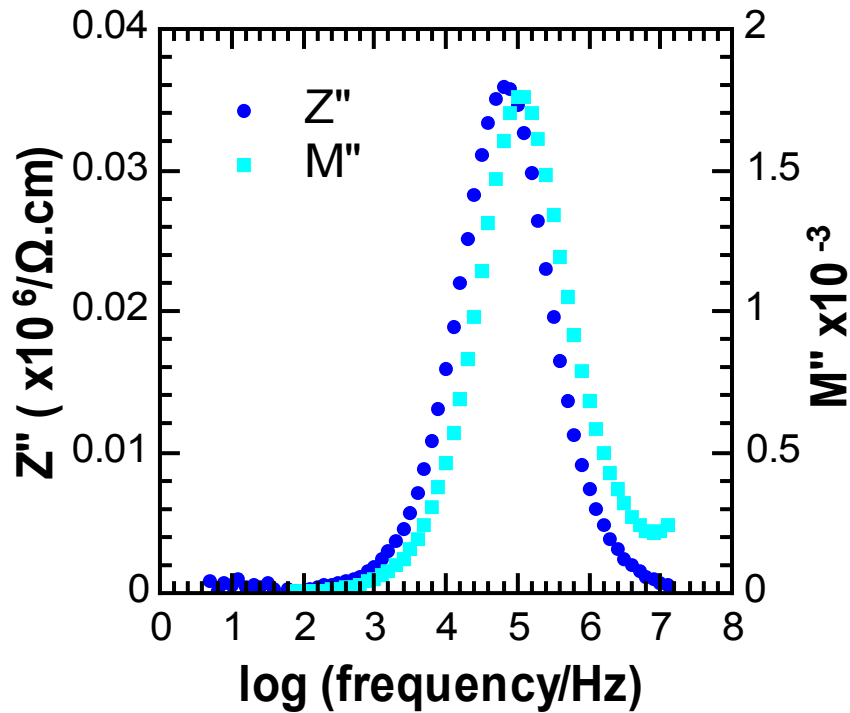


Figure 3.9: Imaginary electric modulus, M'' and impedance, Z'' , spectroscopic plots at 575 K

Assuming Debye behaviour, the modulus peak maximum, M''_{max} , is related to the capacitance and dielectric permittivity by:

$$M''_{max} = \frac{\epsilon_0}{2C} = \frac{1}{2\epsilon_r} \quad \text{Equation 3.3}$$

From the magnitude of the M'' peak this response has an associated C of *ca.* 21 pFcm⁻¹ at 520 K and is therefore associated with the bulk response.²³ With increasing temperature the M'' peak increases in magnitude slightly indicating that the bulk capacitance is falling (Figure 3.10a); the peak is also displaced to higher frequency due to decreasing resistance, Equation 3.4.

$$\tau = RC = \frac{1}{2\pi f_{max}}$$

Equation 3.4

The permittivity of the bulk response can be determined more accurately from the diameter of the semi-circular arc in the complex electric modulus, M^* , (Figure 3.10b) which scales directly as $1/\epsilon_r$. Permittivity data extracted in this manner is shown in Figure 3.11 along with data obtained from fixed frequency measurements (discussed below).

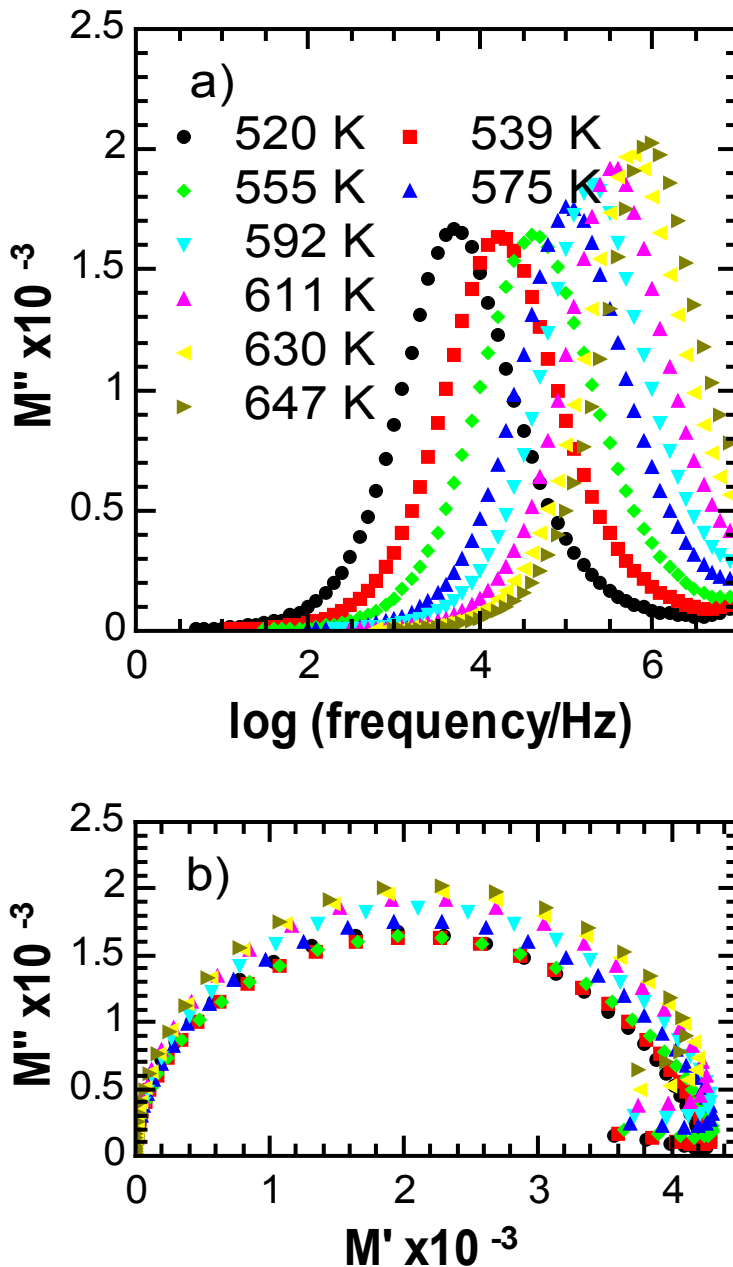


Figure 3.10: M'' spectra (a) and complex electric modulus, M^* plane plots (b) as a function of temperature. (Symbols in part (b) are as in (a)).

Fixed frequency capacitance (C_p) and loss ($\tan \delta$) measurements were performed on insulating samples of BLFO50. Based on the brick layer model and assuming an equivalent of two parallel RC elements in series (representing bulk and grain boundary regions) the parallel capacitance as a function of frequency results in two frequency independent plateaus.²⁴ The parallel capacitance (C_p) measured in the high frequency plateau contains contributions from both the bulk (C_b) and grain boundary (C_{gb}) capacitances according to:

$$C_p = (C_{gb}^{-1} + C_b^{-1})^{-1} \quad \text{Equation 3.5}$$

The magnitudes of the capacitive responses expected in a coarse grained ceramic with thin, well-defined grain boundaries are such that $C_{gb} \gg C_b$ and therefore the overall contribution of the grain boundary to the total capacitance is small. The total high frequency capacitance is therefore a close approximation of the bulk response. Provided high temperature data can be used to validate the assumption that $C_{gb} \gg C_b$ then fixed frequency measurements at lower temperatures can be used to probe the bulk response. The single semi-circular bulk arc in M^* , Figure 3.10b, and the analysis described above indicates that $C_{gb} \gg C_b$ is indeed the case for our samples and so bulk permittivities were calculated from C_p at 10 kHz, 100 kHz and 1 MHz using the relationship:

$$C_p = \epsilon_r \epsilon_0 \frac{A}{d} \quad \text{Equation 3.6}$$

where A is the electrode area, d is the separation between the electrodes (sample thickness), ϵ_0 is the permittivity of free space, and ϵ_r the bulk relative permittivity. Bulk permittivity and loss data as a function of temperature are shown in Figure 3.11.

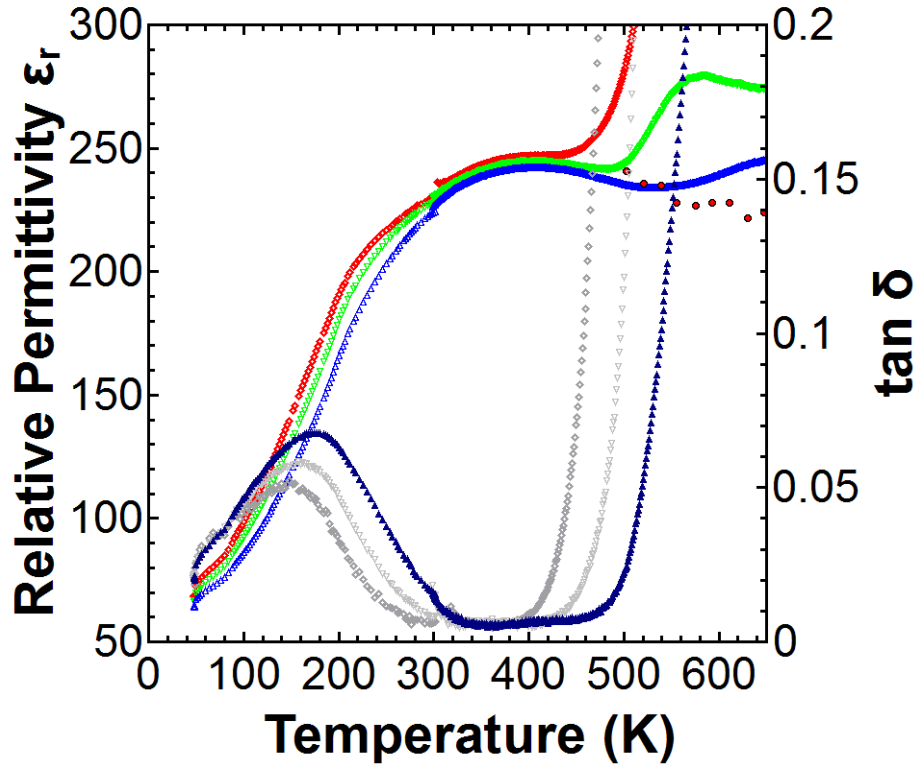


Figure 3.11: Relative dielectric permittivity (ϵ_r) and loss ($\tan \delta$) as a function of temperature at 10 kHz, 100 kHz, and 1 MHz (left to right at high temperature). Bulk values obtained from electric modulus data are included circles black outline.

The permittivity increases from *ca.* 60 at low temperature increasing to *ca.* 240 at 300 K, the loss data exhibit a peak around 100 K (Figure 3.11). The data show only a weak frequency dispersion over the majority of the temperature range; the dramatic upturn in the data at the highest temperatures (particularly evident in the dielectric loss) is due to the increasing contribution of the grain boundary/electrode response and is not intrinsic. Bulk permittivities determined from M^* plots, Figure 3.10b confirm this and indeed show that in fact the bulk permittivity decreases slightly above 500 K. This dielectric behaviour must be intrinsically linked to some structural change, which is not immediately obvious from the data presented in Figure 3.7. A more in-depth structural analysis is required.

Bulk conductivities, $\sigma_b (=R_b^{-1})$ were estimated using two methods: a) bulk resistances (R_b) were obtained from the frequency maxima (f_{\max}) in the M'' spectra plots and capacitance from the complex modulus (M^*) plane plots using the relationships in Equation 3.3 and Equation 3.4. b) The bulk resistance was also extracted more directly from the complex impedance (Z^*) plane plots.

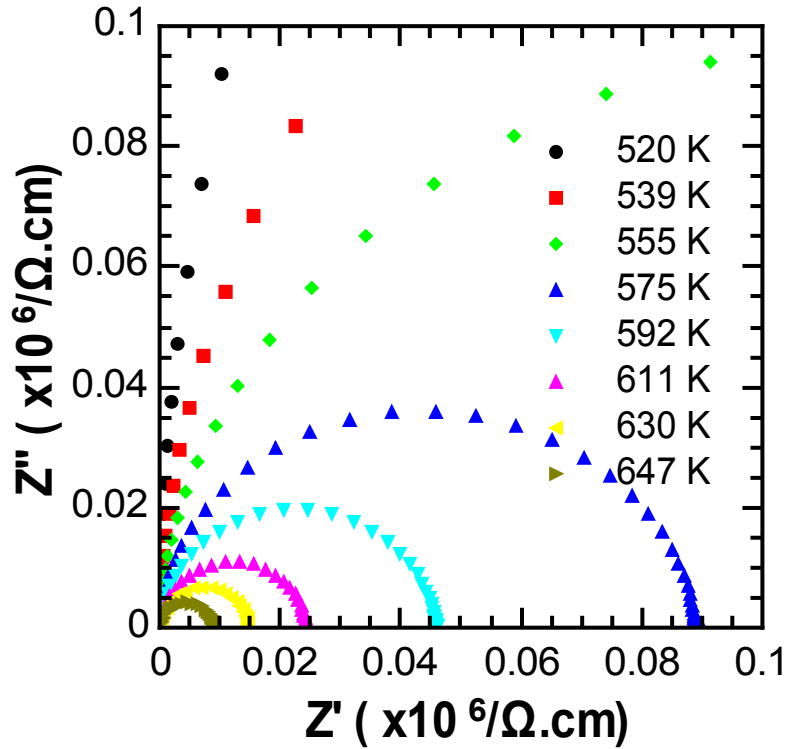


Figure 3.12: Complex impedance plane plots as a function of temperature from which the bulk resistance can be determined.

The conductivities determined by each method are in good agreement, with both showing the expected temperature dependence (Figure 3.13) described by the Arrhenius expression:

$$\sigma_b = \sigma_0 e^{-\frac{E_a}{kT}} \quad \text{Equation 3.7}$$

The bulk activation energy (E_a) is ~ 1.2 eV which is consistent with other experimental studies^{25, 26} and is characteristic of electronic conduction dominated by the presence of oxygen vacancies.²⁷

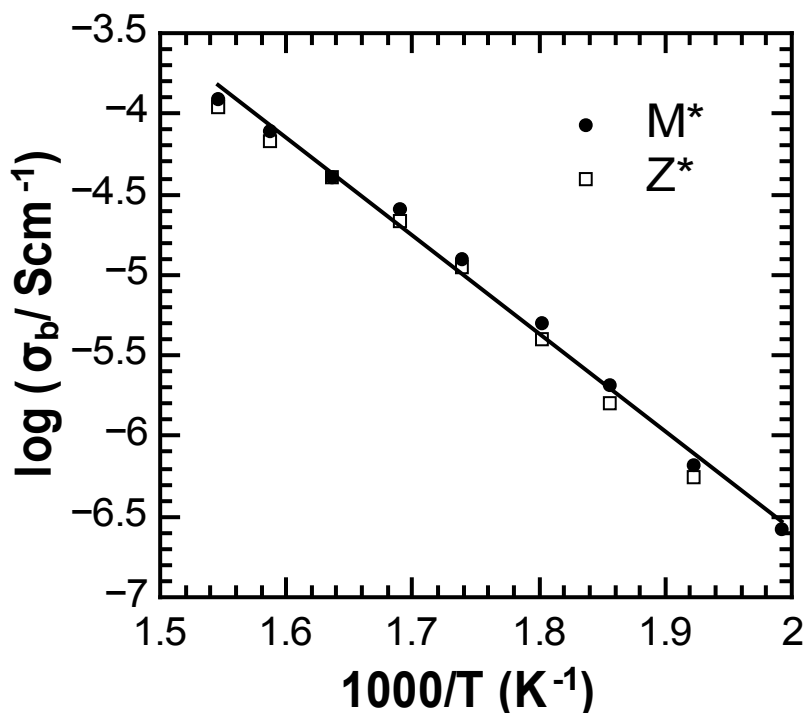


Figure 3.13: Arrhenius plot of bulk conductivities determined from both Z^* and M^* data; activation energy, $E_a = 1.20$ eV ($R^2 = 0.992$)

3.5 Correlation of structure and dielectric response

In order to correlate the change in dielectric response (Figure 3.11) with crystallographic changes, the crystal structures as derived from Rietveld refinements were analysed both in terms of a conventional ‘bond length/bond angle’ description and also using the online structural analysis tool ISODISTORT.^{16, 28} The latter allows comparison of a distorted structure with its parent aristotype (an ideal, cubic perovskite in this case) in terms of specific symmetry-allowed modes which are derived from irreducible representations of the parent symmetry. The advantage of this method is that it allows both the nature and degree of each particular distortion mode to be determined in a completely decorrelated manner – for example, ‘octahedral tilt’ modes and ‘cation displacement’ modes can be seen independently. The seven variable atomic coordinates (Table 3.1) can therefore equivalently be represented by seven distinct symmetry-adapted modes.

The initial Rietveld analysis showed that the FeO_6 octahedra become more regular in terms of Fe-O bond lengths up to *ca.* 300 K; at the same time, however, the internal octahedral angles (O-Fe-O angles) show deviation from an ideal octahedron (Figure 3.14).

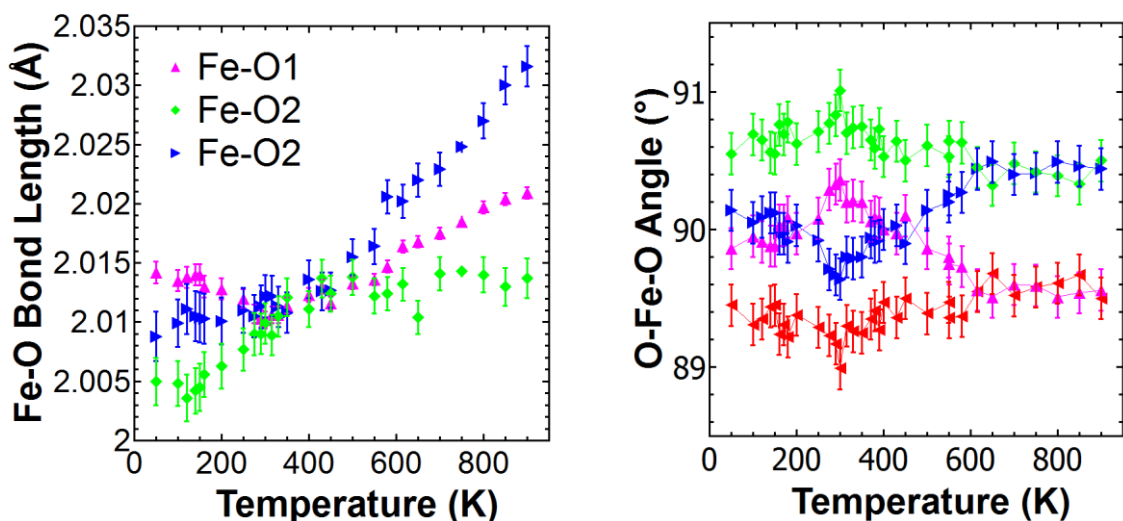


Figure 3.14: Fe-O bond lengths as a function of temperature as determined from Rietveld refinements of PND data (left); internal octahedral (O1-Fe-O2) angles as a function of temperatures indicating a maximum distortion at *ca.* 300 K corresponding to the change in dielectric permittivity (right)

This distortion can be represented clearly using the ISODISTORT software, where it is described by the R_5^+ modes relating to the A-site and oxygen positions. The R_5^+ [A site] mode represents a displacement of the A-site cation along the *c*-axis, Figure 3.15. In terms of the degree of distortion these modes should be viewed as absolute magnitudes and therefore the R_5^+ [A site] at 300 K represents the most distorted state relative to the ideal model. This corresponds to the broad maximum in the relative permittivity (Figure 3.11)

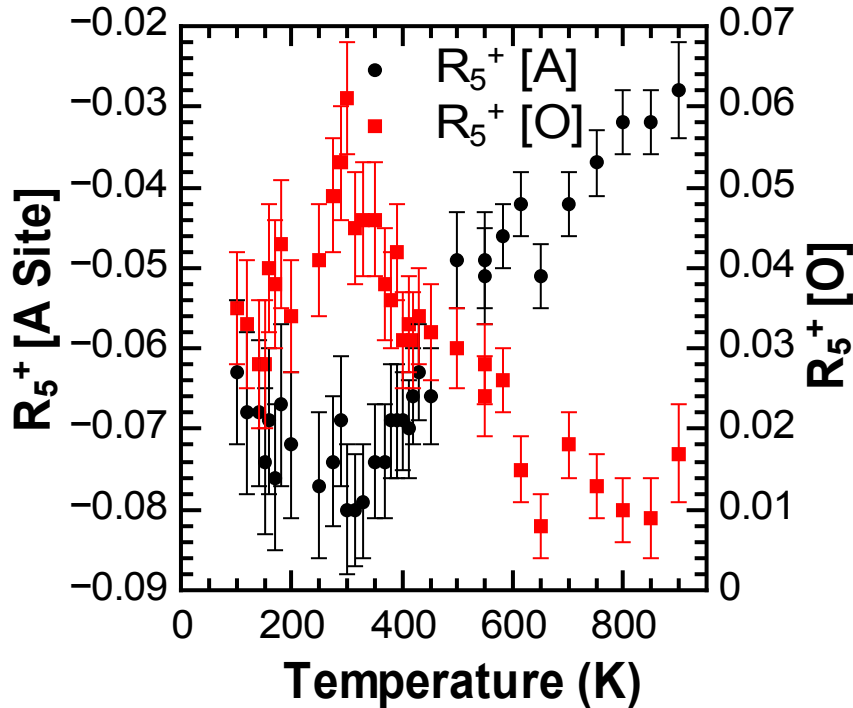


Figure 3.15: ISODISTORT displacement (R_5^+) modes as a function of temperature showing the A-site displacement along the c axis (R_5^+ [A site]) and displacements of the axial oxygens (O1) along c and the equatorial oxygen (O2) along b (R_5^+ [O]).

This A-site displacement also correlates with the R_5^+ [O] mode, which is a ‘scissoring’ distortion of the FeO_6 octahedra (where the axial oxygens (O1) are allowed to move along c while the equatorial oxygens (O2) displace along b). This means that while the octahedra are becoming more regular in terms of bond lengths, they are increasingly distorted in terms of O-Fe-O angles. This distortion, together with the displacement on the A-site leads to an increase in the relative permittivity. This higher than expected permittivity (based on a Clausius-Mosotti summation of ionic polarisabilities) is attributed by a number of authors to a “rattling” effect of the displaced cation and local variations in the Lorentz field²⁹⁻³¹

The Fe-O-Fe angles were also reviewed, which shows that the angles are becoming equivalent at temperatures corresponding to the maximum in the relative permittivity (Figure 3.16). These changes in Fe-O-Fe angles are influenced by changes in the degree of octahedral tilting as well as the distortion in the octahedra, which are both important effects influencing the overall polarisation. However, it is quite instructive to look at structural effects in terms of two distinct types of symmetry modes, with the tilt modes being discussed below.

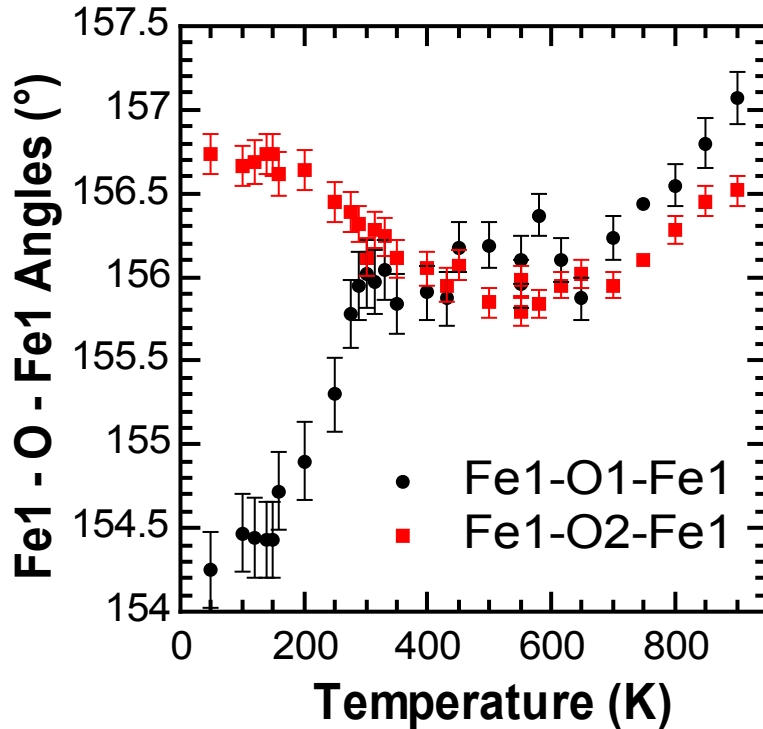


Figure 3.16: Changes in the Fe-O-Fe angles with temperature, which are linked to the changes in the two octahedra tilt modes and the octahedral distortion.

3.6 Structural response to magnetic ordering

As shown in Figure 3.7 the reduced lattice parameters show an increase in the orthorhombic distortion, D_o , with increasing temperature with broad maximum in the range *ca.* 650 - 700 K (Figure 3.8). This change correlates with the paramagnetic - antiferromagnetic transition and the onset of a magnetostrictive effect.

The paramagnetic to antiferromagnetic transition in $\text{Bi}_{1-x}\text{La}_x\text{FeO}_3$ has been studied for compositions $0.18 \leq x \leq 0.35$.³ The authors detected a weak anomaly near 670-675 K using DSC and suggested it was associated with an AFM to paramagnetic phase transition that has been reported elsewhere by Roginskaya and Polomska.^{3, 21, 22} The onset of AFM order in BLFO50 occurs slightly higher *circa* 700 K, as indicated by the fit of the magnetic data (Figure 3.4) and the presence of a predominantly magnetic reflection in the neutron diffraction data at 4.55 Å d-spacing (Figure 3.5). This onset of magnetic order influences the orthorhombic distortion, as described in more detail below.

The initial approach studied changes in the Fe-O-Fe angles. These angles are influenced by the two possible tilting modes, the in-phase (M_3^+) and anti-phase (R_4^+) tilts shown in Figure

3.17. The Fe-O1-Fe angle is influenced by the anti-phase tilt whereas the Fe-O2-Fe angle is influenced by both tilts. An increasing Fe-O-Fe angle suggests a decreasing octahedral tilt, neglecting minor octahedral distortion effects. The increase in the Fe-O1-Fe angle up to *ca.* 300 K therefore suggests a decrease in the anti-phase tilt, while the decrease in the Fe-O2-Fe angle suggests an *increase* in the in-phase tilt. The Fe-O-Fe angles (Figure 3.16) also suggest that there is a significant change at *ca.* 700 K where both the Fe-O-Fe angles start to increase with temperature. However, the Fe-O-Fe angles are also influenced by distortions of the octahedra i.e., both tilts *decrease* above this temperature. It is therefore necessary to study the separate influences of each of the tilts on the Fe-O-Fe angles.

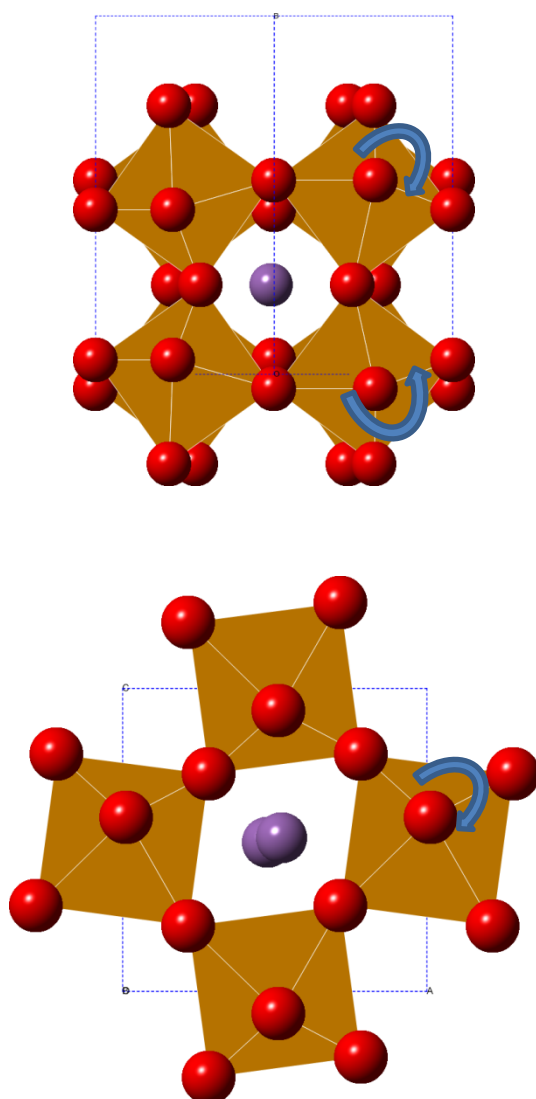


Figure 3.17: Anti-phase (R) rotation about $[101]$ (top) and the in-phase (M) rotation about $[010]$, (bottom) with respect to the $Pnma$ unit cell.

With increasing temperature the anti-phase tilt (R_4^+ [O] mode) decreases, as expected, while the in-phase tilt (M_3^+ [O] mode) increases with temperature reaching a broad maximum round 650-750 K (Figure 3.18). The increase in the in-phase tilt as a function of temperature is highly unusual and has only been observed as a very weak effect over a limited temperature range, for example in KCaF_3 .³² The effect in this case is considerably larger and occurs over a more extensive temperature range.

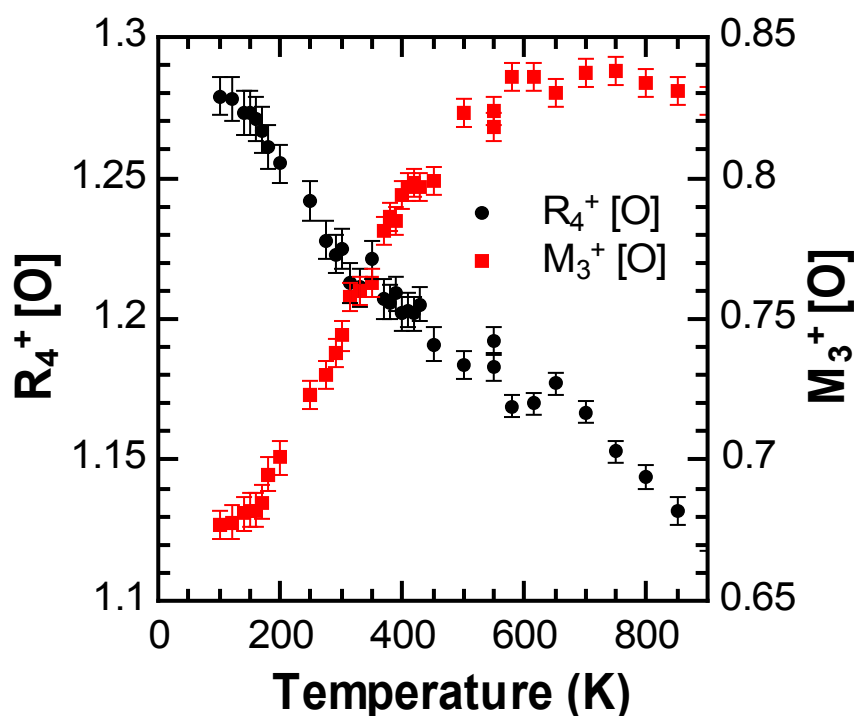


Figure 3.18: ISODISTORT tilt modes as a function of temperature showing the in-phase rotation about [010] (M_3^+) and anti-phase tilt (R_4^+) about [101].

The high-temperature plateau in M_3^+ appears at first-sight approximately in-line with the maximum in the orthorhombic distortion (Figure 3.8). However, the correlation is not exact and, although the in-phase tilt is obviously linked to the orthorhombic distortion it cannot be, in itself, the cause of the distortion (a strictly rigid in-phase tilt would leave the lattice metrically tetragonal, but destroys the crystallographic 4-fold axis). Instead, a non-zero D_o parameter is typically associated with A-site cation displacements in GdFeO_3 -type perovskites.³³ In the $\text{Bi}_{1-x}\text{La}_x\text{FeO}_3$ system, a number of studies have examined the A-site behaviour and have shown that the structural features are closely associated with A-site displacements.^{3, 15} The displacement of the A-site cation along the a -axis is represented in

ISODISTORT by the X_5^+ [A site] mode (Figure 3.19). The X_5^+ mode increases up to *ca.* 650 K where it reaches a maximum before falling with temperature. This correlates strongly with the orthorhombic distortion (Figure 3.19). This clearly shows that displacements on the A-site cause the increasing orthorhombic distortion, with a secondary correlation being the increase in the M_3^+ in-phase tilt. The X_5^+ symmetry mode also has a much smaller oxygen displacement contribution.

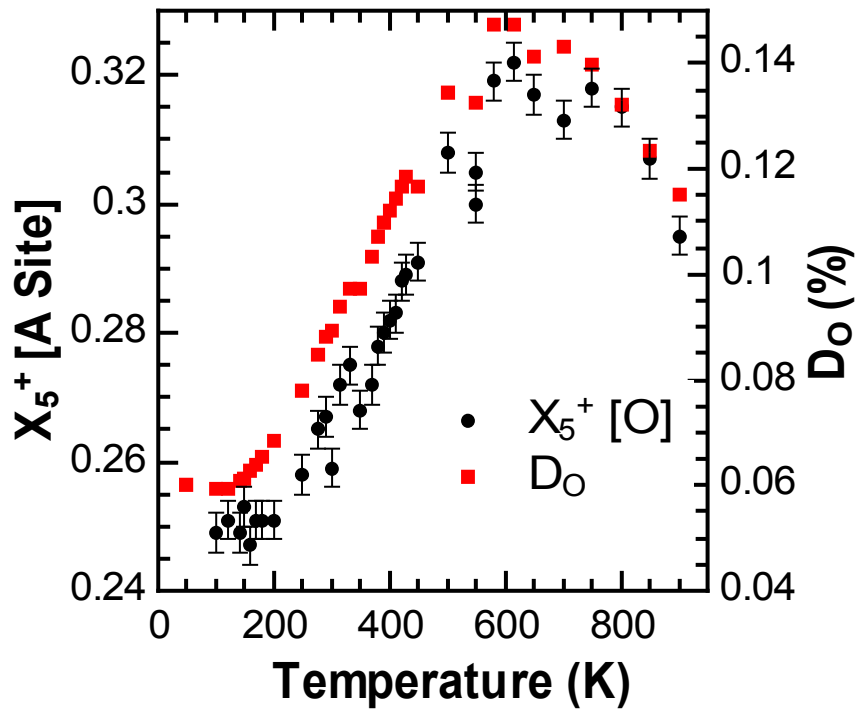


Figure 3.19: ISODISTORT X_5^+ [A site] displacement mode as a function of temperature describing A-cation displacements along the a -axis and the correlation with orthorhombic strain, D_0 .

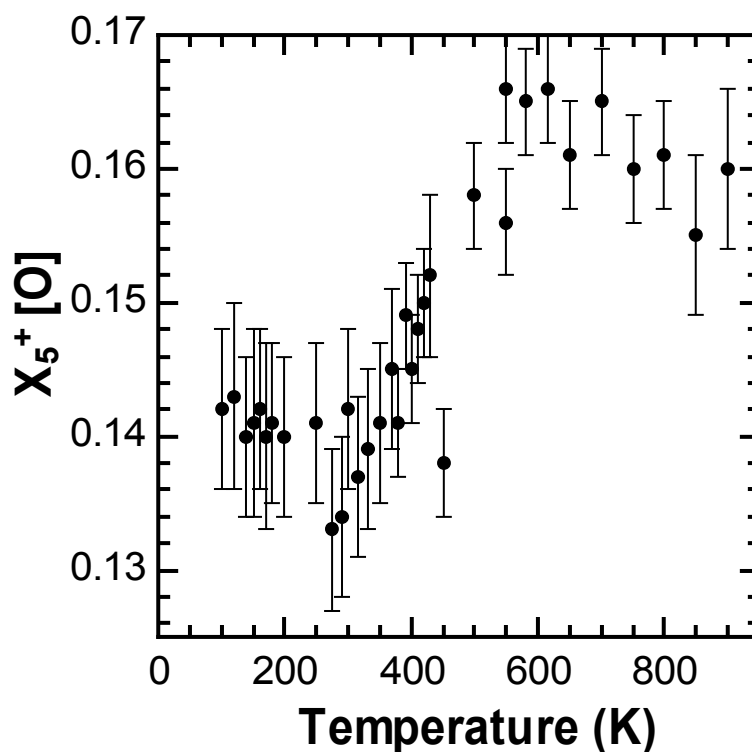


Figure 3.20: ISODISTORT oxygen displacement ($X_5^+ [O]$) mode as a function of temperature.

The structural models so far have considered the bismuth and lanthanum sites as equivalent. Although Bi^{3+} and La^{3+} have similar ionic radii when comparing equivalent coordination numbers³⁴ the effect of the Bi^{3+} lone pair has not been considered (The 8-coordinate Bi^{3+} and La^{3+} ionic radii according to Shannon are 1.170 Å and 1.160 Å, respectively).³⁴ The relative displacements of Bi^{3+} and La^{3+} away from the refined, 'averaged' A-site position are likely to be slightly different. These local displacements in the A-site will be evident in the atomic displacement parameters. If the atom positions are refined anisotropically the direction of the most significant relative displacement can be inferred. Anisotropic refinements of the A-site confirm that there is indeed a relative displacement of the two cations, and show that the U_{11} parameter is significantly larger than U_{22} and U_{33}

Figure 3.21).

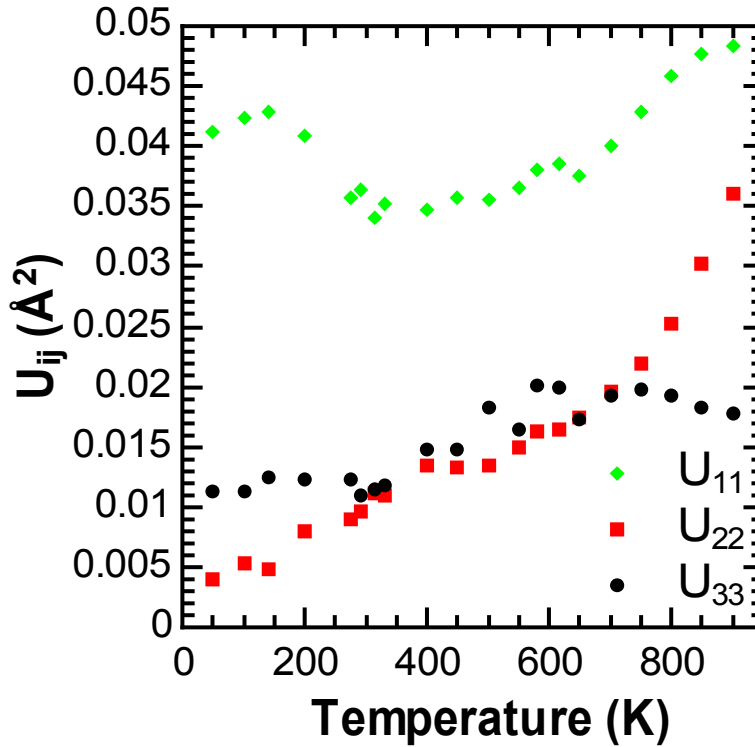


Figure 3.21: Anisotropic atomic thermal displacement parameters (U_{ij}) as a function of temperature along a (U_{11}), b (U_{22}), and c (U_{33}) axes.

The U_{11} parameter corresponds to the displacement along the a -axis of the $Pnma$ unit cell. This suggests that the bismuth and lanthanum sites are not equivalent and are displaced along the a -axis but by differing degrees. This displacement direction is consistent with the change in the orthorhombic distortion X_5^+ mode which shows the overall displacement in the a -axis based on isotropic refinements (Figure 3.19). The X_5^+ mode tracks with the orthorhombic distortion, representing the average displacement of the lanthanum and bismuth site, which it is now possible to demonstrate, is due in part to relative displacements of the two cations away from a single A-site.

The structural analysis so far has shown a displacement of the A-site cations along the a -axis, where the local positions of La and Bi are not perfectly equivalent. This A-site displacement drives the anomalous change in the orthorhombic distortion, with the secondary effect of the abnormal in-phase tilt behaviour. However, the underlying cause of the invariant lattice parameter c below ~ 650 K has not yet been addressed. The c -axis corresponds with the direction of the net magnetisation. This is linked to a magnetostrictive effect within the material. On cooling from the paramagnetic region the sample orders

antiferromagnetically at $T_N \sim 704$ K. Eventually the net magnetisation increases to such a point where it has a detectable effect on the lattice parameters such that there is a deviation in the c -axis from the expected near-linear thermal contraction (as observed in the a - and b -axes) to temperature invariant behaviour, the so-called “Invar effect”.³⁵ A similar effect has been observed in other perovskites such as LaTiO_3 which adopts the GdFeO_3 structure ($Pbnm$) where with the onset of antiferromagnetic (G_x) order results in an increase in the orthorhombic splitting with a changing $\sqrt{2}$ axis set.³⁶ Magnetostrictive effects have also been observed with various ruthenate based perovskites.^{35, 37, 38}

Typically, a Debye-Grüneisen approximation can be applied to the unit cell volume to determine the contraction of the unit cell with decreasing temperature. This accounts for the internal energy of the system and models the volume change with temperature giving the hypothetical contraction of the unit cell in the paramagnetic state. The relative difference between the unit cell parameters or volume of the hypothetical paramagnetic state and that observed experimentally gives the contribution of the magnetostrictive effect. To do this fit an estimation of the Grüneisen parameter needs to be determined from measurements of the heat capacity, bulk modulus and volume expansion.³⁹ As a simple alternative, we have approximated the thermal expansivity of the unit cell parameters with a second order polynomial, $y = A_2 T^2 + A_1 T + A_0$. The $Pn'ma'$ magnetic space group contains no magnetic component along x , and so the a lattice parameter was fitted over the entire temperature range (50 K to 900 K). The polynomial with $A_2 = 2.2174 \times 10^{-8}$, $A_1 = 2.0900 \times 10^{-5}$ and $A_0 = 3.9338$ gave a good fit to the observed data, Figure 3.7. The b - and c -axes were also fitted to this polynomial with the A_2 and A_1 coefficients fixed and A_0 allowed to vary; the b -axis was fitted over the entire temperature range but the c -axis was only fitted in the near-linear, high temperature region and then extrapolated to lower temperatures, Figure 3.7. $A_0 = 3.9240$ and 3.9127 for b - and c -axes, respectively.

The difference between the predicted contraction and the experimental values, Figure 3.7, represents the contribution from magnetostriction. The magnitude of magnetostrictive strain (ω_x) of the lattice can be calculated as:

$$\omega_x = \frac{x_{exp} - x_{calc}}{x_{calc}} \quad \text{Equation 3.8}$$

where x_{exp} and x_{calc} are the experimentally determined and calculated lattice parameters, respectively. The temperature dependence of magnetostriction is shown in Figure 3.22, and clearly indicates an increasing c -axis strain with decreasing temperature, reaching *ca.* 0.3 % at 50 K, which is of a similar magnitude to other magnetostrictive oxides.^{35, 37, 38} There is no detectable strain in the other axes.

In summary, BLFO50 adopts the orthorhombic $GdFeO_3$ crystal structure described by $Pnma$ symmetry. On cooling from high temperature it magnetically orders to a G-type antiferromagnet (T_N *ca.* 704 K) with the moment along the c -axis (Shubnikov symmetry $Pn'ma'$). The magnetic ordering results in: (a) a magnetostrictive (Invar) effect along the magnetic c axis; (b) antipolar A-site displacements along the a -axis; and (c) contrasting changes in in-phase and anti-phase octahedral tilts. The net result is a strong orthorhombic distortion which decreases on further cooling. At *ca.* 300 K the A-site displacements and a distortion of the octahedra caused by a scissoring of the axial oxygens results in a change in the dielectric permittivity from *ca.* 250 to 180.

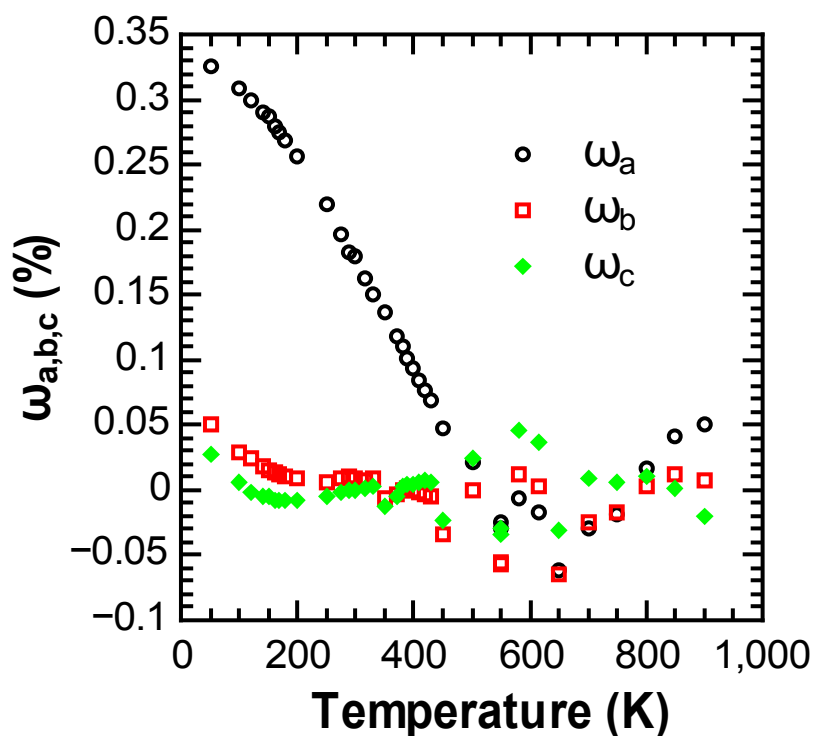


Figure 3.22: Magnetostrictive contribution (ω_x) as a function of temperature showing increasing strain in the c -axis below the Néel temperature.

3.7 Conclusions

A combination of electrical and structural analysis using temperature dependent powder neutron diffraction has shown that lanthanum doped BiFeO₃ of composition Bi_{0.5}La_{0.5}FeO₃ is a wide band gap semiconductor with its structural and dielectric behaviour driven by the magnetic properties. The detailed crystallographic changes (structural distortions) were analysed using both conventional Rietveld analysis and the symmetry mode ISODISTORT tool. The analysis shows that the material adopts the GdFeO₃ structure and that there is an unusual orthorhombic distortion with an increasing in-phase tilt as a function of increasing temperature. This distortion has a corresponding antipolar atomic displacement of the A-site where the lanthanum and bismuth are displaced by different degrees along the *a*-axis. The orthorhombic distortion is caused by the onset of antiferromagnetic order ($T_N \sim 704$ K) and a magnetostrictive Invar effect along the magnetic *c*-axis. The magnetically driven tilt combines with distortion of the octahedra and a corresponding A-site displacement along the *c*-axis resulting in a change in the dielectric permittivity at *ca.* 300 K. The use of symmetry-mode analysis (*via* ISODISTORT), in addition to conventional crystallographic analysis, presents a new paradigm for investigation of structure-property relationships in lanthanide doped BiFeO₃.

3.8 References

1. G. Catalan and J. F. Scott, *Adv. Mater.*, 2009, **21**, 2463-2485.
2. W. Eerenstein, F. D. Morrison, J. Dho, M. G. Blamire, J. F. Scott and N. D. Mathur, *Science*, 2005, **307**, 1203.
3. D. A. Rusakov, A. M. Abakumov, K. Yamaura, A. A. Belik, G. Van Tendeloo and E. Takayama-Muromachi, *Chem. Mater.*, 2011, **23**, 285-292.
4. I. O. Troyanchuk, M. V. Bushinsky, D. V. Karpinsky, O. S. Mantytskaya, V. V. Fedotova and O. I. Prochnenko, *Phys. Status Solidi B*, 2009, **246**, 1901-1907.
5. O. E. González-Vázquez, J. C. Wojdeł, O. Diéguez and J. Íñiguez, *Phys. Rev. B*, 2012, **85**, 064119.
6. M. Marezio, J. P. Remeika and P. D. Dernier, *Acta Crystallogr. Sect. B: Struct. Sci.*, 1970, **26**, 2008-2022.
7. D. C. Arnold, K. S. Knight, G. Catalan, S. A. T. Redfern, J. F. Scott, P. Lightfoot and F. D. Morrison, *Adv. Funct. Mater.*, 2010, **20**, 2116-2123.
8. D. C. Arnold, K. S. Knight, F. D. Morrison and P. Lightfoot, *Phys. Rev. Lett.*, 2009, **102**, 027602.
9. T. Peterlin-Neumaier and E. Steichele, *J. Magn. Magn. Mater.*, 1986, **59**, 351-356.
10. S. Geller and E. A. Wood, *Acta Cryst.*, 1956, **9**, 563-568.
11. S. Acharya, J. Mondal, S. Ghosh, S. K. Roy and P. K. Chakrabarti, *Mater. Lett.*, 2010, **64**, 415-418.
12. I. Sosnowska, T. P. Neumaier and E. Steichele, *J. Phys. C*, 1982, **15**, 4835.
13. J. M. Moreau, C. Michel, R. Gerson and W. J. James, *J. Phys. Chem. Solids*, 1971, **32**, 1315-1320.
14. G. Le Bras, P. Bonville, D. Colson, A. Forget, N. Genand-Riondet and R. Tourbot, *Physica B*, 2011, **406**, 1492-1495.
15. J. H. Lee, H. J. Choi, D. Lee, M. G. Kim, C. W. Bark, S. Ryu, M. A. Oak and H. M. Jang, *Phys. Rev. B*, 2010, **82**, 045113.
16. A. C. Larson and R. B. Von Dreele, Los Alamos National Laboratory 1994.
17. B. Toby, *J. Appl. Crystallogr.*, 2001, **34**, 210-213.
18. R. L. White, *J. Appl. Phys.*, 1969, **40**, 1061-1069.
19. A. Aharoni, E. H. Frei and M. Schieber, *Phys. Rev.*, 1962, **127**, 439-441.
20. D. Treves, *J. Appl. Phys.*, 1965, **36**, 1033-1039.
21. Yu. E. Roginskaya, Yu. E. Venevtsev, S. A. Fedotov and G. S. Zhdanov, *Sov. Phys. Crystallogr.*, 1964, **8**, 490.
22. M. Polomska, W. Kaczmarek and Z. Pajak, *Phys. Status Solidi*, 1974, **23**, 567.
23. J. T. S. Irvine, D. C. Sinclair and A. R. West, *Adv. Mater.*, 1990, **2**, 132-138.
24. A. R. West, D. C. Sinclair and N. Hirose, *J. Electroceram.*, 1997, **1**, 65-71.
25. P. Pandit, S. Satapathy and P. K. Gupta, *Physica B*, 2011, **406**, 2669-2677.
26. K. Kalantari, I. Sterianou, S. Karimi, M. C. Ferrarelli, S. Miao, D. C. Sinclair and I. M. Reaney, *Adv. Funct. Mater.*, 2011, **21**, 3737-3743.
27. M. S. Islam, *J. Mater. Chem.*, 2000, **10**, 1027-1038.

28. B. J. Campbell, H. T. Stokes, D. E. Tanner and D. M. Hatch, *J. Appl. Crystallogr.*, 2006, **39**, 607-614.
29. R. D. Shannon, *J. Appl. Phys.*, 1993, **73**, 348-366.
30. R. A. Parker, *Phys. Rev.*, 1961, **124**, 1713-1719.
31. S. Roberts, *Phys. Rev.*, 1951, **81**, 865-868.
32. K. S. Knight, C. N. W. Darlington and I. G. Wood, *Powder Diffr.*, 2005, **20**, 7-13.
33. P. Woodward, *Acta Crystallogr. Sect. B: Struct. Sci.*, 1997, **53**, 44-66.
34. R. D. Shannon, *Acta Crystallogr. Sect. A: Found. Crystallogr.*, 1976, **32**, 751-767.
35. T. Kiyama, K. Yoshimura, K. Kosuge, Y. Ikeda and Y. Bando, *Phys. Rev. B*, 1996, **54**, R756-R759.
36. A. C. Komarek, H. Roth, M. Cwik, W. D. Stein, J. Baier, M. Kriener, F. Bourée, T. Lorenz and M. Braden, *Phys. Rev. B*, 2007, **75**, 224402.
37. B. Dabrowski, M. Avdeev, O. Chmaissem, S. Kolesnik, P. W. Klamut, M. Maxwell and J. D. Jorgensen, *Phys. Rev. B*, 2005, **71**, 104411.
38. R. Ranjan, A. Senyshyn, R. Garg and H. Boysen, *J. Appl. Phys.*, 2011, **109**, 073908-073907.
39. K. S. Knight, *J. Electroceram.*, 2011, **27**, 143-153.

Superexchange mediated negative thermal expansion in $\text{Bi}_{0.7}\text{Nd}_{0.3}\text{FeO}_3$

4.1 Introduction

This chapter focuses on the relaxor-type behaviour studied with immittance spectroscopy and a detailed study on the structural changes observed in $\text{Bi}_{0.7}\text{Nd}_{0.3}\text{FeO}_3$ (BNFO30). The analysis based on variable temperature powder neutron diffraction (PND) shows BNFO30 adopts the space group $Pn'ma'$ with a G_z -type magnetic unit cell (the same as BLFO50 as described in the previous chapter). Structural distortions are linked to the relative permittivity of the sample with an accompanied change in the magnitude of both octahedral tilts. These distortions correspond to A-site displacements along the a and c -axes. In contrast to $\text{Bi}_{0.5}\text{La}_{0.5}\text{FeO}_3$ (BLFO50), described in chapter 3, both in-phase and anti-phase tilts decrease with decreasing temperature.

As previously introduced in chapter 3, applications and the study of bulk BiFeO_3 are hindered by electrical conductivity due to non-stoichiometry and thermal metastability.¹ The substitution of the volatile Bi^{3+} with rare earths *e.g.* Nd^{3+} ($\text{Bi}_{1-x}\text{Nd}_x\text{FeO}_3$) can improve the electrical properties and thermal stability of the perovskite phase. BLFO50 showed that doping the system affects the octahedra tilts, however, in this case, the effect is more extreme: more than one axis expands on cooling below *circa.* 200 K, which results in negative thermal expansion of the unit cell. This subtle change in behaviour is believed to be due to the smaller ionic radius of Nd^{3+} relative to Bi^{3+} and La^{3+} ; therefore, in this chapter the effects of reducing the A-site average ionic radii will be evaluated.

The $\text{Bi}_{1-x}\text{Nd}_x\text{FeO}_3$ system has been studied in some detail by other authors such as Levin *et al.* who have proposed a phase diagram based on conventional solid-state synthesis.^{2,3} They report the following phase sequence at room temperature: $R3c$ ($0 < x \leq 0.125$) \rightarrow ' $Pbam$ ' ($0.125 < x \leq 0.25$) $\rightarrow Pbnm$ ($x < 0.25$). More specifically, the ' $Pbam$ ' phase has a PbZrO_3 -like antipolar superlattice, with a $\sqrt{2} a_p \times 2\sqrt{2} a_p \times 4 a_p$ unit cell, relative to the aristotype cubic perovskite (a_p). The $Pbnm$ phase has the common GdFeO_3 -like structure, with a $\sqrt{2} a_p \times \sqrt{2} a_p \times 2 a_p$ unit cell.

The NdFeO₃ parent end member ($x = 1$) adopts the same orthorhombic *Pbnm* (62. *Pnma*) structure as BNFO30 and has been studied using neutron and X-ray diffraction.^{4, 5} This has highlighted a number of interesting magnetic interactions within NdFeO₃. The observations of Sosnowska *et al.* reported here have been converted to the *Pnma* setting for comparison with the current work.^{4, 5} There is a C-type antiferromagnetic ordering of Nd³⁺ moments (Figure 4.1) which orders at very low temperatures *circa.* < 1.5 K.⁵ More importantly, the Fe-Fe interactions order creating a cell that conforms to a G₂-type antiferromagnetic cell above 200 K.⁵

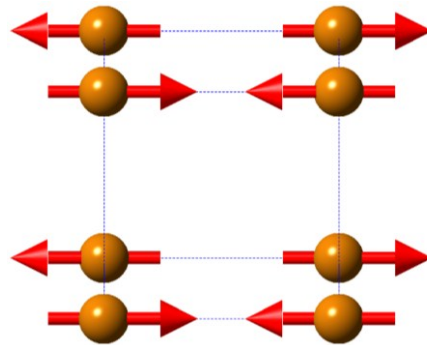


Figure 4.1: C-type magnetic order of the Nd³⁺ moments which occurs *circa.* 1.5 K.

NdFeO₃ has Néel temperature of 690 K.⁶⁻⁸ Below 200 K, there is a coherent rotation of the FeO₆ octahedra and a spin reorientation in the *b-c* plane resulting in an additional component, G_y, to the magnetic cell.⁵ This is due to the increase in the Fe-O2-Fe angle associated with the in-phase tilt and an increase of the axial Fe-O1 bond lengths without changes of the Fe-O1-Fe angles associated with the anti-phase tilt.⁵ This spin reorientation transition has been observed between 100 – 190 K where the Fe³⁺ magnetic moments gradually change direction.⁵ The corresponding rotation of the octahedra may affect the electrical properties, as it will change the freedom of the A-site cations to displace causing a change in polarisability. An A-site displacement has been reported in NdFeO₃, which occurs in the *a-c* plane of the *Pnma* cell (*Pbnm*: *a-b* plane). There is also a negative thermal expansion shown in the *a* lattice parameter over a temperature range 40 - 160 K.^{4, 5}

In this study, PND has been used to highlight similar structural effects within BNFO30 that cause a significant change in the electrical behaviour. In addition, negative thermal expansion of the unit cell has been observed.

4.2 Experimental

The synthesis was carefully performed *via* conventional solid-state methods as outlined in the experimental chapter 2.1. Stoichiometric amounts of Bi_2O_3 and Fe_2O_3 were mixed with Nd_2O_3 , which was dried at 1000 °C prior to weighing. The calcination temperatures for the two-step reaction mentioned within this chapter were 800 °C (5 hrs.) for the 1st calcination step and 1000 °C (5 hrs.) for the 2nd calcination step. Both calcination steps were performed in air.

PND data were collected using the HRPD diffractometer at the ISIS neutron spallation source, Rutherford Appleton Laboratories over an experimental temperature range from 50 - 500 K. Rietveld refinements were carried out using the general structural analysis system (GSAS) and its associated graphical user interface program (EXPGUI).^{9, 10}

4.3 Results - Preliminary structural analysis

Based on this temperature dependent PND study, BNFO30 was found to be primarily the GdFeO_3 -like phase, which has been refined in the alternate *Pnma* setting. A trace amount of Fe_2O_3 secondary phase (*circa.* 1 wt%) was also detected which remains constant in all refinements. Figure 4.2 shows the Rietveld refinement profile of BNFO30 at 300 K with the corresponding unit cell parameters and atom positions shown in Table 4.1.

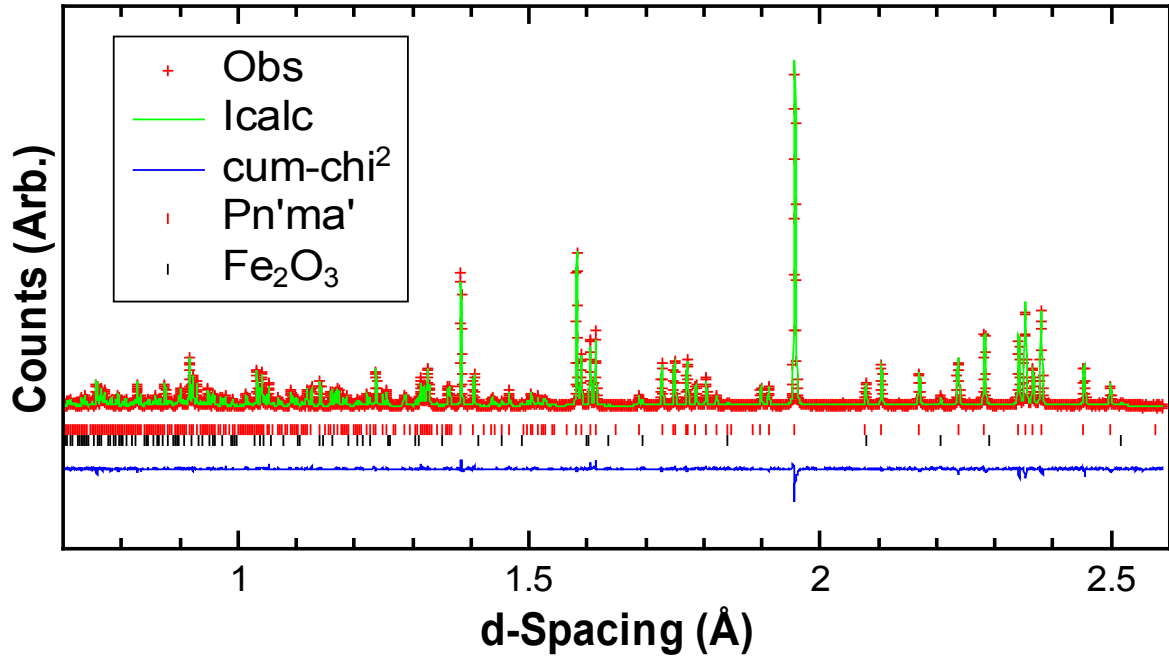


Figure 4.2: Isotropic Rietveld refinement profile of the PND data at 300 K; $\chi^2 = 2.574$, $wR_p = 0.0500$, $R_p = 0.0467$. Tick marks represent Bragg reflections for $Pn'ma'$ (top) and Fe_2O_3 (bottom).

Table 4.1: Atomic coordinates of the $Bi_{0.7}Nd_{0.3}FeO_3$ $Pn'ma'$ phase refined from the 300 K PND data; $a = 5.61889(4)$ Å, $b = 7.81949(5)$ Å, $c = 5.45226(4)$ Å.

Site	X	Y	Z	U_{iso} (Å ²)
Bi/Nd	0.04671(15)	0.25	0.9933(2)	0.0063(2)
Fe	0	0	0.5	-0.00058(16)
O1	0.4750(3)	0.25	0.0883(3)	0.00536(18)
O2	0.20193(18)	0.54305(13)	0.19982(18)	0.00536(18)

The $Pnma$ phase has been refined with a G_z -type antiferromagnetic unit cell, described with Shubnikov symmetry as $Pn'ma'$. This is the equivalent cell to BLFO50 and the parent G_x -type magnetic cell of $NdFeO_3$ refined in the $Pbnm$ setting.^{4, 5} The moment has been refined and fixed along the c -axis, which produces the most stable refinement. The net magnetization based on these refinements, Figure 4.3, shows a significant magnitude at all studied temperatures.

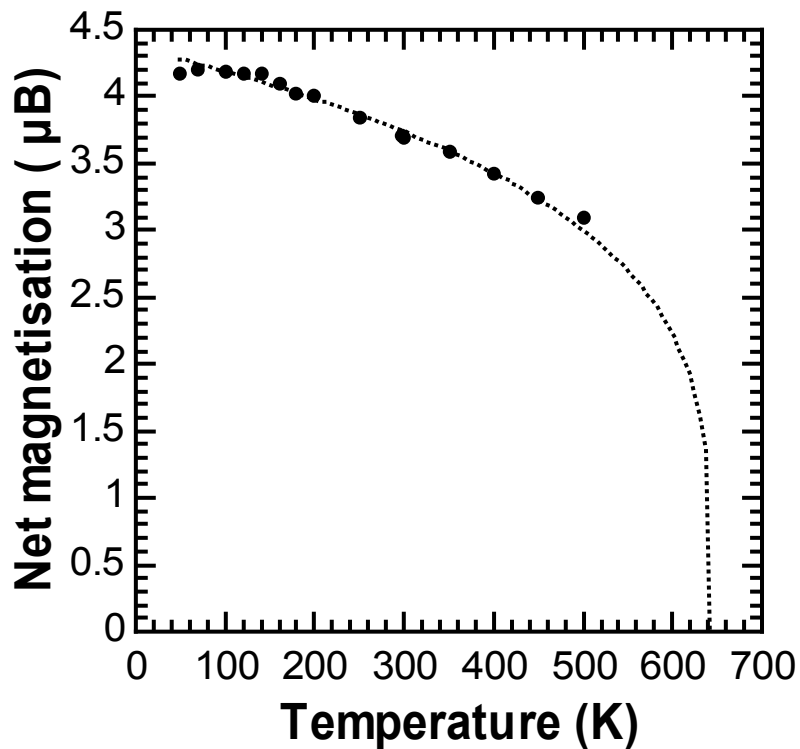


Figure 4.3: Net magnetisation along (c) as a function of temperature in $Bi_{0.7}Nd_{0.3}FeO_3$. Black dotted line represents a fit of the magnetic data to a power law.

The Néel temperature is expected to be slightly lower than that of the parent $NdFeO_3$ (T_N *circa.* 690 K)⁶⁻⁸ due to the relationship with the Fe-O-Fe angles as discussed later. Other PND studies, such as that by Koehler *et al.*¹¹ have suggested a higher Néel temperature, around $T_N \sim 760$ K.

An attempt at fitting the net magnetisation to a power law, Equation 4.1, assuming a mean field approximation, found that the Néel temperature, T_N , should be *circa.* 642 K +/- 84 K with an exponential term, α , of 0.25 +/- 0.06. However, the extrapolation is over a significant range and the error is therefore large.

$$F(T) \propto (T_N - T)^\alpha \quad \text{Equation 4.1}$$

On cooling to 100 K, the quality of the fit degrades for the $Pn'ma'$ model due to changes in the relative peak intensities. Therefore, other magnetic models were tested at low temperature with the moments aligned in their respective directions. The G_z type magnetic cell with the moment fixed along the c -axis remains the best refinement. The goodness-of-fit parameters, χ^2 , wR_p , and R_p for the other magnetic models are shown in Table 4.2.

Table 4.2: Goodness-of-fit parameters for magnetic and non-magnetic refinements of the $Pnma$ cell at 100 K.

Magnetic Symmetry	Space group	χ^2	wR_p	R_p
G_z	$Pn'ma'$	9.552	0.0971	0.0802
G_y	$Pn'm'a$	11.810	0.1080	0.0962
G_x	$Pnma$	11.860	0.1820	0.0947
(non-magnetic)	$Pnma$	13.090	0.1137	0.1047

A number of papers show that orthoferrites can have off-axis magnetic components,^{5, 12} which could be the origin of intensity changes at low temperature. Therefore, an attempt at refining an off-axis magnetic component was made by using soft constraints and allowing components along M_x and M_y . However, this produced unstable models due to refining near zero magnetic moments.

The software ISODISTORT can be used to quickly predict magnetic intensity.¹³ The $Pn'ma'$ setting was used to simulate a magnetic component along the a -axis. It was found to add intensity uniquely on magnetic reflections at $[h,k,l] = [0,1,2]$, $[0,3,0]$, and a structural and magnetic reflection at $[2,1,0]$. A refinement of data collected at 100 K shows that these reflections should occur at 2.58 Å, 2.61 Å, and 2.63 Å d-spacing, respectively. There is no sign of additional magnetic intensity in the 90° bank data and in the backscattering bank no 2.58 Å $[0,1,2]$ reflection is distinguishable. An off-axis component along the a -axis is therefore not present and cannot be the origin of intensity changes at low temperatures. There are no easily distinguished unique reflections for a magnetic component along the b -axis. Other possibilities for intensity changes are reviewed later.

The temperature dependent PND study (50 - 500 K) revealed the evolution of the unit cell parameters shown in Figure 4.4, where there is a similar contraction in the c -axis and expansion in the a -axis on heating over a wide temperature range (50 K to 200 K). Over the same range, there is also negative thermal expansion in the b -axis on heating.

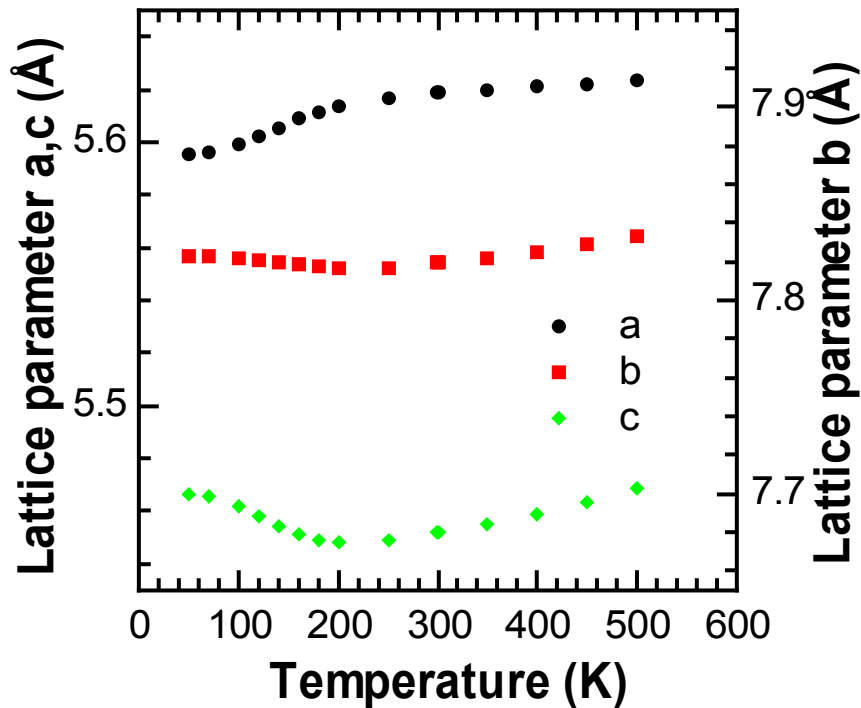


Figure 4.4: Lattice parameters as a function of temperature

This negative thermal expansion in the b - and c -axes results in an overall contraction of the unit cell volume as a function of increasing temperature (Figure 4.5). This is rather unusual; for example in BLFO50, the magnetostriction resulted in an invar effect where the volume becomes invariant at low temperature (chapter 3).

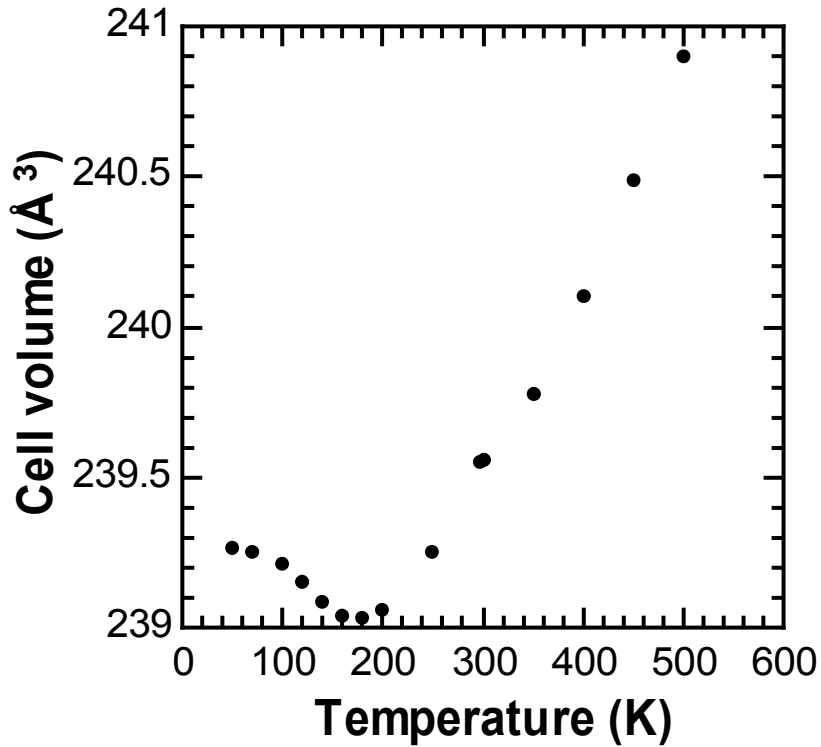


Figure 4.5: BNFO30 unit cell volume as a function of temperature.

The changes in the unit cell volume can be evaluated in terms of thermal expansion coefficients using Equation 4.2, where V_0 is the volume, T is temperature, and α_v is the expansion coefficient.

$$\alpha_v(T) = \frac{1}{V_0} \cdot \frac{\delta V}{\delta T} \quad \text{Equation 4.2}$$

The differing gradient and intercepts were determined between all points from 50 to 500 K based on a linear fit between adjacent temperature readings. The average gradient and intercept over the ranges are for the positive and negative thermal expansion regions are as follows:

$$V = 4.20 \times 10^{-3} \times T + 236.8 \quad (200-500 \text{ K})$$

$$V = -1.82 \times 10^{-3} \times T + 239.4 \quad (50 - 180 \text{ K})$$

Based on these fits the calculated average thermal expansion coefficient is $2.18 \times 10^{-5} \text{ K}^{-1}$ for the expansion of the unit cell above 200 K and varies between 3.48×10^{-5} and $5.18 \times 10^{-6} \text{ K}^{-1}$. The average (negative) thermal expansion coefficient is $-7.59 \times 10^{-6} \text{ K}^{-1}$ at lower temperatures (50 K- 180 K) and ranges from $-1.32 \times 10^{-5} \text{ K}^{-1}$ to $-2.05 \times 10^{-6} \text{ K}^{-1}$. This change in expansion is clearly significant and can be explained with changes in the physical properties of the material *i.e.*, magnetism and bonding as outlined in the following sections.

4.4 Strain and the impact on diffraction

As previously stated the intensity of the reflections at low temperature cannot be fully accounted for with a simple isotropic refinement of the nuclear and magnetic structure. The quality of the isotropic refinements below 200 K deteriorates. The assessment of different magnetic models suggests that the intensity mismatch is unlikely to be associated with a spin reorientation or off-axis magnetisation. There are no additional reflections at low temperature, which would be indicative of a change of symmetry. This is shown in the Rietveld refinement using isotropic peak profiles, Figure 4.6, where the intensities are poorly fitted due to the peak shapes.

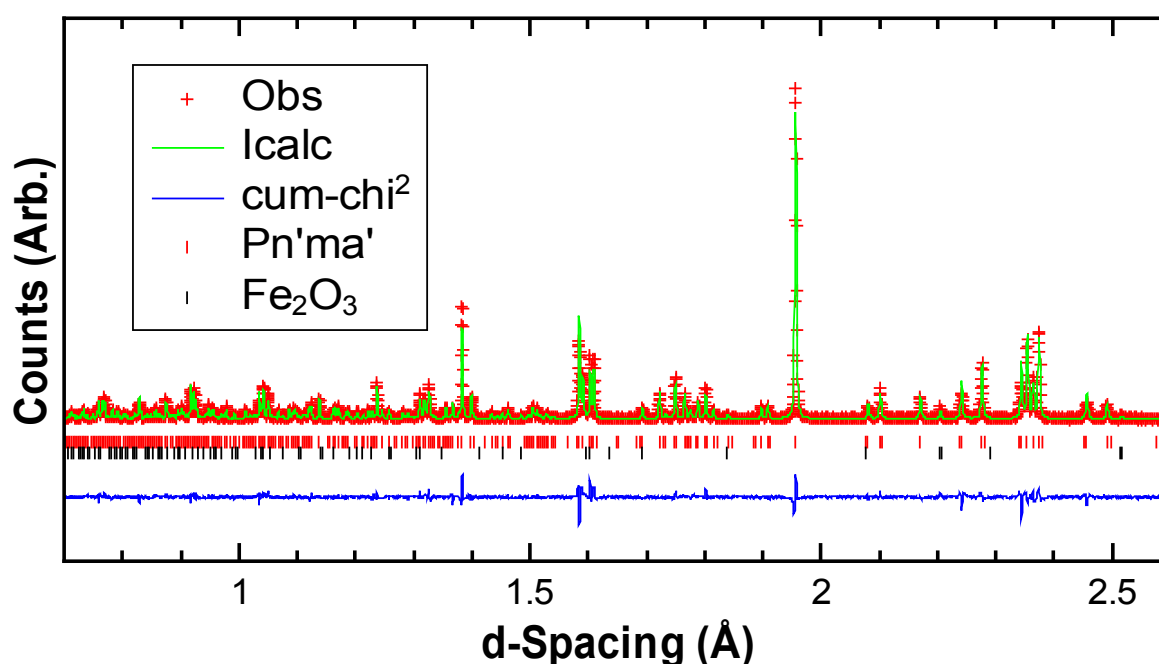


Figure 4.6 Isotropic refinement of the 50 K data showing a poor quality of fit due to the modelling of peak shapes. $X^2 = 8.647$, $wRp = 0.0925$, $Rp = 0.0763$.

Anisotropic peak broadening can occur in powder diffraction patterns, for instance due to strain which broadens reflections as a function of h, k, l . GSAS models this broadening with a Lorentzian function (profile function 3) which is designed to model macroscopic strain. The profile adds six additional empirical terms, labelled as L_{11} (γ_{11}), L_{22} (γ_{22}), L_{33} (γ_{33}), L_{12} (γ_{12}), L_{12} (γ_{12}), and L_{23} (γ_{23}). The terms are conventionally labelled with the Greek letter gamma, γ , and broaden specific h, k, l reflections as shown in Equation 4.3.

$$\gamma_L = \gamma_{11}h^2 + \gamma_{22}k^2 + \gamma_{33}l^2 + \gamma_{12}hk + \gamma_{13}hl + \gamma_{23}kl \quad \text{Equation 4.3}$$

The systematic evaluation of the terms showed that the L_{11} and L_{33} have the most significant impact on the quality of the fit by broadening (h,l)-dominated reflections. The refinement profile, Figure 4.7, with these terms demonstrates a significant improvement to the quality of the fit.

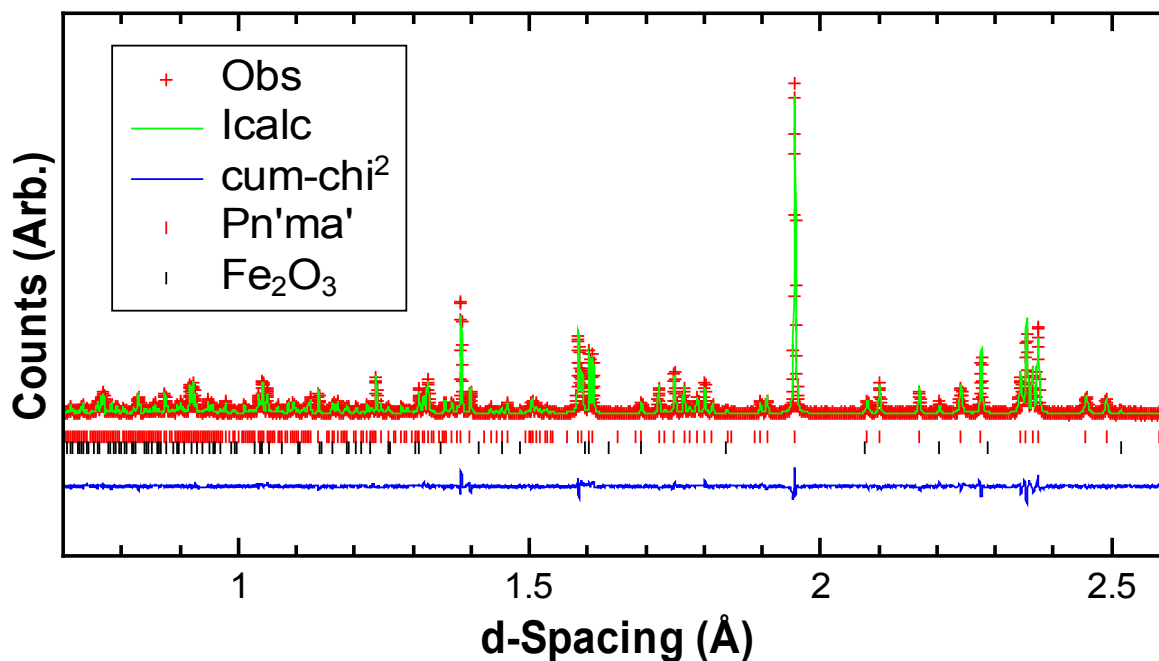


Figure 4.7: Refinement profile of the 50 K data with anisotropic L_{33} and L_{11} peak broadening terms; $\chi^2 = 4.898$, $wR_p = 0.0696$ $R_p = 0.0624$.

For comparison, Table 4.3 compares agreement factors of models with and without the anisotropic peak broadening at 50 K.

Table 4.3: Goodness-of-fit parameters for refinements with and without L_{xx} strain terms.

Model	Spacegroup	χ^2	wR_p	R_p
No strain terms	$Pn'ma'$	8.647	0.0925	0.0763
Profile 3 L_{33}	$Pn'ma'$	5.19	0.0717	0.0626
Profile 3 L_{33} L_{11}	$Pn'ma'$	4.898	0.0696	0.0624
Profile 3 L_{xx} (6 terms)	$Pn'ma'$	3.522	0.059	0.0536

4.5 Electrical properties

The electrical theory that has been used within this chapter is outlined in the experimental theory section on immittance spectroscopy (chapter 2.7). The electrical response of the BNFO30 sample shows it has at least two electroactive regions, which are clearly visible in the electrical modulus (Figure 4.8) and impedance (Figure 4.9).

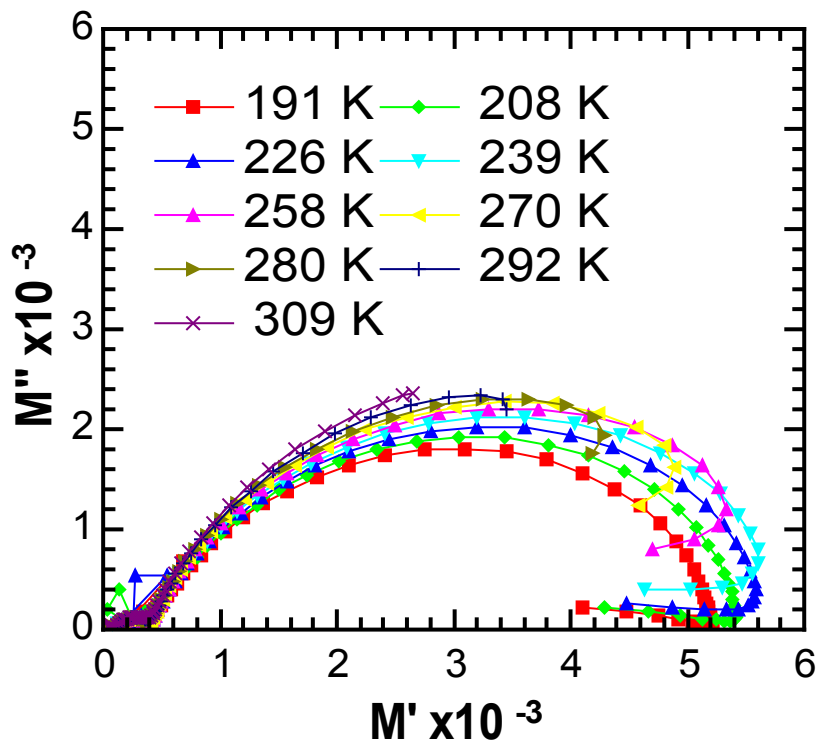


Figure 4.8 Complex modulus, M^* , as a function of temperature showing two electroactive components.

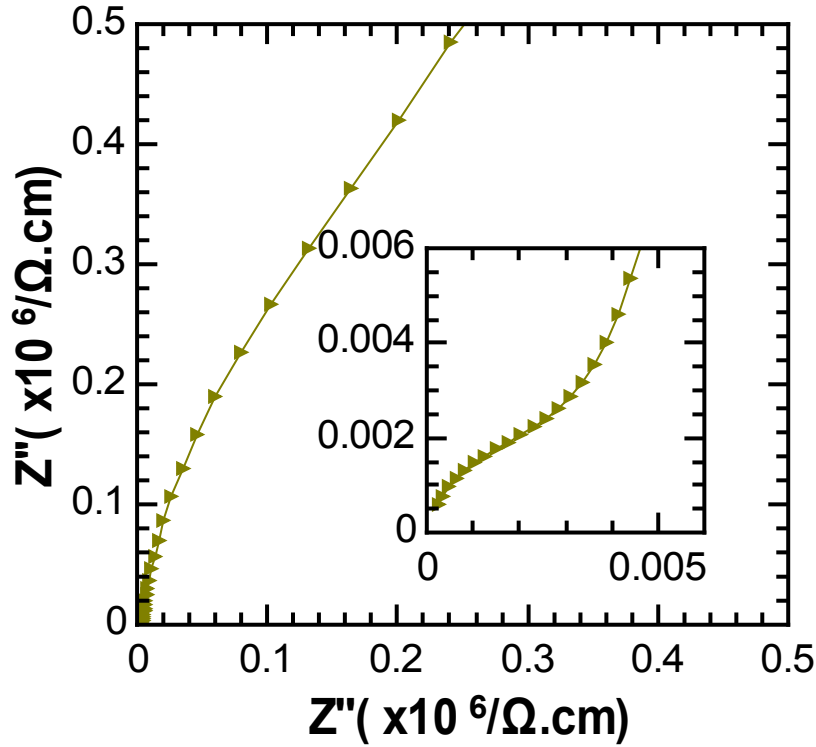


Figure 4.9: Complex impedance, Z^* , plane plot at 280 K showing the grain boundary and conducting bulk response (in the insert region Z' 0-0.006).

The permittivity of the electroactive responses was determined from the diameter of the semi-circular arc in the complex electric modulus (Figure 4.8) which scales directly as $1/\epsilon_r$. From this, it was possible to determine the capacitive response of the components. At 280 K, for example, the capacitance (C) of the component that dominates the complex modulus is 13.3 pFcm^{-1} . The response has therefore been associated with the bulk based on typical bulk capacitive responses given by Irvine *et al.*¹⁴

On cooling the sample, isothermal analysis has shown that the magnitude of the bulk capacitive response increases before leaving the measurable frequency window *circa*. 174 K. Assuming Debye like behaviour, the peak maximum, M''_{max} , of an RC element is related to the capacitance and dielectric permittivity (ϵ_r) by:

$$M''_{max} = \frac{\epsilon_0}{2C} = \frac{1}{2\epsilon_r} \quad \text{Equation 4.4}$$

The Debye-like M'' peak decreases in magnitude on cooling and moves across the frequency domain of the M'' spectra (Figure 4.10). This represents an increase in the capacitance of the bulk.

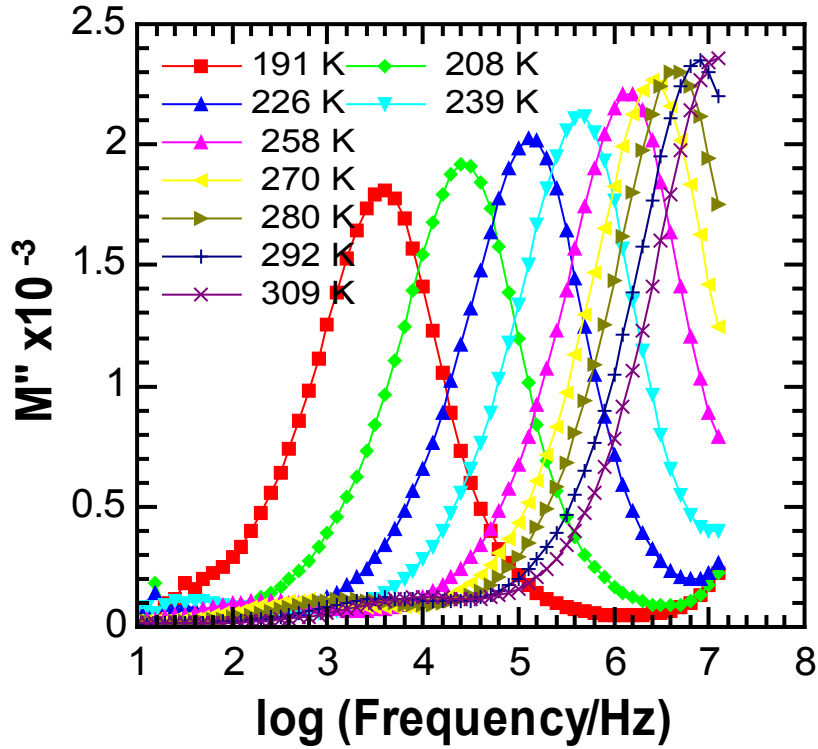


Figure 4.10: M'' spectra show the electroactive response of the bulk dominating the electrical response.

The displacement of the peak to lower frequencies indicates, as expected, the resistance of the sample increases as shown by:

$$\tau = RC = \frac{1}{2\pi f_{max}} \quad \text{Equation 4.5}$$

Fixed frequency, total capacitance (C_p) and loss ($\tan \delta$) measurements, performed on the BNFO30 sample allowed for the analysis of the capacitive behaviour at temperatures below those where individual relaxations could be observed. Assuming an equivalent circuit of two parallel RC elements in series (representing the bulk and grain boundary regions) as outlined in the experimental section on the brickwork model (chapter 2.7.3), the parallel capacitance (C_p) as a function of frequency results in a high frequency plateau.¹⁵ This plateau contains contributions from both bulk (C_b) and grain boundary (C_{gb}) capacitances according to:

$$C_p = (C_{gb}^{-1} + C_b^{-1})^{-1} \quad \text{Equation 4.6}$$

The magnitudes of the capacitive responses in the BNFO30 pellet are such that $C_{gb} \gg C_b$. This means that the overall contribution of the grain boundary to the total capacitance at high frequency is small and C_p is effectively that of the bulk response. Bulk capacitance data

extracted from M^* at higher temperatures can be used to validate this assumption ($C_{gb} \gg C_b$) from which the relative permittivity of the bulk were calculated based on:

$$C_p = \epsilon_r \epsilon_0 \frac{A}{d} \quad \text{Equation 4.7}$$

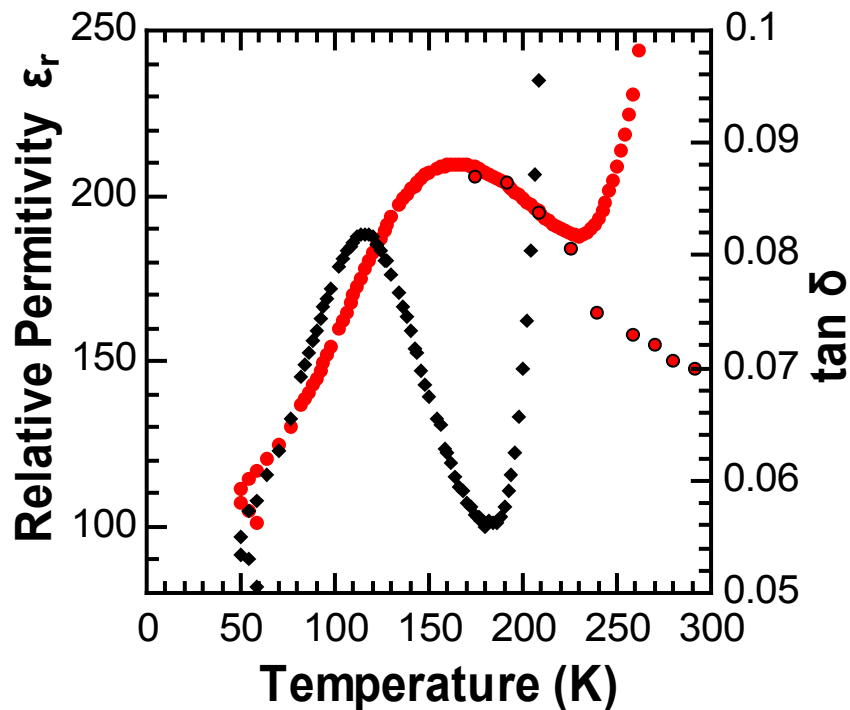


Figure 4.11: Relative permittivity (circles) and loss (diamonds) is shown as a function of temperature (1 MHz). Bulk permittivity values determined from modulus data obtained from isothermal measurements are included (circles with black outline).

For simplicity, the total effective permittivity at 1 MHz has been plotted as a function of temperature and there is good agreement between the effective permittivity based on the total capacitance and bulk values as determined from M^* plots. The relative permittivity ranges from *circa.* 110 – 210 and peaking around *circa.* 160 K. At higher temperature, there is a dramatic upturn in the 1 MHz data due to an increasing contribution from the grain boundary/electrode response.

However, plotting the relative permittivity and loss at multiple frequencies shows a frequency dependence, which is characteristic of relaxor-type behaviour (as shown by the frequency dispersion and displacement in the peak maxima, Figure 4.12). The frequency dependence in the peak maxima means that the peak position varies by *circa.* 20 °C between 1 kHz and 1 MHz.

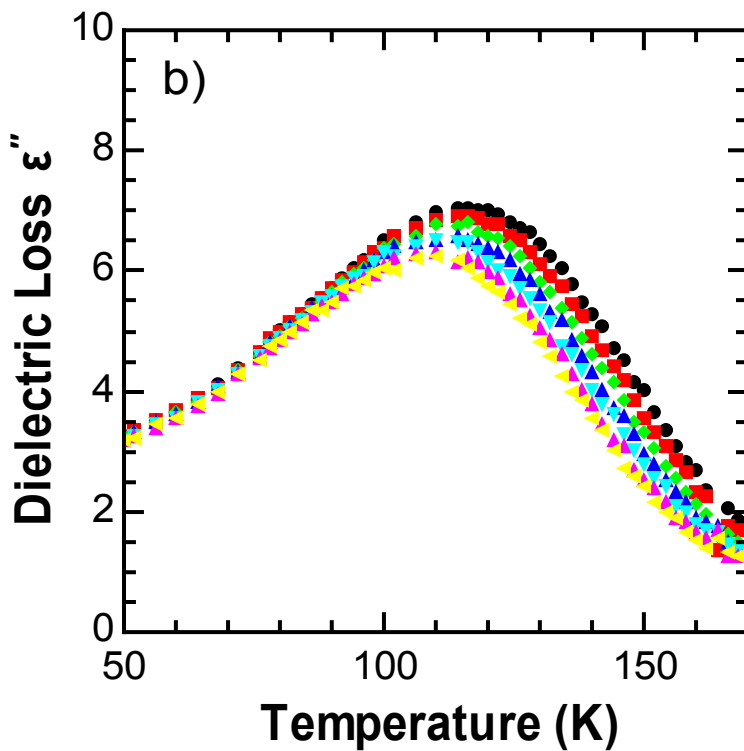
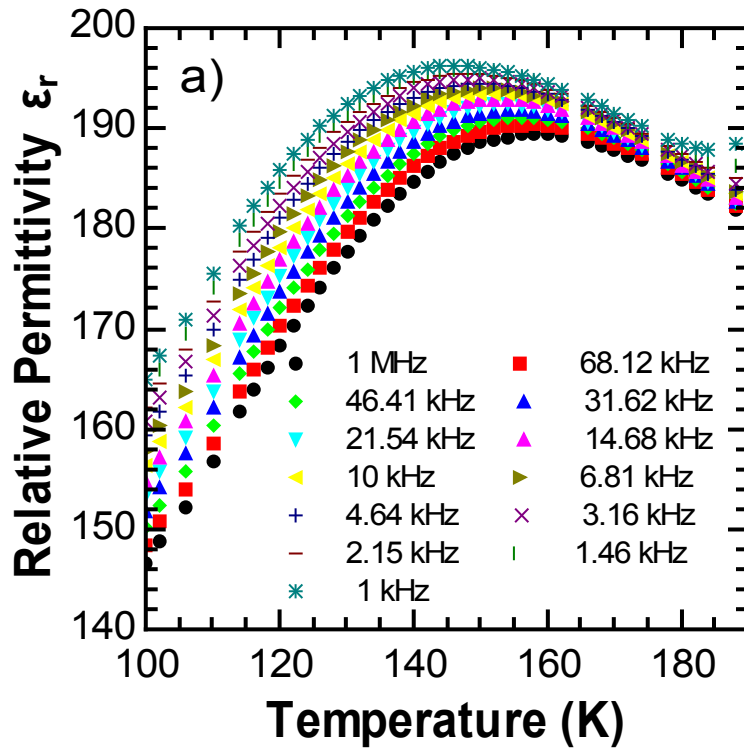


Figure 4.12: Plot of the relative permittivity (a) and loss (b) as a function of temperature showing a frequency dispersion at low temperature. Symbols in part (a) and (b) are the same

Relaxor-type behaviour can occur due to inhomogeneity on a nanometre scale. In BNFO30, this will probably be due to A-site disorder with regional clusters of neodymium and bismuth. It has been suggested clusters of nano-regions may be interacting at low temperature,^{16, 17} creating a spectrum of relaxation times, which correspond to random local relaxation processes.

The frequency dispersion in the relative permittivity can be analysed with a Vogel-Fulcher (VF) expression, Equation 4.8:¹⁸

$$f = f_0 e^{-E_a/k(T_m - T_f)} \quad \text{Equation 4.8}$$

where f corresponds to the frequency of applied field, f_0 is the limiting response frequency of the dipoles, E_a is the activation energy associated with the local polarisation process, k is the Boltzmann constant, T_m is the temperature at which the relative permittivity is at its maximum for a given frequency (f) and T_f is the static (dipole) freezing temperature.

A frequency sweep with an excitation voltage of 500 mV was performed measuring the total capacitance and loss as a function of temperature. 31 frequencies were recorded from 100 Hz to 10 MHz of which 17 frequencies (f) were used in the VF analysis between 2.154 kHz and 1 MHz; data beyond these limits above and below these thresholds were discarded due to interference from the measuring cables and noise, respectively. Limiting the frequency range of the fit also avoided significant contributions from the grain boundary/electrode response in the higher temperature data.

The peak maximum in the relative permittivity and the corresponding temperature, T_m , were determined from a 2000 point spline fit. Based on Equation 4.8, fitting a function to $\ln f$ vs. T_m data (Figure 4.13) allows the freezing temperature (T_f) to be determined.

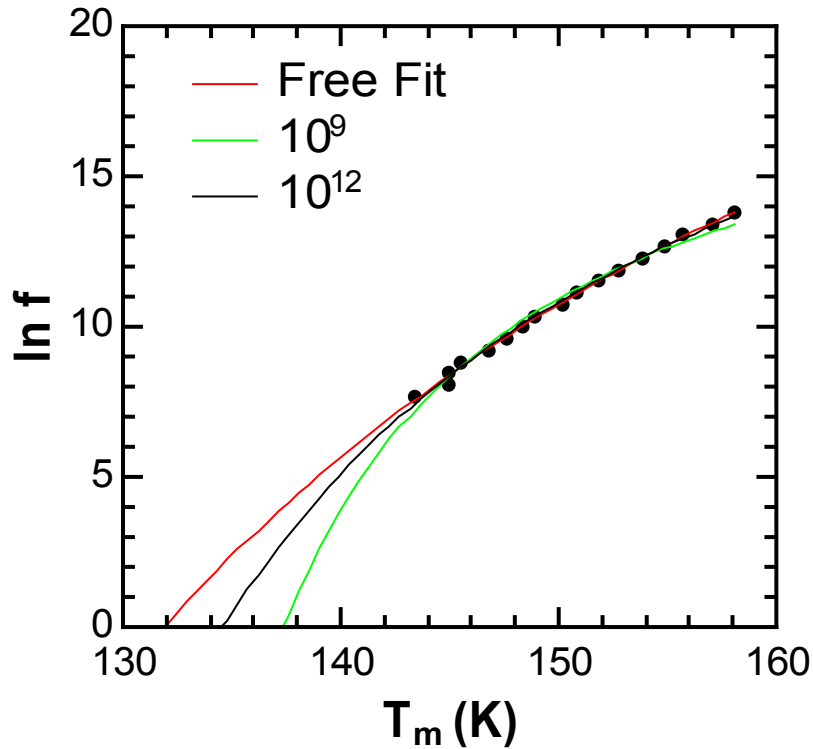


Figure 4.13: $\ln f$ vs. T_m showing an unrealistic free fit (red) and fits where limits for the dipole response frequency f_0 (green and black) have been applied.

An unrestricted (free) fit of this function results in an unrealistic fundamental response frequency of the dipoles, $f_0 = 1.057 \times 10^{17}$ Hz, and a dipole freezing temperature, T_f , of 83 K. Typically dipole response frequencies range between $10^9 - 10^{12}$ Hz.¹⁸ Using these as limits for f_0 results in the following freezing temperature values - Table 4.4.

Table 4.4: The freezing temperatures and associated errors for are shown for fixed values of f_0 .

f_0 (Hz)	$\ln f_0$	T_f (K)	E_a (eV)	χ^2	R^2
10^9	20.7	126.11 +/- 0.74	0.0201 +/-0.007	5.88×10^{-2}	0.985
10^{12}	27.6	110.68 +/- 0.68	0.0569 +/-0.001	1.76×10^{-2}	0.996

As pointed out by Rotaru *et al.*, and demonstrated by the need to fix f_0 to a realistic response frequencies, VF analysis can lead to unreliable and unrealistic physical parameters due to fitting the curvature of T_m over a narrow frequency range and the subsequent extrapolation to determine T_f .¹⁸

Consequently, methods that are more robust can be used to give frequency independent parameters such as the analysis of the dielectric loss, ϵ'' , with Jonscher's universal dielectric response (UDR) model. UDR describes the frequency dependent response of the ϵ'' by:¹⁹

$$\epsilon'' = \frac{1}{(f/f_p)^{-m} + (f/f_p)^{1-n}} \quad \text{Equation 4.9}$$

where f is the ac applied frequency, f_p is the frequency at which the ϵ'' reaches a maxima and exponent terms describe the gradient of the response below (m) and above ($n-1$) the peak frequency, respectively (Figure 4.14). The two exponents m and n allow for the fitting of asymmetric peaks found in relaxors and has allowed values between $0 \leq m, n \leq 1$. For a perfect Debye response the gradient before and after the peak maxima in a $\log \epsilon''$ vs. $\log f$ (Hz) plot should be +1 and -1 respectively *i.e.*, $m = 1$, and $n = 0$.

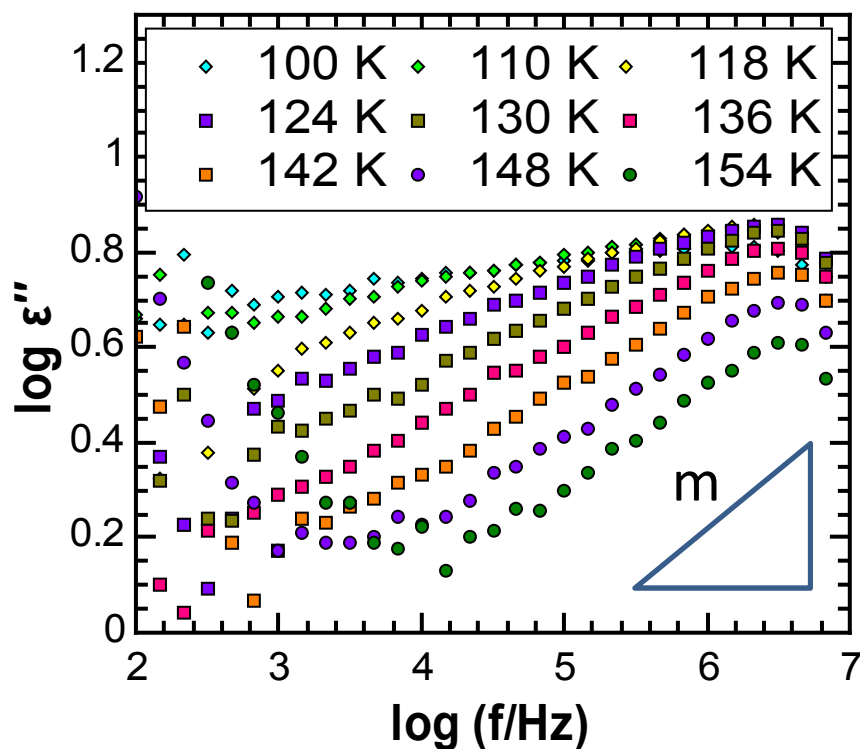


Figure 4.14: Dielectric loss spectra ($\log \epsilon''$ vs. $\log f$) at selected temperatures.

As expected with relaxor type behaviour, the ϵ'' peak of the bulk response in the BNFO30 sample shows asymmetry, as seen in the plot of $\log \epsilon''$ vs. $\log f$ (Hz) (Figure 4.14). There is also a minor secondary component, which enters the low frequency window at high temperature, which is associated with the more resistive grain boundary. Critically, we observe that the gradient of the electroactive response, m , shown in Figure 4.14 decreases on cooling.

This is due to the sample approaching a critical freezing temperature, T_f , below which the dipoles will have a frequency independent response, which means the gradient, m , should tend towards zero when approaching the freezing temperature.

The minor secondary component which is present in the high temperature data means that the gradient m shown in Figure 4.15 as a function of temperature, had to be carefully determined for a series of temperatures. The deviation at low temperature is associated with a gradual change in the quality of the fit in m as the gradient is determined close to the peak maxima. Therefore, an extrapolation over the linear part of the curve from 110 – 136 K was performed avoiding potential additional contributions at temperature extremes. On cooling, the gradient, m , of the bulk ϵ'' response tends toward zero as the freezing temperature is approached, Figure 4.14; therefore extrapolating to $m = 0$ results in an estimated freezing temperature, T_f , of 96 K +/- 3 K. This is similar to that of the VF analysis where the analysis showed that the freezing temperature lies within a range 110 - 126 K.

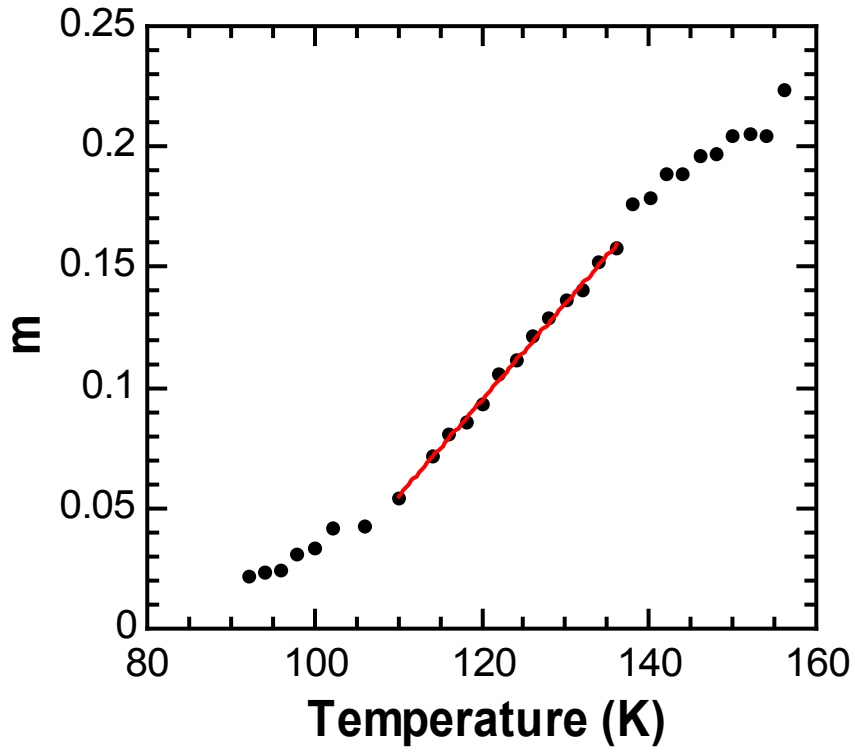


Figure 4.15: Gradient, m , of the response shown in the $\log \varepsilon''$ vs. $\log f$ plot as a function of temperature

4.6 Activation energy of the bulk conduction process.

As in chapter 3, bulk conductivities, $\sigma_b (= R_b^{-1})$ were estimated over a range of temperature using capacitances obtained from M^* and M''_{max} frequency using the relationship $RC = 1/2\pi f_{max}$. The conductivity determined from M^* data show the expected temperature dependence described by the Arrhenius expression:

$$\sigma_b = \sigma_0 e^{-\frac{E_a}{kT}} \quad \text{Equation 4.10}$$

The bulk activation energy (E_a) was determined to be ~ 0.35 eV which is consisted with other experimental studies²⁰ and is characteristic of electronic conduction dominated by polaron hopping.²¹

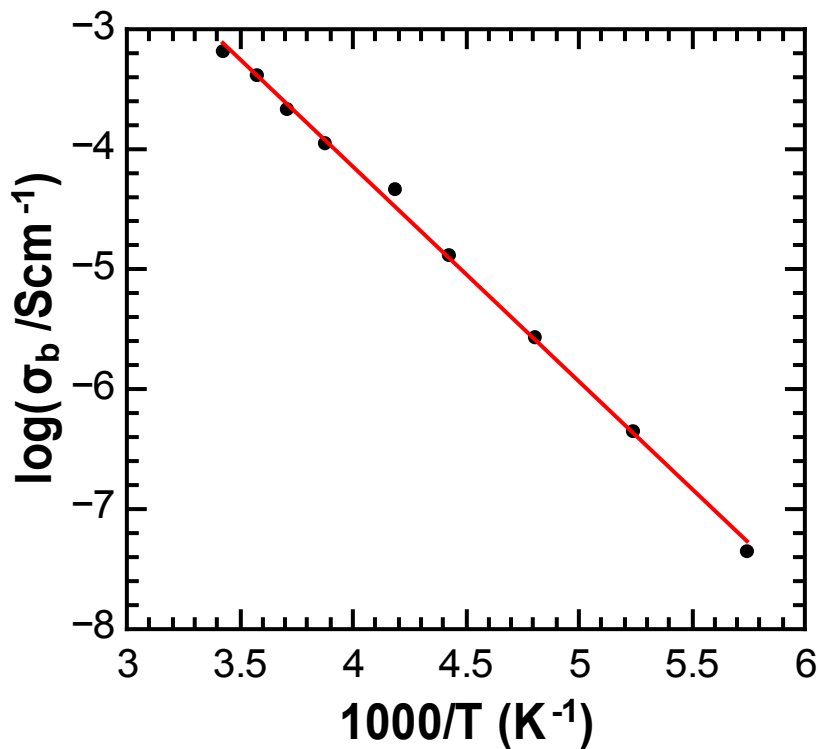


Figure 4.16: Arrhenius plot of bulk conductivities determined from M^* data; $E_a = 0.35 \pm 0.006$ eV ($R^2 = 0.998$).

4.7 Correlation between structural behaviour and the dielectric response

The presence of nano-domains is a possible explanation for the relaxor type behaviour observed in the electrical response. However, it does not explain the origins of changes in the magnitude of the relative permittivity. Changes in relative permittivity of the bulk response are associated with structural changes and long-range order. Therefore, the following section discusses correlations between structural changes determined from the Rietveld refinement of PND data collected during a temperature dependent study and the dielectric response. The analysis uses a combination of conventional 'bond length / bond angle' analysis and using the online structural analysis tool ISODISTORT.¹³

Initial conventional Rietveld refinements showed that the Fe-O bond lengths contract on cooling as expected (Figure 4.17). However, the contraction is not completely linear over the studied temperature range. The rate of contraction in the axial Fe-O1 bond, shown in Figure 4.17, deviates below *circa*. 180 K; this is close to the maximum in the relative permittivity measured at 1 MHz, Figure 4.11. In addition, the longest Fe-O bond length (Fe-O2) shows compression just outside of the level of significance and at a temperature coincident with the 1 MHz peak in the loss ($\tan \delta$), Figure 4.11.

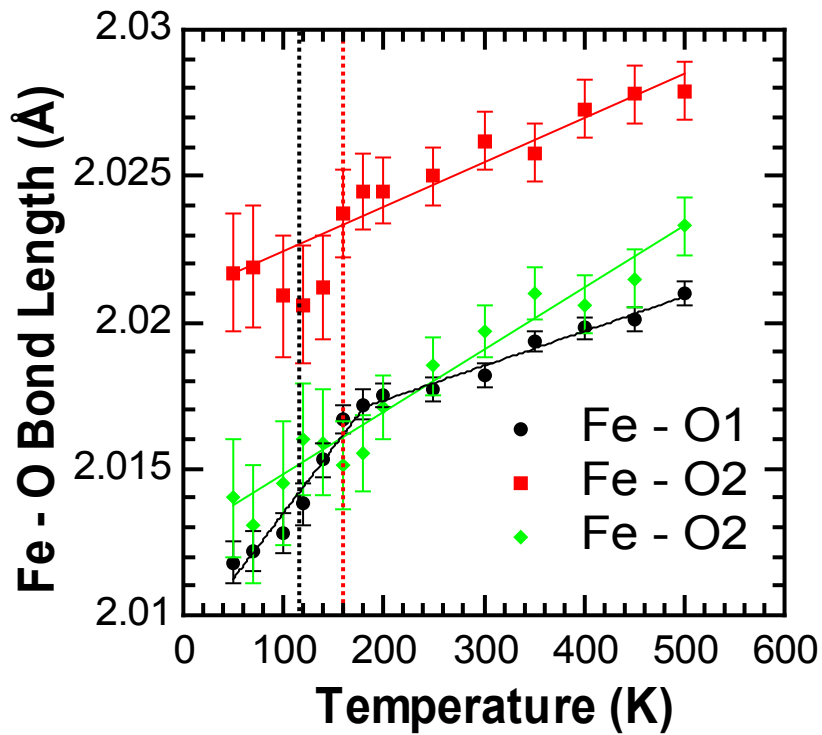


Figure 4.17 Fe-O bond lengths as a function of temperature, showing a change in the Fe-O bond lengths around 160 K (which is in-line with the 1 MHz peak in the relative permittivity shown with the red dotted line. The distortion in the Fe-O2 bond length is in-line with the 1 MHz peak in $\tan \delta$ shown with the black dotted line).

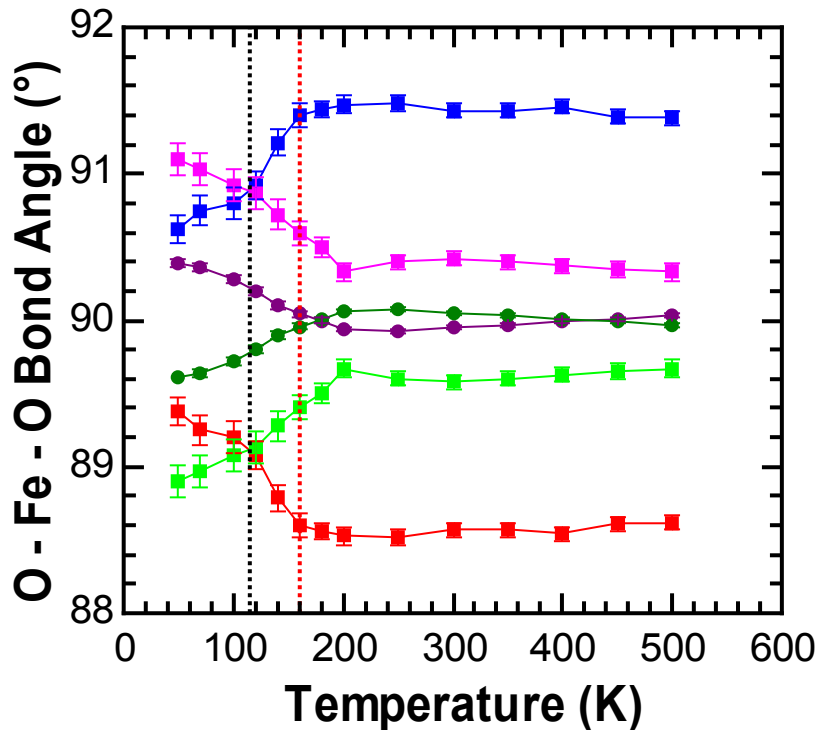


Figure 4.18: Equatorial O1-Fe-O2 (■) and the equatorial-to-equatorial O2-Fe-O2 (●) bond angles are shown as a function of temperature (black dotted line: $\tan \delta$ peak max red dotted line: ϵ' peak max at 1 MHz)

These changes in the Fe-O bond lengths also have corresponding changes with the O-Fe-O intra-octahedral bond angles. On cooling from *circa.* 200 K, 4 of the pairs of O-Fe-O angles deviate away from 90° and the remaining 2 pairs of *circa.* 90° angles between the axial and equatorial plane tend towards 90°. The 4 paired angles are linked to the R_5^+ [O] distortion mode in which it could be viewed that the axial oxygens undergo a slightly different displacement than that of the equatorial plane with respect to the R_4^+ tilt mode and thus the octahedron distorts.

The evaluation of the inter-octahedral Fe-O-Fe angles showed both the Fe-O1-Fe and Fe-O2-Fe angles increase upon cooling below 200 K (Figure 4.19). The Fe-O-Fe angles increase at different rates, resulting in the inter-octahedral angles becoming most equivalent around 180 K.

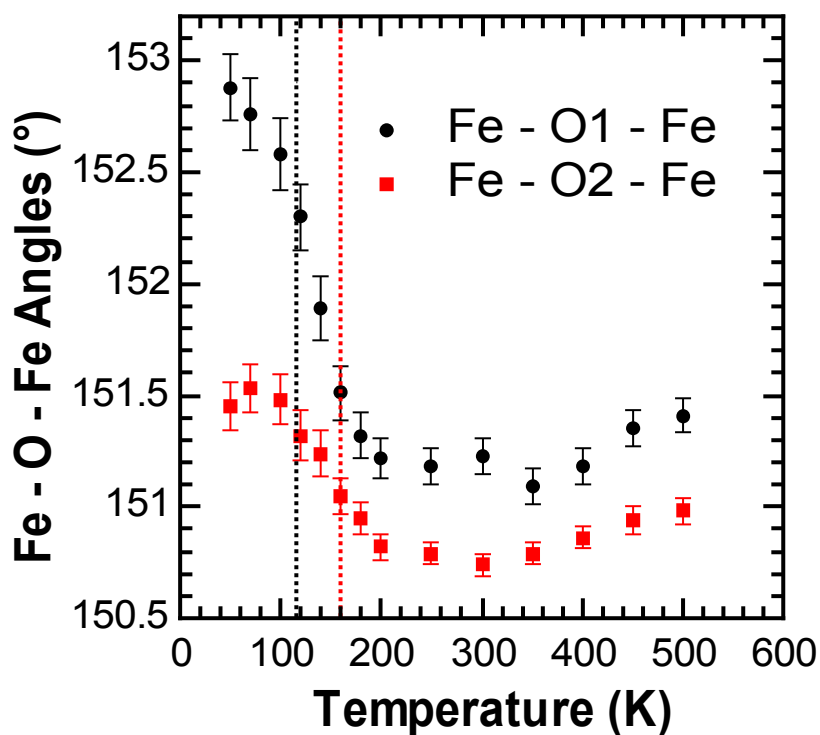


Figure 4.19: Fe-O-Fe angles as a function of temperature, which increases, on cooling. (black dotted line: $\tan \delta$ peak max red dotted line: ϵ' peak max)

The Fe-O-Fe bond angles are comprised of contributions from both the tilt system and distortion modes of the octahedra. In this case, a significant contribution affecting the system comes from the in-phase tilt around the b -axis and anti-phase tilt along b .

Upon cooling below 200 K, the Fe-O1-Fe angle (Figure 4.19) tends towards 180°. This is due to a decreasing octahedral tilt, which means the b -axis will expand on cooling (Figure 4.4). This expansion is offset slightly by the change in the axial Fe-O1 bond length (Figure 4.17). To demonstrate the relation between the (anti-phase) octahedral tilt and the b -axis, a graphical representation of the anti-phase tilt is shown in Figure 4.20. The Fe-O bonds are depicted in order to highlight the Fe-O-Fe angles. If the octahedra are considered to be rigid *i.e.*, constant Fe-O bond lengths, upon cooling, the increasing Fe-O-Fe angle (shown in green) would result in the pseudo cubic unit cell length b (yellow) and b -axis expanding. The expansion along b is due to the decreasing tilt having a larger effect than the expected contraction in the Fe-O1 bond length (Figure 4.17) and therefore the unit cell expands. The lengths a and c should be uniformly affected by the anti-phase tilt and expand.

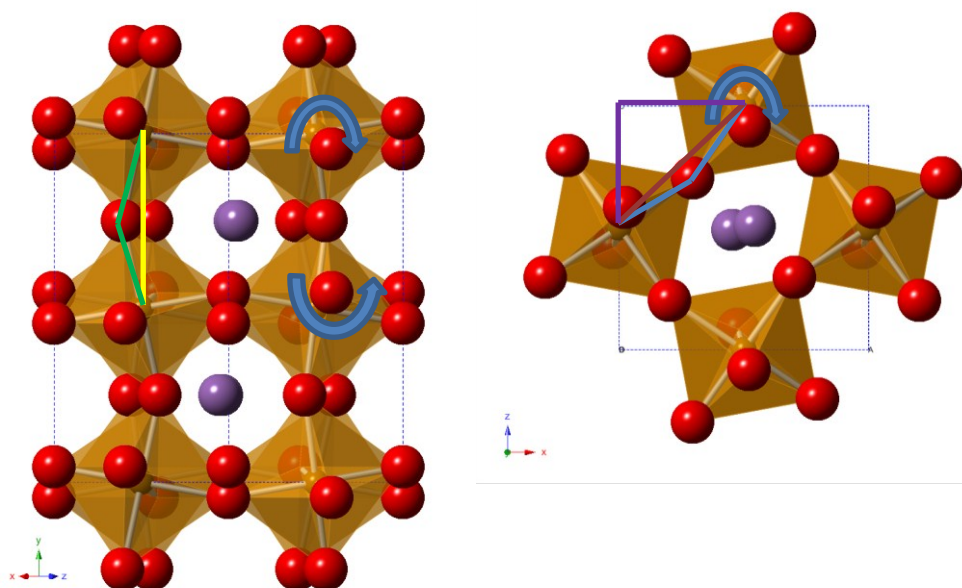


Figure 4.20: Anti-phase, R, rotation in the [101] plane (left) and the In-phase, M, rotation about the b -axis, (right)

The Fe-O2-Fe angle increases due to the in-phase tilt, which has a similar effect on the unit cell as the anti-phase tilt. The lattice affected by a decreasing in-phase tilt mode will expand uniformly in the ac plane. The Fe-O2-Fe angle has been highlighted in light blue in Figure 4.20. On cooling below 200 K, the Fe-O2-Fe angle increases which means the pseudo cubic cell length (shown in brown) expands and the cell lengths a and c should uniformly expand.

This means the contraction in the a -axis (Figure 4.4) cannot be explained by the changing magnitude of the tilt system.

In order to explain the ‘anomalous’ contraction in the a -axis as well as other distortions, ISODISTORT can be used to interpret quantitatively changes in the structure within BNFO30. ISODISTORT does this in terms of distortion modes rather than changes in the observed angles and bond length. This allows the A-site displacements to be simply evaluated, which are linked to the contraction in the a -axis. For instance, as explained previously, the anti-phase tilt must be decreasing on cooling to explain the change in the b -axis.

ISODISTORT represents the anti-phase and in-phase tilts with the R_4^+ and M_3^+ modes, respectively. The magnitude of the tilt modes decrease on cooling below 200 K corresponding to the increases in Fe-O-Fe angles in Figure 4.19. Above 200 K, the tilt modes are almost invariant, ‘plateauing’ prior to the ‘expected’ decrease at higher temperatures. Typically, systems will tend towards higher (un-tilted) symmetry at high temperature.

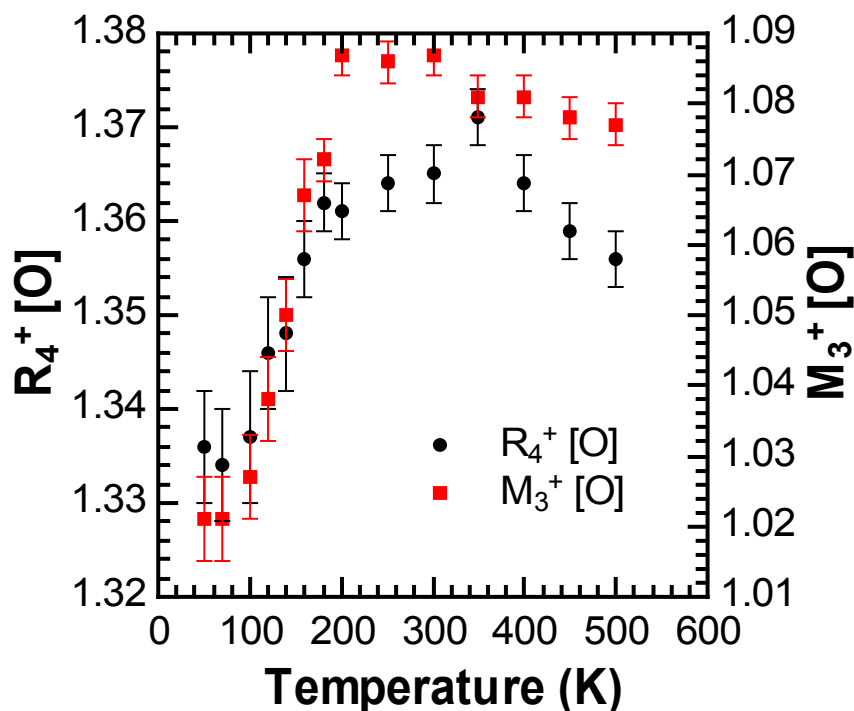


Figure 4.21: M_3^+ mode showing the in-phase rotation about b -axis and R_4^+ mode showing the anti-phase tilt.

A-site displacements can influence the a and c lattice parameters. ISODISTORT represents these with the R_5^+ [A-site] and X_5^+ [A-site] mode representing a displacement along c and a respectively. The R_5^+ [A-site] and X_5^+ [A-site] track with the orthorhombic strain (D_o) shown in Figure 4.22. The orthorhombic distortion parameter, D_o , represents the strain in the structure and is defined in Equation 4.11 where a and c are the unit cell lengths:

$$D_o = \frac{|a - c|}{2(a + c)} \quad \text{Equation 4.11}$$

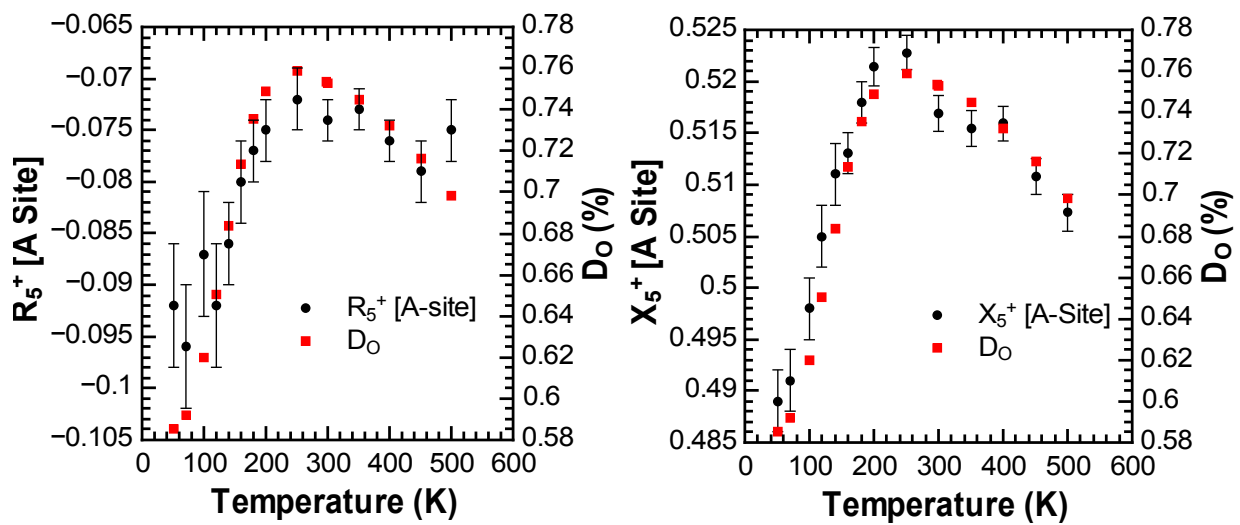


Figure 4.22: X_5^+ and R_5^+ [A-site] modes representing a displacement along a and c respectively. The distortion modes correlate with the degree of the orthorhombic distortion. Over the temperature range 50 – 200 K the change in the magnitude of the X_5^+ [A-site], the displacement along a , is larger than that of the R_5^+ [A-site] (Table 4.5). However, the X_5^+ displacement decreases with decreasing temperature, which means the unit cell is expected to contract along a as is observed in the temperature dependence of the lattice parameters, Figure 4.4. The relative contributions of the various modes can be considered by comparing their relative magnitudes of change in magnitude over this temperature range, δ , where:

$$\delta = |mode_{200K}| - |mode_{50K}| \quad \text{Equation 4.12}$$

In addition to the magnitude of distortion, the sign of the parameter δ denotes increasing (positive δ) and decreasing (negative δ) distortion from the cubic aristotype. From the δ values presented in Table 4.5 it is clear that the R_5^+ [A-site] displacement along c is not only the largest, but it is the only mode to tend away from the ideal cubic aristotype on cooling

(50 – 200 K) – *i.e.*, δ is negative. Note that δ for the R_5^+ [O] mode is also negative, but this mode is also unique in that it changes sign between 200 and 50 K (Figure 4.23). This corresponds to the scissoring distortion where the axial (O1) oxygens change from being under-rotated (negative R_5^+ [O]) relative to the equatorial Fe-O2 plane at 200 K to over-rotated (positive R_5^+ [O]) at 50 K. This change is easily explained by the onset of increasing A-site displacements in the ac -plane (especially in c – the R_5^+ [A-site] mode) which “push out” the axial (O1) oxygens.

Table 4.5: The seven distortion modes, based on the PND refinements at 50 and 200 K.

Temperature (K)	R_4^+ [O]	R_5^+ [A-site]	R_5^+ [O]	X_5^+ [A-site]	X_5^+ [O]	M_2^+ [O]	M_3^+ [O]
200	1.361	-0.075	-0.023	0.521	0.274	0.022	1.087
50	1.336	-0.092	0.035	0.489	0.250	0.012	1.021
Δ	0.025	-0.017	-0.058	0.0324	0.024	0.010	0.066

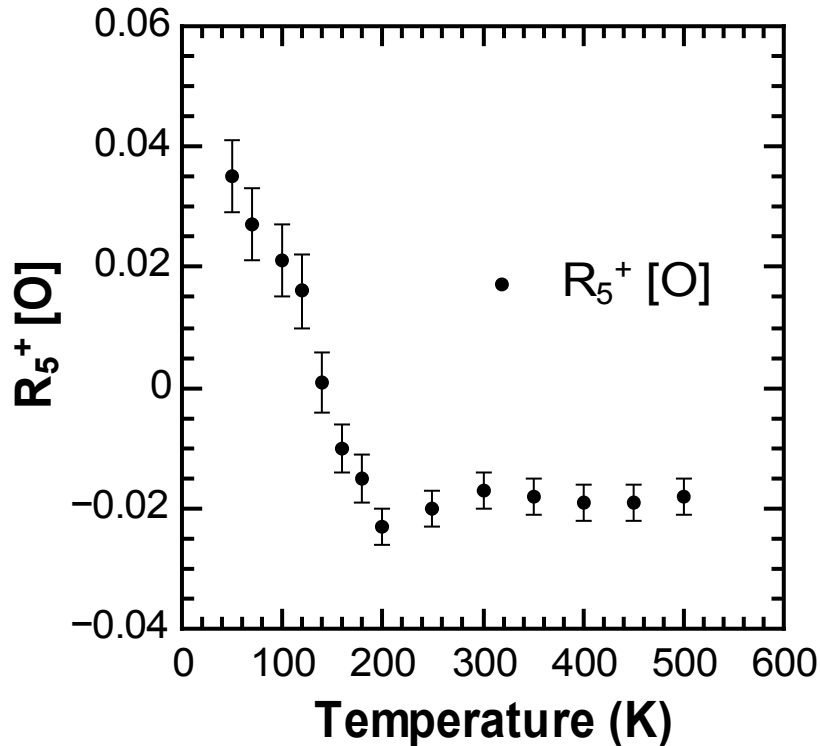


Figure 4.23: $R_5^+ [O]$ mode corresponding to the scissoring distortion where the axial oxygens (O1) are allowed to move along c while the equatorial oxygens (O2) displace along b .

The A-site displacements can be understood when considering the A-O interatomic distances. As the M_3^+ mode decreases on cooling, the rotation of the octahedra will affect the A-site displacements directionally in the ac plane. The rotation means that in general the A-O1 interatomic distances will increase on cooling if the octahedron is pointing towards the A-site - the converse is also true. This means that the shortest A-O1 bond lengths expand and the longest A-O1 distances contract on cooling. For the axial oxygens, the A-O2 distances will expand if the corresponding Fe-O-Fe angle points towards the A-site. Again, the converse is true.

Figure 4.24 show a representation of the perovskite structure viewed down the b -axis. The oxygens are numbered according to their respective distances from the A-site. The A-site is asymmetric with all the longest interatomic distances (9-12) to one side of the $[101]$ and the $[\bar{1}01]$ planes for the respective A-site symmetry equivalent sites. The “arrow head” shaped asymmetry of the AO_{12} dodecahedra might indicate the direction of the Bi^{3+} lone pair alternating along the c -axis (Figure 4.26).

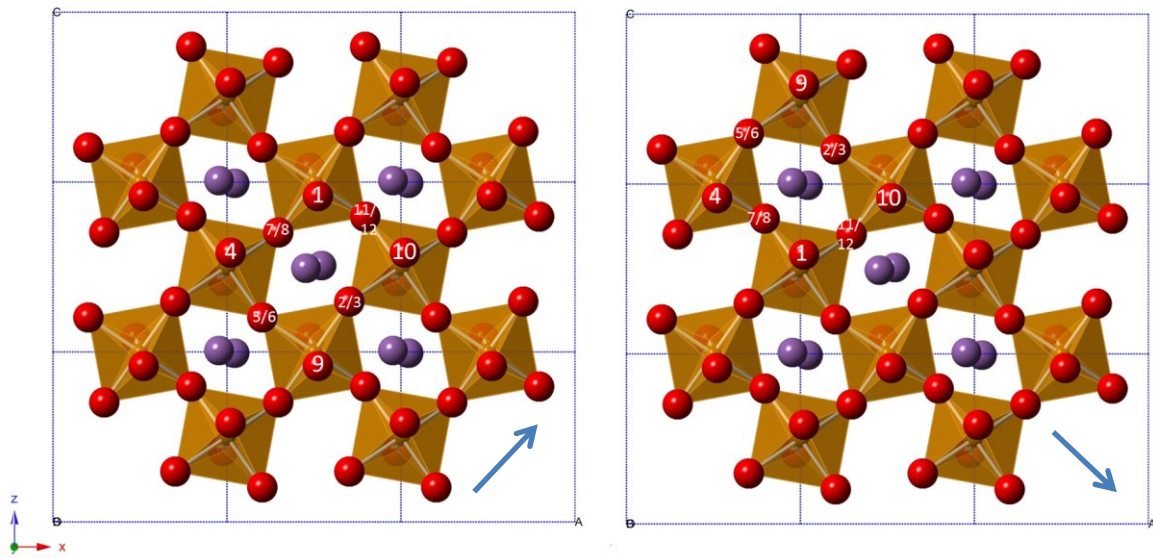


Figure 4.24: Interatomic distances between the A-site (purple) oxygen positions (red) are numbered with increasing distance. Equatorial O2 positions are above and below the plane of the A-site.

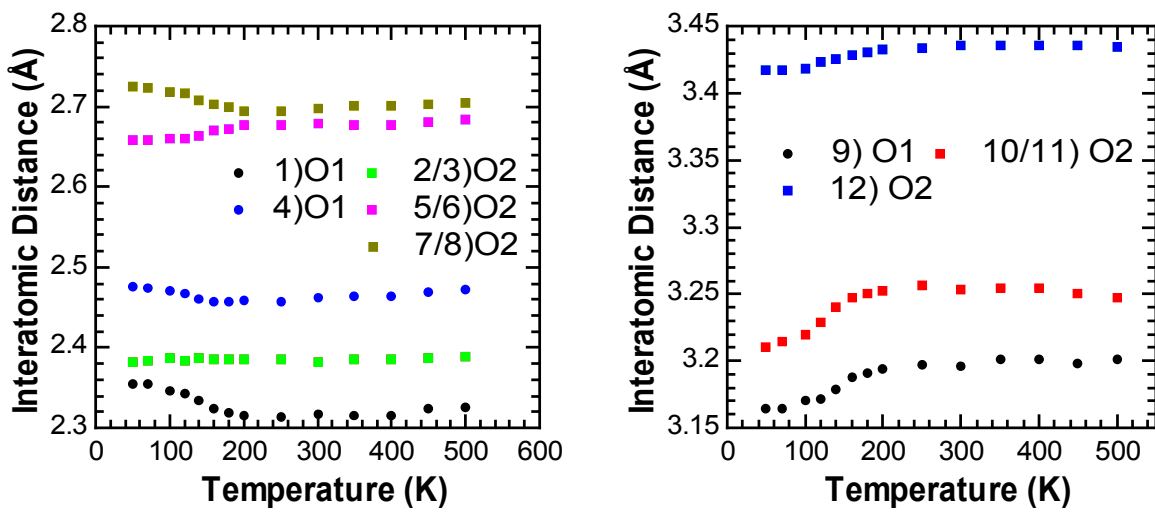


Figure 4.25: Interatomic distances between the A-site and axial (O1) and equatorial oxygens (O2)

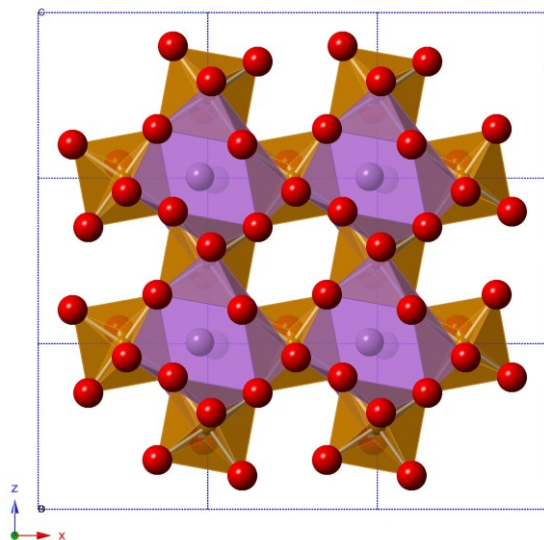


Figure 4.26: The asymmetric shape of the A-site polyhedron based on the 50 K data. The A-site dodecahedra are shown in purple surrounded by the network of the FeO_6 octahedra.

The anisotropy of the A-site is not due to anisotropic thermal displacements. Initially the PND data was refined with anisotropic A-site temperature factors in an attempt to resolve previously mentioned intensity issues. This showed that the U_{33} increases below 200 K with a proportional decrease in the U_{22} parameter (Figure 4.27). This might suggest a shift in the direction of thermal vibrational mode atomic displacements associated with the A-site from the b -axis to the c -axis. However, the magnitudes of the U_{ij} values when compared to BLFO50 in chapter 3 are very small.

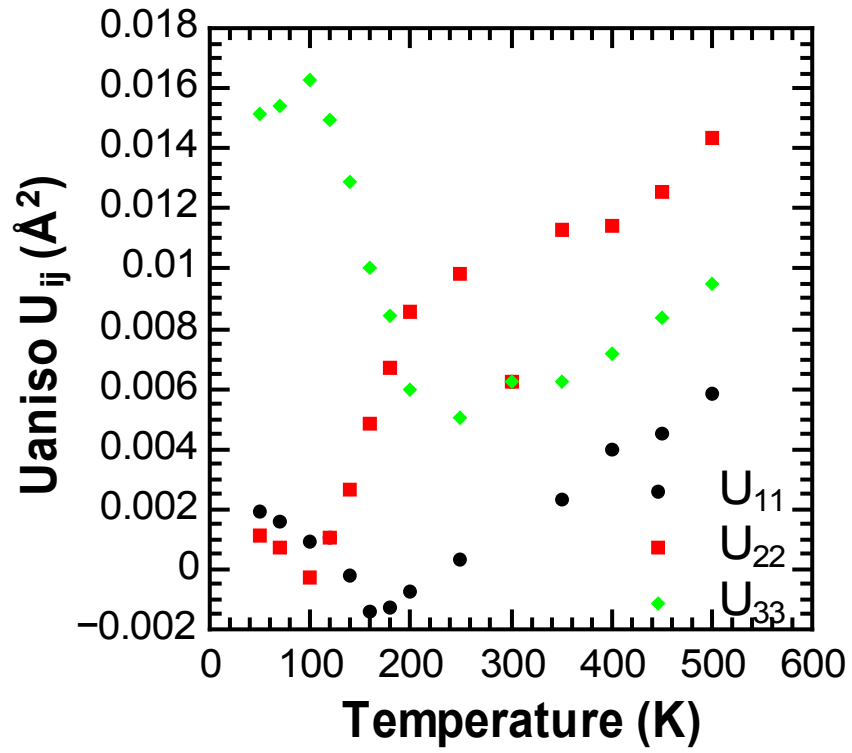


Figure 4.27: Anisotropic atomic thermal displacement parameters (U_{ij}) as a function of temperature along a (U_{11}), b (U_{22}), and c (U_{33}) axes.

4.8 Structural changes and magnetic ordering

Structural changes have been highlighted in relation to the relative permittivity. However, the origin behind the distortions is presumably a competition between a purely structural geometry (bonding) optimisation and magnetostrictive effects arising from the antiferromagnetic ordering. The effect of magnetism as a driving force on the structure is evaluated within this section. Figure 4.28 shows the G_z -type magnetic unit cell of BNFO30 where the antiparallel alignment of the moments along each axis is clearly shown.

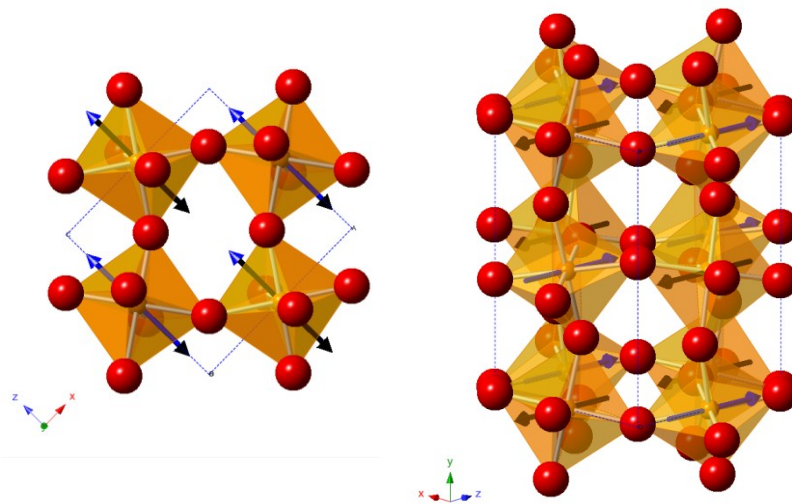


Figure 4.28: The perovskite structure of $\text{Bi}_{0.7}\text{Nd}_{0.3}\text{FeO}_3$ with the G_z -type magnetic cell showing the anti-parallel moments pointing along c -axis of the $Pn'ma'$ unit cell.

An important concept especially with antiferromagnetic systems is that of superexchange. A representation of the p - d hybridisation between the O^{2-} and Fe^{3+} , which results in antiparallel alignment of the spins and antiferromagnetic order, is depicted in Figure 4.29.

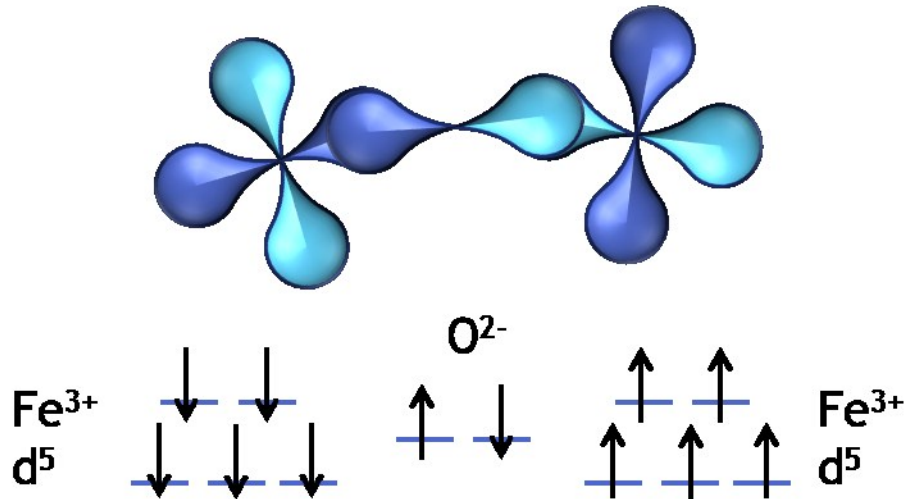


Figure 4.29: *p-d* hybridised orbital representing the Fe-O-Fe interactions of the outer shell

Superexchange is the coupling of the spins of next-nearest-neighbour cations *via* an intermediate anion that results in long-range magnetic order. The ideal conditions for superexchange to occur are when the Fe-O-Fe bond angles are at 180° resulting in optimal orbital overlap. On cooling, the net magnetisation in BNFO30 increases (Figure 4.3) and the Fe-O-Fe angles tend toward 180° (Figure 4.19) accordingly, both the in-phase, M_3^+ , and anti-phase tilts, R_4^+ , decrease in magnitude (Figure 4.20). In the absence of magnetic influences, such as in CaTiO_3 , the M_3^+ and R_4^+ tilts are expected to increase on cooling.²²

Superexchange associated with antiferromagnetic order cannot be the only significant influence on the structure, as this would result in a cubic system with 180° overlap of the *p-d* hybridised orbitals. Purely structural effects, driven by the optimisation of chemical bonding, therefore have to be considered. In BNFO30, these bonding considerations in competition with the changing tilts result in the shortening of the axial Fe-O1 bond and distortion of the octahedra *via* the R_5^+ [O] mode resulting in changes in the polarisation shown in the relative permittivity and loss.

The most significant factor with respect to the optimisation of bond lengths may be optimisation of bonding at the A-site. This should tend to displace the A-site atom further from the centre of its coordination environment as the temperature decreases (in the absence of magnetic influences). This is the case of the non-magnetic CaTiO_3 structure

where both R_5^+ and X_5^+ modes increase in absolute magnitude on cooling representing a shift of the A-site away from the centre of its coordination sphere.²²

The contribution of the A-site on the structure can be regarded in terms of ionic size effects. It has been established that the tilt system is affected by the relative size of the A and B-site cations. The average size of the A-site cation relative to that of the B-site and oxygen lattice has been described by the Goldshmidt tolerance factor (t) which can be used to predict tilts.²³ Typically in a perovskite structure, the tolerance factor ranges between $0.78 \leq t \leq 1.05$.²⁴

For BNFO30, the Nd ionic radius is smaller than that of the bismuth (Nd³⁺ VIII: 1.109 Å, Bi³⁺ VIII: 1.17 Å) and other lanthanide species *e.g.* La (La³⁺ VIII: 1.160 Å)²⁵, such that based on the tolerance factor, the BNFO30 has a larger overall tilt (BNFO30 $t = 0.87$, BLFO30 $t = 0.88$). Woodward describes the effects on the tilt system as an attempt to maximise the A-O covalent bonding while minimising the repulsive A-O overlap.²⁶ To minimise the A-O repulsive interactions and maximise the covalent bonding as a function of temperature (instead of composition) the octahedra must rotate *i.e.*, the anti-phase tilt, R_4^+ , rotates the octahedra in the [101] plane (represented in Figure 4.28) and the in-phase tilt, M_3^+ , rotates the octahedra about the b -axis. The freedom to rotate is dependent on the size of the A-site. In this case, the Nd site is small relative to the oxygen framework allowing both tilts to be utilised in order to minimise the A-site volume. This is in contrast to the lanthanum system BLFO50 studied in chapter 3, which shows negative thermal expansion in a single axis: the c -axis. The La site is much larger and consequently the tolerance factor for BLFO50 ($t = 0.89$) is closer to the ideal cubic perovskite.

4.9 Conclusions

A combination of electrical and structural analysis using temperature PND has shown that Nd doped BiFeO₃ of the composition Bi_{0.7}Nd_{0.3}FeO₃ is a semiconducting relaxor (E_g 0.35 eV) which adopts the GdFeO₃ structure (*Pnma*). The observation of negative thermal expansion within the system prompted further investigation into the crystallographic changes driving this unusual thermal evolution. The detailed crystallographic changes (structural distortions) were analysed using both conventional Rietveld analysis and the symmetry mode tool ISODISTORT. The analysis shows that the material's structure and dielectric behaviour is mediated by superexchange, which drives anomalous changes in the tilt behaviour at low temperature. These changes occur well below the Néel temperature (642 K) due to a competition between covalent bonding and the G_z-type antiferromagnetic order. Superexchange favours linear Fe-O-Fe interactions, which means the in-phase, M₃⁺, and anti-phase, R₄⁺, tilts decrease on cooling. This results in more subtle effects, such as the octahedra distorting and a shortening of the axial Fe-O1 bond together with corresponding A-site displacements (R₅⁺ A-site) along the *c*-axis.

The A-site displacements in the *ac* plane (R₅⁺ and X₅⁺ A-site) correlate with the orthorhombic strain and are in competition with the tilt modes. In particular, the *decrease* of the X₅⁺ (A-site) mode on cooling should lead to the contraction of the unit cell along the *a*-axis. Due to this mode the unit cell contracts along the *a*-axis which is in contrast to expansion of the *b* and *c* axes (and unit cell volume) at low temperature due to the superexchange-driven 'un-tilting' phenomenon. Given the distribution of the longest A-O interatomic distances, the Bi³⁺ lone pair is probably directed along the *c*-axis in an alternating pattern.

In contrast to the BLFO50 system, which utilised an anomalous behaviour of the in-phase tilt (M₃⁺) to relieve strain, the system BNFO30 uses a decrease in both tilts. This is probably due to the relative sizes of the A-site cations competing with the effects of magnetic superexchange.

4.10 References

1. W. Eerenstein, F. D. Morrison, J. Dho, M. G. Blamire, J. F. Scott and N. D. Mathur, *Science*, 2005, **307**, 1203.
2. I. Levin, M. G. Tucker, H. Wu, V. Provenzano, C. L. Dennis, S. Karimi, T. Comyn, T. Stevenson, R. I. Smith and I. M. Reaney, *Chem. Mater.*, 2011, **23**, 2166-2175.
3. I. Levin, S. Karimi, V. Provenzano, C. L. Dennis, H. Wu, T. P. Comyn, T. J. Stevenson, R. I. Smith and I. M. Reaney, *Phys. Rev. B*, 2010, **81**, 020103.
4. R. Przeniosło, I. Sosnowska, M. Loewenhaupt and A. Taylor, *J. Magn. Magn. Mater.*, 1995, **140-144, Part 3**, 2151-2152.
5. W. Sławiński, R. Przeniosło, I. Sosnowska and E. Suard, *J. Phys.: Condens. Matter*, 2005, **17**, 4605.
6. R. L. White, *J. Appl. Phys.*, 1969, **40**, 1061-1069.
7. D. Treves, *J. Appl. Phys.*, 1965, **36**, 1033-1039.
8. S. C. Parida, S. Dash, Z. Singh, R. Prasad, K. T. Jacob and V. Venugopal, *J. Solid State Chem.*, 2002, **164**, 34-41.
9. A. C. Larson and R. B. Von Dreele, Los Alamos National Laboratory 1994.
10. B. Toby, *J. Appl. Crystallogr.*, 2001, **34**, 210-213.
11. W. C. Koehler, E. O. Wollan and M. K. Wilkinson, *Phys. Rev.*, 1960, **118**, 58-70.
12. T. Peterlin-Neumaier and E. Steichele, *J. Magn. Magn. Mater.*, 1986, **59**, 351-356.
13. B. J. Campbell, H. T. Stokes, D. E. Tanner and D. M. Hatch, *J. Appl. Crystallogr.*, 2006, **39**, 607-614.
14. J. T. S. Irvine, D. C. Sinclair and A. R. West, *Adv. Mater.*, 1990, **2**, 132-138.
15. A. R. West, D. C. Sinclair and N. Hirose, *J. Electroceram.*, 1997, **1**, 65-71.
16. D. Viehland, S. J. Jang, L. E. Cross and M. Wuttig, *J. Appl. Phys.*, 1990, **68**, 2916-2921.
17. K. Hirota, S. Wakimoto and D. E. Cox, *Journal of the Physical Society of Japan*, **75**, 111006.
18. A. Rotaru, D. C. Arnold, A. Daoud-Aladine and F. D. Morrison, *Phys. Rev. B*, 2011, **83**, 184302.
19. A. K. Jonscher, *Dielectric Relaxation in Solids*, Chelsea Dielectrics Press, London, 1983.
20. K. Kalantari, I. Sterianou, S. Karimi, M. C. Ferrarelli, S. Miao, D. C. Sinclair and I. M. Reaney, *Adv. Funct. Mater.*, 2011, **21**, 3737-3743.
21. M. S. Islam, *J. Mater. Chem.*, 2000, **10**, 1027-1038.
22. K. S. Knight, *J. Alloys Compd.*, 2011, **509**, 6337-6345.
23. V. M. Goldschmidt, *Naturwissenschaften*, 1926, **14**, 477.
24. C. A. Randall, A. S. Bhalla, T. R. ShROUT and L. E. Cross, *J. Mater. Res.*, 1990, **5**, 829-834.
25. R. D. Shannon, *Acta Crystallogr. Sect. A: Found. Crystallogr.*, 1976, **32**, 751-767.
26. P. Woodward, *Acta Crystallogr. Sect. B: Struct. Sci.*, 1997, **53**, 44-66.

Variations in the electrical properties of rare earth doped BiFeO_3

5.1 Introduction

This chapter serves as an overview to the development and optimisation of the electrical properties of $\text{Bi}_{1-x}\text{La}_x\text{FeO}_3$. A number of key samples of the composition $\text{Bi}_{0.6}\text{La}_{0.4}\text{FeO}_3$ are discussed where changes in the second step of the synthesis result in significantly different conductivities. Similar electrical behaviour is found at other compositions such as in $\text{Bi}_{0.75}\text{La}_{0.25}\text{FeO}_3$.

As stated in the Introduction, BiFeO_3 is currently the only known room temperature multiferroic oxide and is therefore a good candidate for further research due to its high ferroelectric ($T_c \sim 810 - 830 \text{ }^\circ\text{C}$)^{1, 2} and antiferromagnetic ($T_N \sim 370 \text{ }^\circ\text{C}$) ordering temperature.³ Theoretical calculations show that the band gap of BiFeO_3 is *circa*. 2.8 eV,⁴ which means BiFeO_3 is a wide band-gap semiconductor which should show only modest levels of conductivity at ambient temperatures; the high levels of conductivity often observed is due to the defect chemistry. Optimisation of the electrical properties can therefore be achieved through modifying the synthesis route.

Producing high-purity, single-phase, electrically insulating BiFeO_3 ceramics is problematic due to parasitic secondary phases that nucleate around the grain boundaries⁵ *i.e.*, $\text{Bi}_{25}\text{FeO}_{39}$ and $\text{Bi}_2\text{Fe}_4\text{O}_9$.⁶ The volatility of Bi_2O_3 at high temperatures can lead to sample non-stoichiometry due to bismuth loss and decomposition into secondary phases, and also oxygen loss leading to reduction of Fe (III) to Fe (II). These reasons have been cited as potential origins for conductivity within BiFeO_3 .⁷

One approach to reduce the amount of secondary phases is doping on the B-site. Valant *et al.* describe the influences on the secondary phases suggesting that small amounts of impurities such as Ti^{4+} on the B-site can dramatically reduce the amount of secondary phases such as $\text{Bi}_2\text{Fe}_4\text{O}_9$.⁸ This doping with Ti^{4+} has also been shown to improve the electrical properties, producing electrically insulating samples in the $\text{Bi}_{1-x}\text{Nd}_x\text{Fe}_{1-y}\text{Ti}_y\text{O}_3$ system.⁹ Small amounts of Ti^{4+} , *circa*. 3 % change the electrical response from an electronically conducting

sample with an activation energy *circa.* 0.29 eV, which is typically associated with polaron hopping, to an insulating sample with an activation energy *circa.* 1.0 eV associated with oxygen vacancies.⁹ The Ti^{4+} compensates for the partial reduction of Fe^{3+} *i.e.*, $\text{Bi}(\text{Fe}^{3+}_{1-x}\text{Fe}^{2+}_x)\text{O}_{3-x/2}$ eliminating the need for a compensation mechanism *via* oxygen vacancies.⁹ This methodology undoubtedly works and has been used to try to clarify the nature of the PbZrO_3 -like phase and the possibility of an antiferroelectric phase.⁹ Other synthesis and doping methods are available, such as rapid liquid phase sintering^{10, 11}, excess Bi_2O_3 ,^{7, 12} and acid leaching¹² to remove secondary phases.

Rapid liquid phase sintering typically uses very short reaction times, for example Wang *et al.* sinter their samples for 450 s at 880 °C.¹¹ The melting point for Bi_2O_3 is *circa.* 817 °C¹³, however the process is so quick that it limits volatilisation of Bi_2O_3 and the samples are electrically insulating. This allowed polarisation vs. electric field (P - E) loops to be collected at room temperature requiring a field of 100 kVcm^{-1} to saturate the sample (remanent polarisation, $P_r \approx 4.0 \mu\text{Ccm}^{-2}$).¹¹ Pradhan *et al.* used excess Bi_2O_3 (Bi:Fe 1.2:0.8) and suggest that excess Bi^{3+} compensates for the loss of Bi_2O_3 during the long sintering process or Fe deficiency promotes the Fe^{3+} state and the absence of oxygen vacancies.⁷ Either way, they produce X-ray diffraction patterns that appear single phase and well saturated P - E loops with a reported $2P_r$ of 10 μCcm^{-2} with an applied field of 150 kVcm^{-1} .⁷ Electrical data in this study is limited to room temperature total capacitance and loss as a function of frequency, which appears to be the general case for studies into BiFeO_3 .⁷

Methods such as A-site doping, which is the method adopted for the synthesis of samples discussed in this thesis, have the advantage of lowering the ferroelectric phase transition closer to room temperature allowing study of the transition reduction of leakage currents, allowing potential exploitation in device applications.

5.2 Experimental

The synthesis was carefully performed *via* conventional solid-state methods as outlined in the experimental chapter 2.1. Stoichiometric amounts of Bi_2O_3 and Fe_2O_3 were mixed with La_2O_3 , which was dried at 1000 °C prior to weighing. The final calcination temperature for samples mentioned within this chapter varies. The initial calcination step was performed at 800 °C (5 hrs.). The second calcination step temperature and synthesis atmosphere will be outlined as required for each sample in the following sections.

Powder neutron diffraction (PND) data were collected using the HRPD diffractometer at the ISIS neutron spallation source, Rutherford Appleton Laboratories. Rietveld refinements were performed using the general structural analysis system (GSAS) and its associated graphical user interface program (EXPGUI).

5.3 Results

The following section will outline changes in the phase compositions of $\text{Bi}_{0.6}\text{La}_{0.4}\text{FeO}_3$ (BLFO40) as a function of temperature. Subsequent sections will outline the electrical behaviour of a number of key BLFO40 samples. These samples described in the subsequent sections were synthesised from a common starting batch; after the first calcination step from which aliquots were taken and synthesis conditions were varied. Changes in synthesis conditions produce a variety of different conductivities.

5.4 Preliminary Structural analysis – BLFO40 with temperature

The preliminary analysis of the BLFO40 sample shows that at room temperature it is a phase mixture of incommensurate '*Imma*' (circa. 54 wt%) and a commensurate *Pnma* (circa. 45 wt%) with a minor secondary phase of Fe_2O_3 . The '*Imma*' and *Pnma* phases approximate to a $\sqrt{2} a_p \times 2 a_p \times \sqrt{2} a_p$ unit cell. At higher temperature, above 460 K, the *a* and *c* ($\sqrt{2} a_p$) lattice parameters of the '*Imma*' unit cell become equivalent and the phase can be refined as tetragonal *I4/mcm* (Figure 5.1).

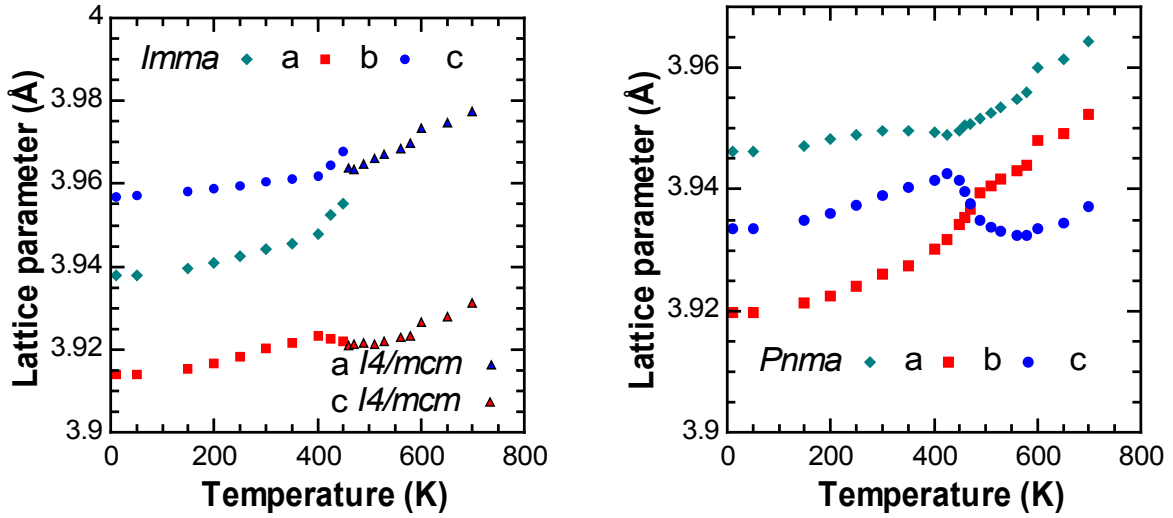


Figure 5.1 : Reduced (pseudo cubic) cell lattice parameters for the '*Imma*', *I4/mcm* and *Pnma* phases as a function of temperature for BLFO40. Lattice parameters with a $2 a_p$ relationship are shown in red (squares) and $\sqrt{2} a_p$ in cyan and blue (diamonds and circles, respectively).

The phase fractions as a function of temperature are shown in Figure 5.2 where it can be seen that the majority phase at high temperature is *Pnma*. At higher temperature, it is therefore possible to refine the *Pn'ma'* G_z -type magnetic phase shown to be present in $\text{Bi}_{0.5}\text{La}_{0.5}\text{FeO}_3$ (BLFO50), Chapter 3. The net magnetisation determined from the refinements is consistent with BLFO50 over the temperature range 460 - 700 K (Figure 5.3) and results in a Néel temperature just above 700 K for BLFO40 (BLFO50 $T_N = 704 \pm 3$ K). Below 460 K, the magnetic contributions were not refined due to the increasing complexity of the refinement.

There are additional reflections (at 1.54 Å and 1.66 Å d-spacing) below 460 K that can be indexed by a doubling of the *Imma* (or *Pnma*) *c*-axis. The doubling of the *Imma* *c*-axis is consistent with an incommensurate structure of the composition $\text{Bi}_{0.75}\text{La}_{0.25}\text{FeO}_3$ reported by Rusakov *et al.*¹⁴

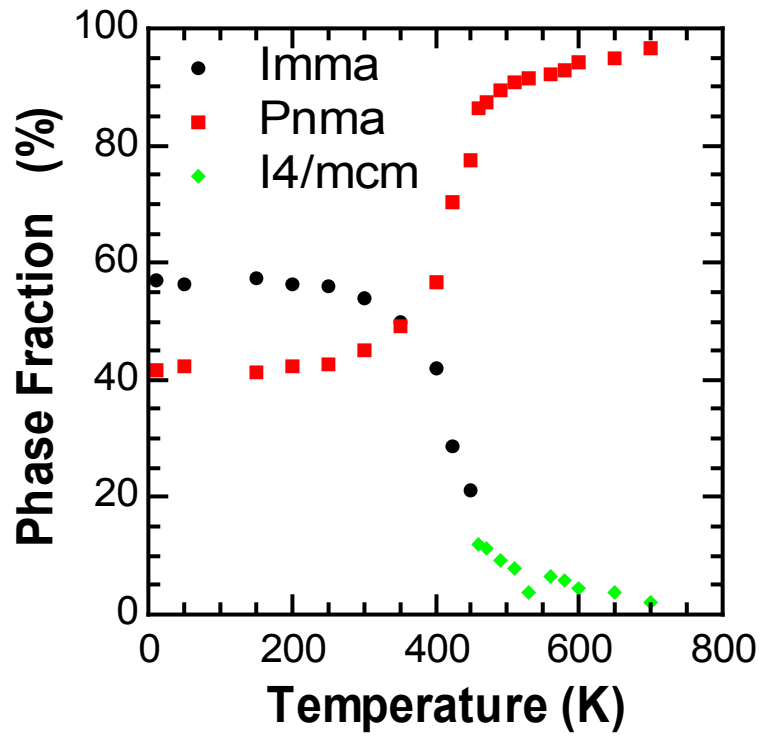


Figure 5.2: Phase fractions for the body-centred and primitive cells of the $\text{Bi}_{0.6}\text{La}_{0.4}\text{FeO}_3$ phase mixture.

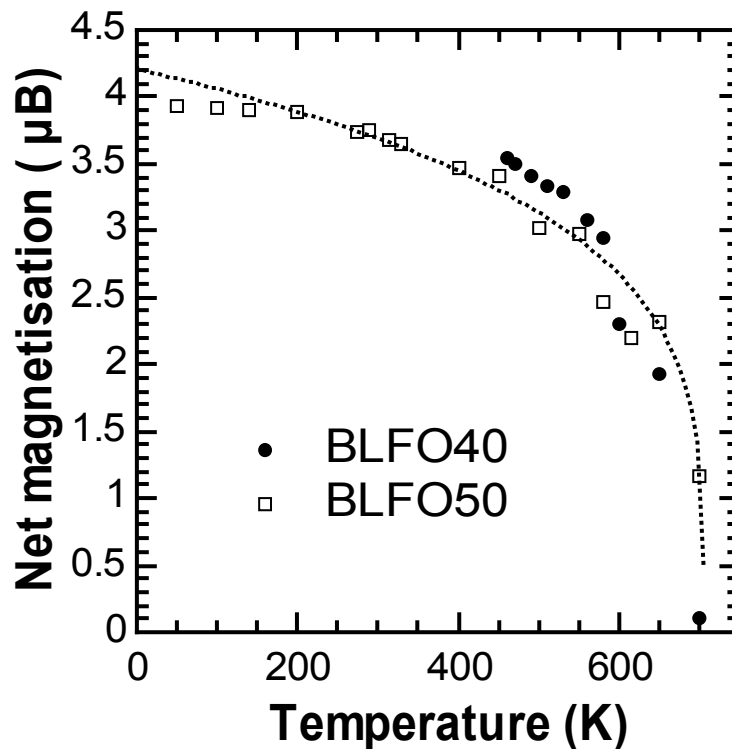


Figure 5.3: Net magnetisation (along c) as a function of temperature as determined from Rietveld refinement of PND data. Dotted black line represents a fit of the magnetic data to a power law for BLFO50 (see Chapter 3).

5.5 Electrical response - BLFO40 1000 °C in Air

The following electrical data and analysis relates to a sample of the composition $\text{Bi}_{0.6}\text{La}_{0.4}\text{FeO}_3$. All calcination steps were in air and the second calcination step temperature was 1000 °C (5 hrs.).

The electrical data at 390 K shows a broad feature in the M'' spectra on heating for the first time and the sample is electrically inhomogeneous (Figure 5.4). This is due to a significant contribution from multiple electroactive regions with similar time constants. These contributions may arise from the grain boundary, the presence of different phases within the sample or an inhomogeneous distribution of defects between the core and outer region of the grains (*e.g.* a core-shell type model).

On heating, the M'' spectra change such that the electrical response appears Gaussian* by 645 K. If the peak profile is considered on heating *i.e.*, from 10^3 to 10^4 Hz at 390 K there appears to be two significant contributions to the overall response (Figure 5.4). This plateau becomes less distinct as the sample is heated. This might suggest that the electroactive region, which dominates the modulus data at lower frequency, has a larger associated activation energy than the response appearing at higher frequencies. This would result in the responses 'merging' due to the time constants and the f_{max} tending towards equivalence as the sample is heated.

The corresponding response in Z'' relating to the broad response in the M'' is obscured by a low frequency response; this is particularly evident at 390 K on heating (Figure 5.4). A small Z'' response (low resistivity) and large response in the M'' spectra (low capacitance) is consistent with a conducting bulk that can be described by the brick layer model outlined in chapter 2.

On cooling, the Z'' response remains Debye-like, however the M'' response broadens on cooling. This is particularly evident at high frequency beyond the peak maxima and is due to multiple contributions to the overall response. The relationship between the capacitive response and the thickness of the electroactive domains has been outlined by Irvine *et al.*¹⁵ and is described in chapter 2. They show that even a small phase fraction, *i.e.*, a minor

* The peak profiles are Debye-like but for a simple approximation to determine the full width half maximum a Gaussian distribution can be used.

secondary phase, with a thin domain cross-section can have a significant contribution to the overall capacitance.¹⁵

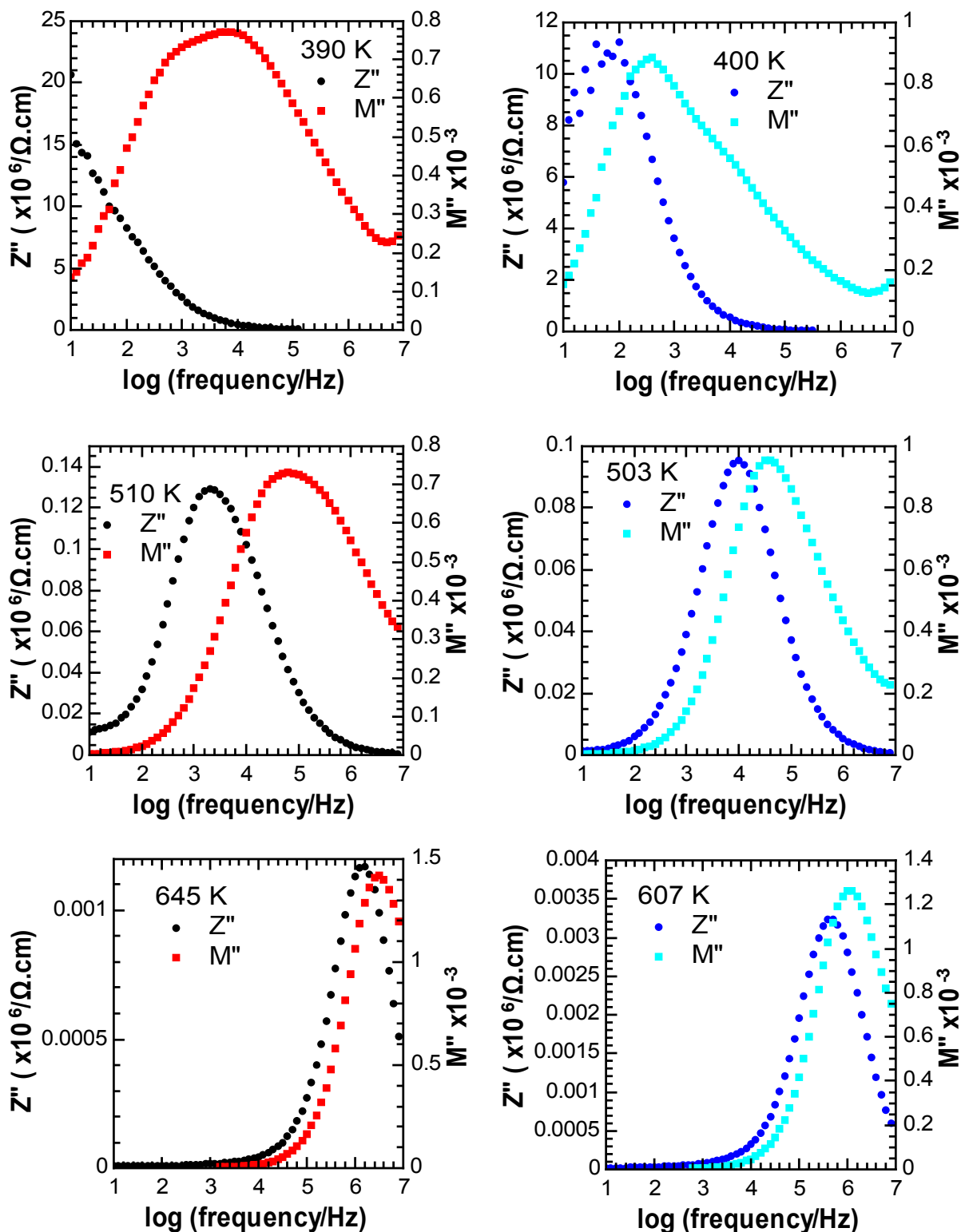


Figure 5.4: Z'' and M'' spectra as a function of temperature show a broad modulus peak (due to two overlapping electroactive responses) which narrows on heating (left) and broadens again on cooling (right). The thermal cycle is shown anticlockwise from 390 K (top left).

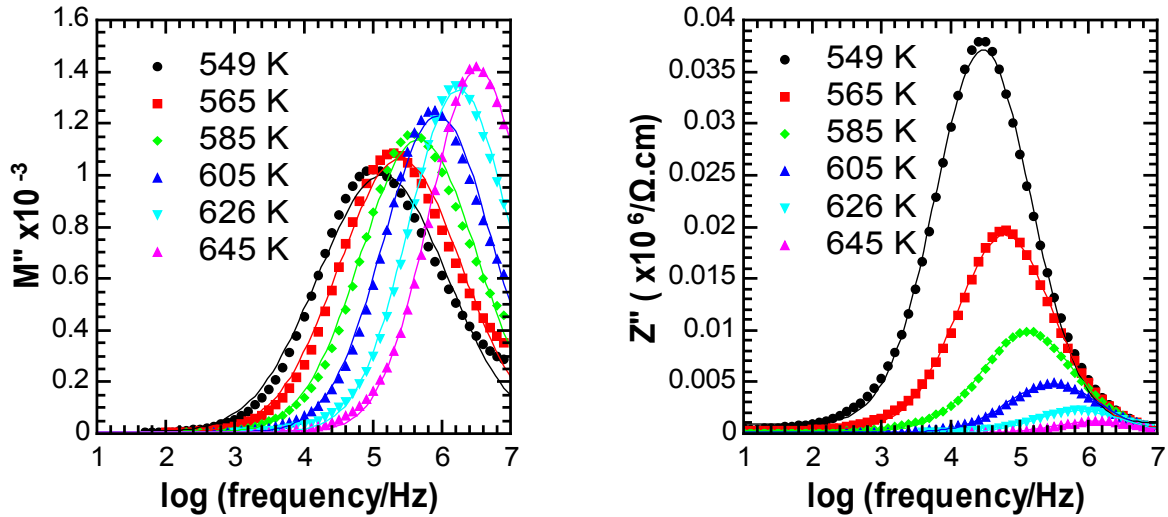


Figure 5.5: Immittance spectra of BLFO40 Air above 549 K showing an electroactive component with similar peak frequencies dominating the response in both M'' and Z'' spectra.

Data collected on heating can be fitted with a Gaussian distribution above 549 K, Equation 5.1, from which the full width half-maximum ($FWHM$) can be calculated. The parameter x_c represents the frequency corresponding to the peak maximum, σ is the standard deviation in values about the maximum and Y_0 and A are arbitrary terms relating to the displacement of the peak and its magnitude.

$$f(x) = Y_0 + A \frac{\sqrt{2\pi}}{\sigma} e^{-2\left(\frac{x-x_c}{\sigma}\right)^2} \quad \text{Equation 5.1}$$

The $FWHM$ can be calculated using Equation 5.2.

$$FWHM = 2\sqrt{2\ln(2)}\sigma \quad \text{Equation 5.2}$$

An ideal Debye response for a single relaxation should have a $FWHM$ circa 1.14 decades.¹⁶ Providing the $FWHM$ of a response does not exceed 1.5 decades, approximate values of the capacitive and resistive elements can be obtained.¹⁶ From the Table 5.1 and Table 5.2, the $FWHM$ of the responses tend towards 1.14 decades with increasing temperature. This shows that there are still at least two electroactive responses with different activation energies contributing to the electrical response.

Table 5.1: *FWHM* and fit parameters for the Z'' response as a function of temperature.

Temperature (K)	A	σ	x_c	Y_0	<i>FWHM</i> (\log_{10})
549	6.28×10^{-2}	1.39	4.47	9.82×10^{-4}	1.42
565	3.24×10^{-2}	1.38	4.79	4.98×10^{-4}	1.41
585	1.62×10^{-2}	1.37	5.13	2.44×10^{-4}	1.40
605	7.80×10^{-3}	1.33	5.49	9.86×10^{-5}	1.36
626	3.46×10^{-3}	1.28	5.85	3.99×10^{-5}	1.30
645	1.74×10^{-3}	1.23	6.12	2.31×10^{-5}	1.25

Table 5.2: *FWHM* and fit parameters for the M'' response as a function of temperature.

Temperature (K)	A	σ	x_c	Y_0	<i>FWHM</i> (\log_{10})
549	2.34	1.88	5.14	5.16×10^{-3}	1.92
565	2.37	1.79	5.40	3.29×10^{-3}	1.83
585	2.40	1.69	5.67	2.94×10^{-3}	1.72
605	2.41	1.57	5.94	4.07×10^{-3}	1.60
626	2.42	1.46	6.25	6.16×10^{-3}	1.49
645	2.46	1.40	6.52	7.61×10^{-3}	1.44

The approximate magnitudes of the resistance and capacitance of the dominant component in the spectra can be determined from the peak position and magnitude, as outlined in chapter 2. Activation energies can be determined from the time constant, ($\tau = RC = \frac{1}{2\pi f_{max}}$) which follows Arrhenius type behaviour similar to the conductivity (Equation 5.3).

This should produce more reliable activation energies than conductivities as it only requires f_{max} to be determined, eliminating the need for the estimation of R or C .

$$\tau = \tau_0 \exp^{E_a/kt} \quad \text{Equation 5.3}$$

Based on the $x_c (= \log_{10} f_{max})$ values in Table 5.1 the activation energy associated with most resistive component which dominates the Z'' spectra on heating can be estimated to be *circa.* 1.21 - 1.25 eV (549 - 645 K). On cooling, the equivalent analysis results in an estimated activation energy *circa.* 0.96 - 0.99 eV. On heating, the M'' spectra at high temperature has a broad response with a *FWHM* above 1.5 decades for all but two data collection temperatures. Based on these limited data the activation energy associated with the M'' responses is *circa.* 1.14 eV, which is in broad agreement with the equivalent calculation using the Z'' spectra.

Determining activation energies and capacitances, particularly at low temperature, from the spectra is difficult. However, other samples such as $\text{Bi}_{0.75}\text{La}_{0.25}\text{FeO}_3$ (BLFO25) show similar behaviour, as will be discussed later.

5.6 Electrical response - BLFO40 1000 °C N_2

The analysis in this section relates to a sample from the same initial starting batch as BLFO40 Air ($\text{Bi}_{0.6}\text{La}_{0.4}\text{FeO}_3$). The second step calcination temperature remained at 1000 °C (5 hrs.) However, the final step synthesis atmosphere was changed and enriched with nitrogen (BLFO40 N_2). This change in the synthesis route produces a much more homogeneous, electrically insulating response. Consequently, the broad features in the M'' and Z'' spectra cannot be observed. High temperature electrical data from 468 K (Figure 5.6 and Figure 5.7) show a single response in the M'' and Z'' spectra with a *FWHM* close to the ideal theoretical response. This corresponds to a temperature range where the incommensurate *Imma* phase transforms to *I4/mcm* and the dominant phase is *Pnma* (Figure 5.2), although it is not clear at this stage if this is a coincidence or not.

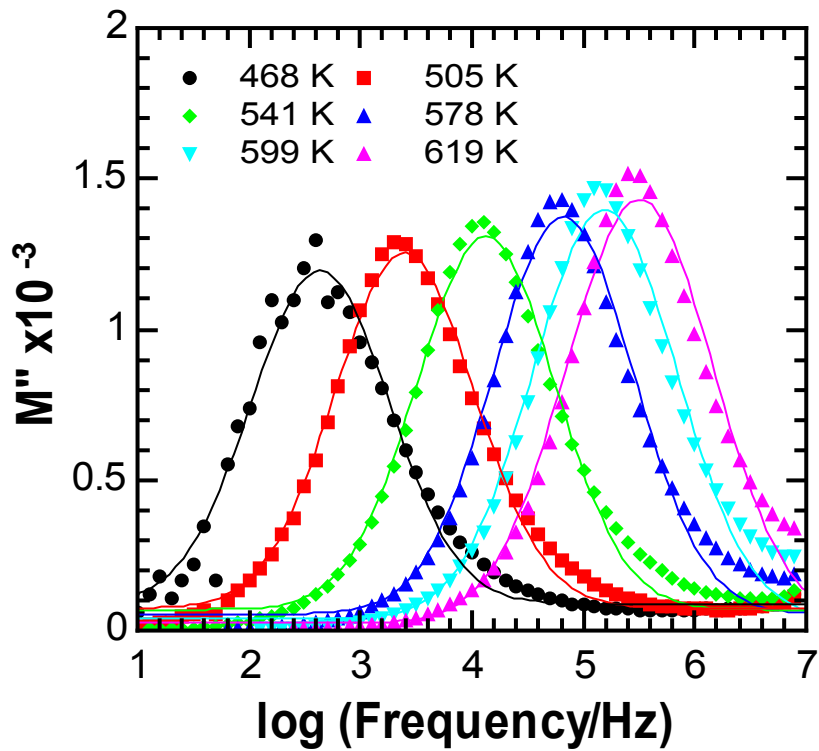


Figure 5.6: M'' spectra as a function of temperature showing an electroactive response with a $FWHM$ between 1.26 - 1.34 decades.

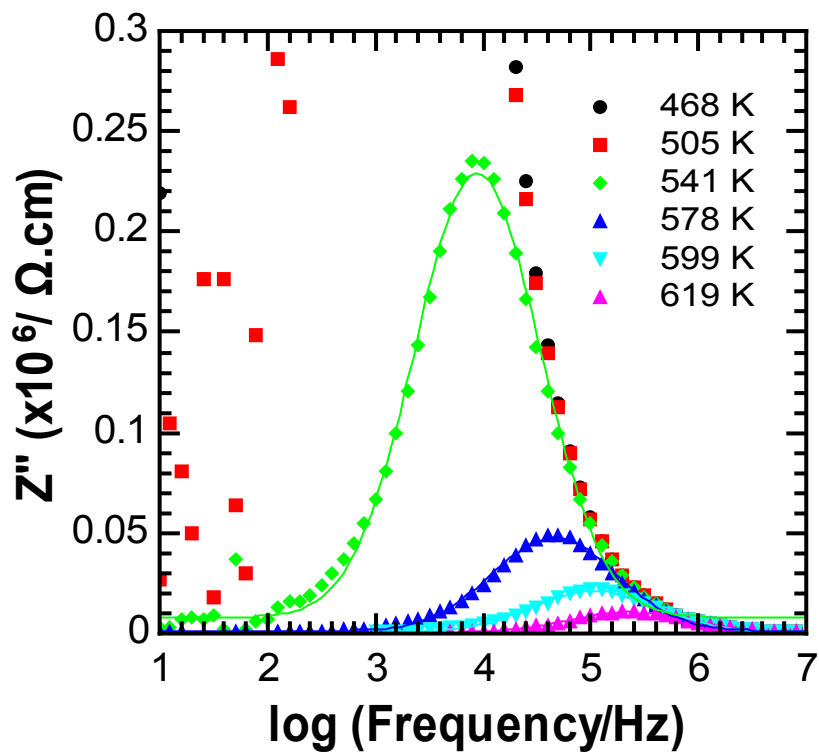


Figure 5.7: Z'' spectra as a function of temperature showing an electroactive response with a $FWHM$ between 1.18-1.19 decades.

Calculations based on x_c values from Z'' spectra gives an estimated activation energy in the range 1.18 - 1.2 eV, which is in agreement with the values obtained from the M'' (1.10- 1.19 eV). These activation energies are similar to the high temperature response found in the BLFO40 Air sample. Capacitance values obtained from fitting the response in the complex modulus are in the range 27.5 pFcm^{-1} - 26.0 pFcm^{-1} over the temperature range 505 K - 619 K and correspond to magnitudes associated with a bulk response¹⁵

5.7 BLFO40 1100 Air

The synthesis route was systematically changed from the BLFO40 Air synthesis route. This time the second step synthesis temperature was 1100 °C for a period of 5 hrs (BLFO40 1100) and the atmosphere was not enriched. This sample is more conducting than the samples described previously. There are at least two electroactive responses within the sample. The bulk response dominates the M'' spectra (Figure 5.8) with estimated capacitances between $1.15 - 12.8 \text{ pFcm}^{-1}$ and a grain boundary response dominates the Z'' spectra. Based on a fit of the peak position, x_c , in the M'' spectra, an activation energy of the bulk response is estimated to be between 0.46 - 0.5 eV. The *FWHM* decreases on cooling from 1.4 to 1.14 decades over the temperature range 307 - 226 K. This is a similar range of *FWHM* found for the bulk response in the M'' spectra of BLFO40 N₂ at higher temperature. Overall the observed behaviour is consistent with an electrically homogenous bulk response.

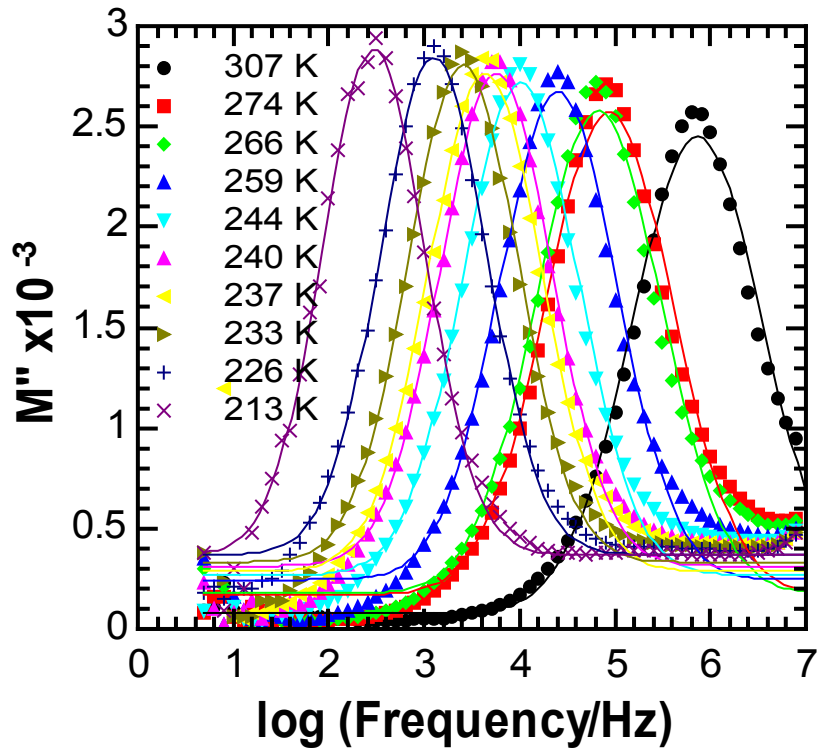


Figure 5.8: M'' spectra of BLFO40 1100 between 307 – 213 K on cooling shows a decreasing $FWHM$ with temperature.

5.8 Comparison of bulk and “total sample” permittivities

A comparison of the relative permittivities of all the BLFO40 samples against sweep data of an insulating sample at a high frequency (representing the bulk contribution) may indicate the nature of the capacitive response in the samples. The relative permittivity of BLFO40 Air was calculated from the high frequency intercept of the M^* complex plane plot *i.e.*, the total capacitance of the sample. The permittivity of BLFO40 N_2 and BLFO40 1100 are based on a fit of the bulk response in the complex modulus and represents only the bulk permittivity.

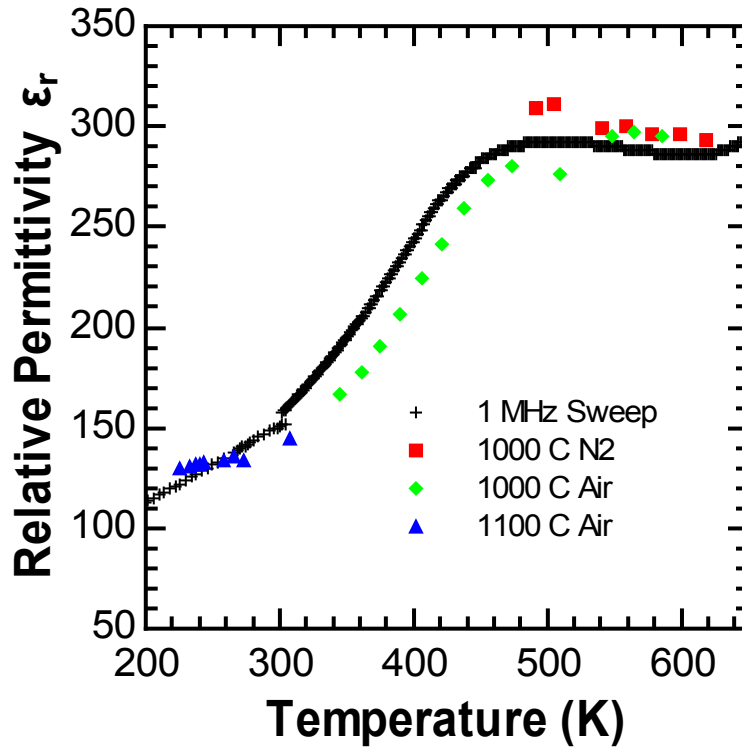


Figure 5.9: BLFO40 N₂ and BLFO40 1100 bulk permittivities and BLFO40 Air sample permittivity as a function of temperature compared against high frequency (1 MHz) permittivity calculated from the total capacitance measurements. Correlation between BLFO40 N₂ and the 1 MHz data suggest that the permittivities are related to the bulk.

Strong correlation between the permittivities suggests that despite being unable to directly measure the bulk response in the insulating samples at lower temperatures, the origins of the capacitive responses are similar in all the samples *i.e.*, dominated by bulk behaviour. The slight suppression of the calculated permittivity for BLFO40 Air may be due to a small grain boundary contribution (Figure 5.9).

As the capacitances are broadly the same, it suggests differences in the samples are due to differing conductivities arising from changes in the defect chemistry and the number available charge carriers. Similar activation energies found in BLFO40 Air and N₂ at high temperature suggest that at the very least the high temperature conduction process is the same. Activation energies *circa* 1.2 eV are associated with electronic conduction dominated by the presence of oxygen vacancies.¹⁷

5.9 BLFO25 1000 °C N₂

Electrical data for Bi_{0.75}La_{0.25}FeO₃ (BLFO25) shows some similarities to BLFO40 Air. All synthesis steps were performed under an enriched nitrogen atmosphere. The second calcination step was at 1000 °C (5 hrs.).

Rietveld refinement of room temperature PND data on samples of this composition shows a phase mixture of incommensurate *Imma* and a “PbZrO₃-like” phase refined as *Pbam*. On heating, the phase composition should favour the ‘*Imma*’ phase. This reasoning is based on the phase sequence as a function of composition by authors such as Rusakov *et al.*¹⁴ and Troyanchuk *et al.*^{18, 19} where the ‘*Imma*’ phase is found in more heavily doped samples. The estimated phase fractions determined from the Rietveld refinements of PND data are sensitive to the starting position of the refinement and the fitting of broad low intensity reflections that are believed to be incommensurate peaks associated with the *Imma* phase. The best refinements at room temperature suggest that the dominant phase is the “PbZrO₃-like” phase.

The electrical data show two distinct electroactive responses, which are more easily resolved than in the similar BLFO40 Air electrical data (Figure 5.10). The first electroactive response in the modulus is evident at about 10³ Hz at 399 K with a second response at about 10⁵ Hz. On heating, the first, low frequency, response increases in magnitude as the second response decreases and it becomes hard to distinguish from the high frequency edge of the first response. Approximate activation energies can be determined from estimates of the positions of the peak maxima, f_{max} . The first, low frequency, component has an activation energy between 0.81 - 0.85 eV, as determined from f_{max} over the temperature range 341 – 415 K and the second higher frequency component has an activation energy *circa* 0.46 - 0.53 eV.

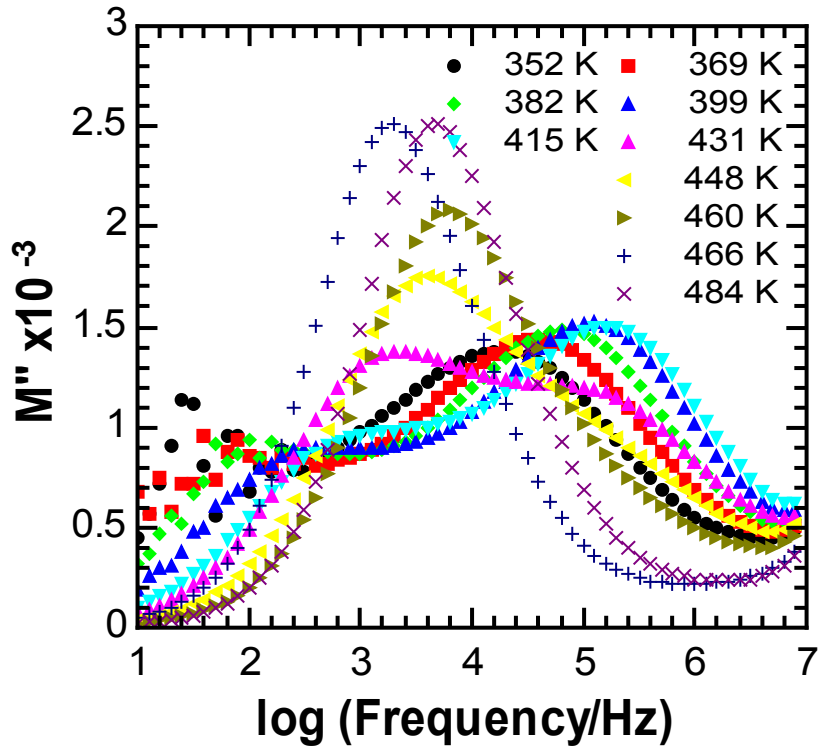


Figure 5.10: Low temperature M'' response of BLFO25

Above 466 K, the response appears Debye-like and again can be approximated by fitted with a Gaussian distribution. Based on a fit of the complex modulus over the temperature range 466 - 594 K the capacitances are in the range $12.1 - 15.7 \text{ pFcm}^{-1}$, again characteristic of a bulk response. Above 538 K, there appears to be a significant change in the activation energy shown in Figure 5.11 by a change in the displacement of the electroactive response. The activation energies calculated from the highest temperatures are fitted on a limited number of points and therefore are approximate. The magnitudes of the activation energy have been determined quantitatively from f_{max} (actually x_c) and are summarised in Table 5.3.

Table 5.3: Table of activation energies, E_a , determined on heating BLFO25

Temperature range (K)	Estimated E_a (eV)
386 – 460 (C1)	0.81 – 0.85
341 – 415 (C2)	0.46 – 0.53
466 – 502	<i>circa.</i> 0.91
558 – 594	<i>circa.</i> 1.81

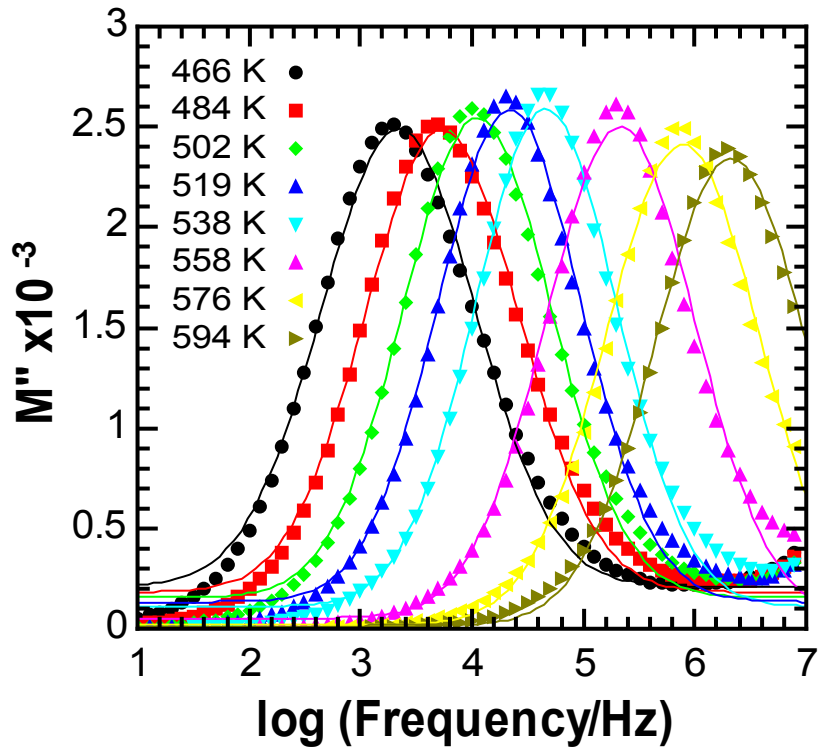


Figure 5.11: High temperature M'' response of BLFO25 showing a change in activation energy above 538 K. *FWHM*: 1.41 (466 K) – 1.31 (538 K) – 1.39 decades (594 K).

On cooling (Figure 5.12) and reheating (Figure 5.13), the peaks in the modulus and impedance spectra are broad, indicating that there is more than one component. However, the *FWHM* of the peak in the M'' spectra is smaller than the initial heating suggesting the sample is more homogeneous and there is a change in the resistivities of the electroactive regions. The time constants of the components are almost identical and individual components cannot easily be resolved. Estimates of the activation energy calculated from the M'' spectra from the cooling data between 586 - 475 K gives a range between 0.71 – 0.90 eV. This is consistent with the first component on the initial heating. The activation energy is consistent with the Z'' spectra over the same temperature range (0.87 -1.02 eV).

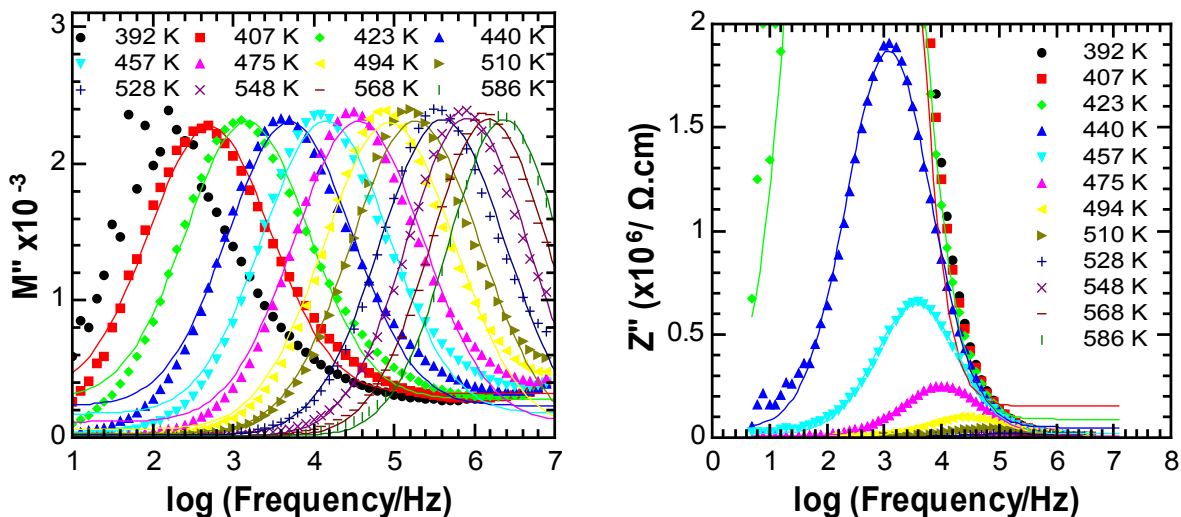


Figure 5.12: Imaginary modulus (left) and impedance (right) spectra collected on cooling. Fitting of the M'' spectra with Gaussian function results in $FWHMs$ in the range 1.43 (586 K) – 1.66 (494 K) – 1.55 decades (407 K).

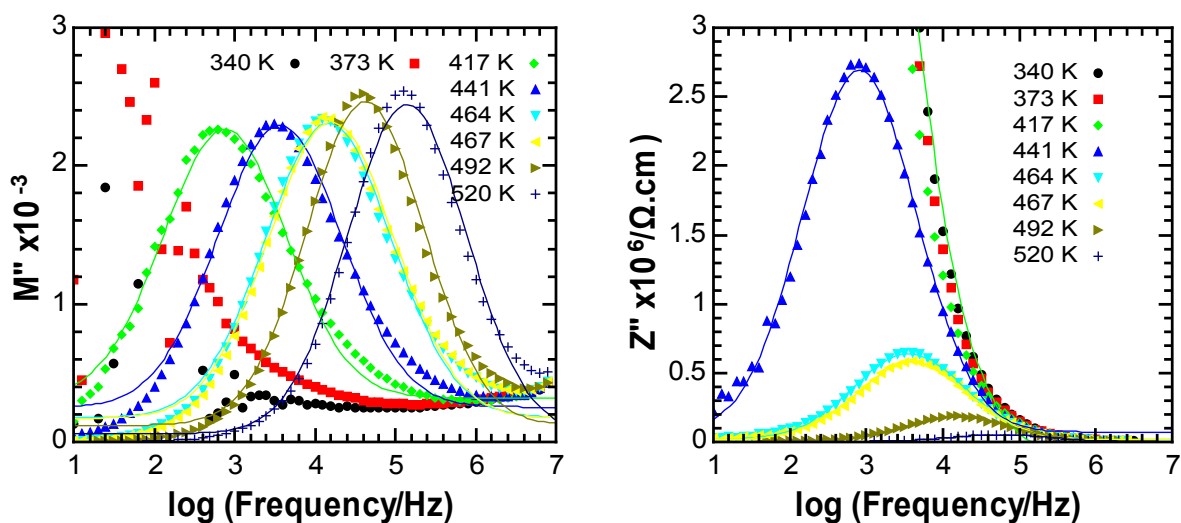


Figure 5.13: Imaginary modulus (left) and impedance (right) collected on heating; the $FWHM$ of the M'' peak varies between 1.45 – 1.60 decades.

5.10 Possible origins of the changes in the electrical response

The observed changes in the immittance spectra relating to the *FWHM* and peak shape may be attributed to one of a number of different scenarios. Changes in the relative phase fraction as a function of temperature, where the phases have different resistances and associated activation energies, may influence the *FWHM* and peak profile. Troyanchuk *et al.* suggest that the polar *R3c* and antipolar *Pnam* phases have similar thermodynamic potentials and the transition between the phases has a large associated activation energy.²⁰ This allows phase coexistence and an isothermal structural change.²⁰ Considering the two phases, '*Imma*' and *Pnma*, have the same elemental compositions (at least in terms of cation composition) with similar unit cell volumes, their respective polarisabilities must therefore be similar based on the Clausius Mossotti relationship²¹ and the respective ionic polarisabilities.²²

$$\kappa' = \frac{(3V_m + 8\pi\alpha_D^T)}{3V_m - 4\pi\alpha_D^T} \quad \text{Equation 5.4}$$

where κ' is the calculated permittivity, V_m the molar volume, α_D^T the total dielectric polarisability.

If the resistivities of the phases are similar, the time constants will also be similar and therefore the positions of the peaks associated with the electroactive response of the phases should appear at similar frequencies. The phases may have different activation energies associated with the dominant conduction process. In general, this will lead to a subtle broadening or narrowing of the peaks in the immittance spectra as a function of temperature. Assuming the phases are electrically distinguishable, significant changes in phase fraction will clearly affect the volume fraction and cross-section of grains and therefore the relative contributions of the components in the complex modulus and M'' spectra will change accordingly.

The *FWHM* and peak profile may also be affected by a concentration gradient of defects, such as oxygen vacancies, between the core and the grain boundaries. A schematic of a core shell model is shown in Figure 5.14. This idea of a concentration gradient means changes in the immittance spectra could be due to an annealing process where the oxygen vacancies

are able to migrate through the sample during the course of collection of isothermal immittance data.

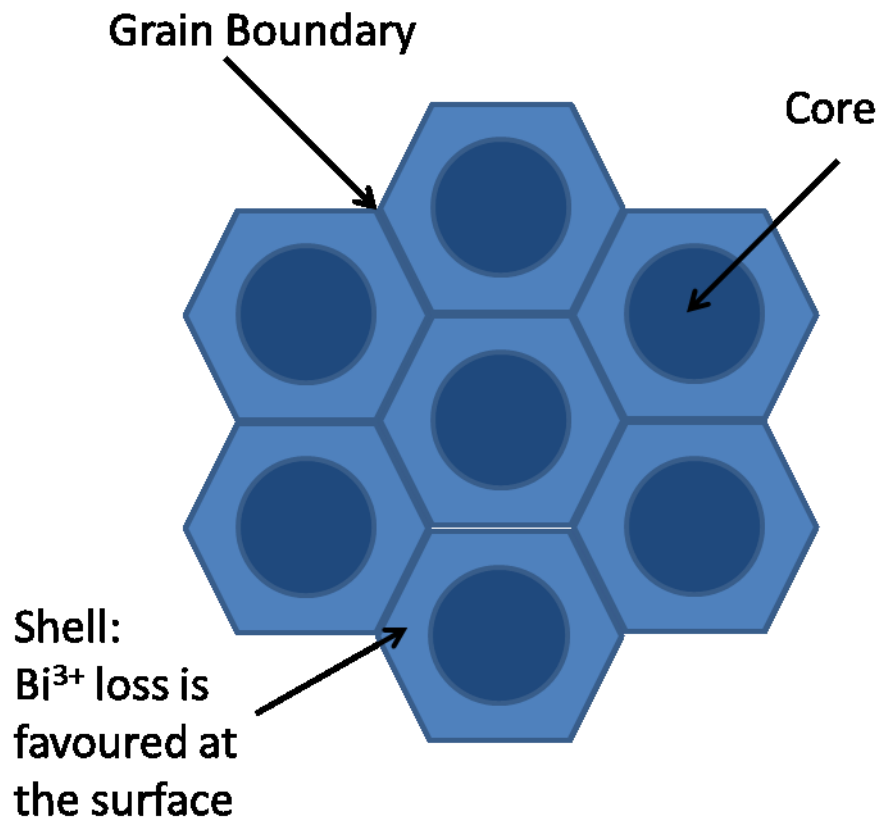
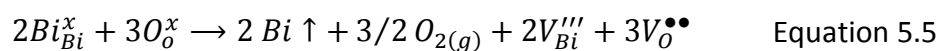


Figure 5.14: An idealised representation of a core-shell model.

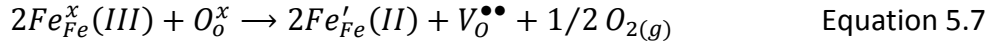
Before discussing this argument further, Kröger–Vink notation has been used to describe the formation of defects. Defects in the sample may occur due to Bi³⁺ loss. This process will be favoured at the surface and results in the formation of Bi³⁺ and oxygen vacancies to maintain the lattice charge neutrality as shown in Equation 5.5.



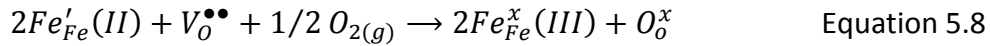
On cooling, the oxygen vacancies may be backfilled resulting in p-type conduction.



The other possible defect mechanism involves the reduction of Fe³⁺ to Fe²⁺ (resulting in n-type conduction). This mechanism can occur throughout the lattice as diffusion of oxygen will be much faster than that of bismuth cations for Bi volatilisation.



On cooling, the reduction process will reverse and Fe²⁺ will be reoxidised, forming Fe³⁺ and removing some of the associated oxygen vacancies.



These processes are kinetically controlled and given enough time will reach an equilibrium state. As the diffusion process is relatively slow, the sample may not reach this equilibrium state on cooling during the final synthesis step. This might mean the sample only reaches a homogenous equilibrium state during the electrical analysis. In this case, as the concentration gradient of defects changes during the experiment, the resistivities associated with the different electroactive regions change and the Debye peak positions shift in the immittance spectra accordingly.

The different effects relating to the conduction process may be intrinsically linked such that a concentration gradient of defects may favour one phase over another and therefore an annealing process changing the distribution of defects may change the relative phase fractions. Zacate *et al.* show using theoretical calculations that oxygen vacancies cause a significant displacement in the surrounding oxygen lattice.²³ The cumulative effect of a number of oxygen vacancies may result in a bias towards one of the '*Imma*' or '*Pnma*' phases. Changes in the immittance spectra as a function of temperature in this scenario are due to a change in the distribution of defects, which may alter the phase fractions.

Before describing how these scenarios may relate to the samples, it should be stressed that the current data are insufficient to conclusively state which of the described scenarios is correct and proceeding descriptions should be viewed as potential interpretation of the observed electrical responses.

In BLFO40 Air sample, the changes in the electroactive response (Figure 5.4) occur over a temperature range where the phase composition shown from the PND data between '*Imma*' and '*Pnma*' significantly alter. The exact phase fractions may vary as the neutron data

have been collected on a sample where all steps were performed under nitrogen, as outlined in chapter 2. The PND study shows the phase composition at 390 K is approximately 2:3 '*Imma*':*Pnma*. On further heating, the '*Imma*' phase transforms to *Pnma* (Figure 5.2). The phase fractions at 510 K are *circa* 1:9 and the broad feature in the M'' frequency spectra narrows on heating accordingly. This narrowing of the response is also observed in the Z'' spectra (Figure 5.4).

On cooling, considering the large region of phase coexistence the transformation to '*Imma*' and that the phases fractions may not be identical to that observed during the heating process *i.e.*, there could be some hysteretic behaviour. This hysteresis may also be observed in the immittance spectra and could explain the changing response in the M'' spectra on cooling.

Although the changing electrical response may be due to changes in the phase composition, this is not conclusive and other possibilities must be considered. The grains may be electrically inhomogeneous *i.e.*, the core of the grain may be more conducting than the surface or *vice versa* due to a defect (oxygen vacancy) concentration gradient. On heating, these defects can migrate and the sample becomes more homogeneous.

This possible scenario might describe the electrical data of BLFO25 (Figure 5.10). On the subsequent heating of BLFO25, the response in the M'' spectra remains Debye-like, where previously the response was electrically inhomogeneous. This suggests the changes in the conduction process(es) are irreversible. This would be expected if there were a defect concentration gradient through the grains. If changes in the electrical behaviour are due to a changing defect gradient, an *in-situ* electrical and structural study may reveal subtle changes in the overall composition as a function of temperature. However, such a study would prove to be technically difficult.

In the electrical data from BLFO25 it was possible to extract activation energies from the dominant capacitive responses on the first heating. The two activation energies were 0.81 - 0.85 eV and 0.46 - 0.53 eV. The second heating only revealed the component with the larger activation energy estimated in the range 0.71 – 0.90 eV. This may represent a shift from a polaron hopping dominated process where the oxidation state of Fe changes between Fe^{3+} and Fe^{2+} to a process that is dominated by oxygen vacancies. Changes in BLFO40 Air may be

similar, as the profile of the M'' spectra responses are similar in both samples on the first heating. However, this is speculative as activation energies to support this argument could not be extracted from the BLFO40 Air data.

BLFO40 1100 has a bulk activation energy *circa*. 0.46 – 0.5 eV. This is probably associated with polaron hopping linked to changes in the oxidation state of Fe^{3+} . In BLFO40 N_2 the bulk activation energy is 1.18 - 1.2 eV which is similar to BLFO40 Air at high temperature. These activation energies can be associated with oxygen vacancies. The *FWHM* of these samples are above 1.14 decades and tend towards this value with changing temperature. This may suggest that the electroactive responses are comprised of components from both phase fractions with subtly different activation energies.

5.11 Activation energies in $\text{Bi}_{1-x}\text{La}_x\text{FeO}_3$

The two broad categories of activation energies (either *ca.* 0.5 eV or *ca.* 1.1 eV) observed in the BLFO40 and BLFO25 compositions discussed above have also been observed in an range of other compositions of $\text{Bi}_{1-x}\text{La}_x\text{FeO}_3$. All samples were synthesised in air and the synthesis temperatures and durations are outlined in chapter 2. The complex modulus data for these samples shows a dominant electroactive response in the spectra from which activation energies can be determined. As in chapters 3 and 4, bulk conductivities, $\sigma_b (= R_b^{-1})$ were estimated over a range of temperature using capacitances obtained from M^* and M''_{\max} frequency using the relationship $RC = 1/2\pi f_{\max}$. The conductivity determined from M^* data show the expected temperature dependence described by the Arrhenius expression

An Arrhenius plot of bulk conductivities is shown in Figure 5.15 where it can be seen that over the broad range of samples there are two distinct groupings corresponding to activation energies in the range 0.45 – 0.49 eV and 1.06 -1.20 eV. It should be pointed out while $x = 0.4$ shares the same synthesis route as BLFO40 Air, the response is homogeneous with an activation energy *circa* 1.16 eV. This demonstrates the sensitivity of subtle changes in the reaction conditions between batches despite the best efforts to replicate reaction conditions. BLFO40 1100 and BLFO40 N_2 have been added to demonstrate within a single batch of material the conductivity can be tailored between the two different conductivities. The BLFO25 data set corresponds to the modulus data collected on cooling.

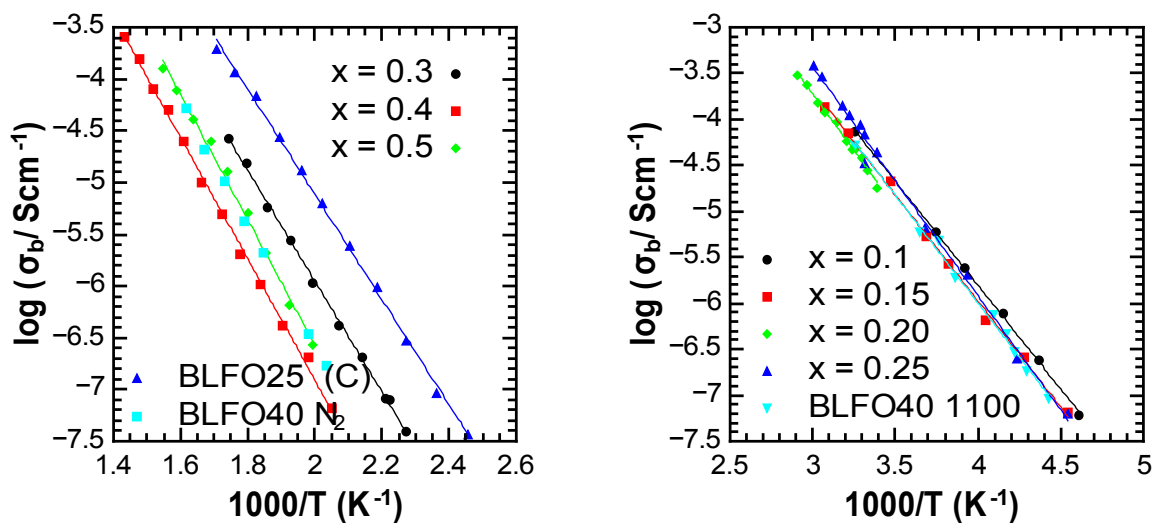


Figure 5.15: Arrhenius plots of bulk conductivities determined from M^* data showing two groupings of activation energies.

5.12 Conclusions

In summary, a comparison of the total capacitance in the inhomogeneous BLFO40 Air sample compared with the bulk response of homogeneous samples shows a strong correlation. This suggests that the dominating contribution to the overall response is similar *i.e.*, the bulk. Therefore, differences in the time constants observed between samples are due to different conductivities of the various electroactive regions which constitute the bulk response.

A number of samples have been synthesised with broad responses in the M'' spectra. Peak maxima for some of the samples can be estimated, *e.g.* BLFO25, and activation energies can be assigned to the different electroactive responses. This reveals two significantly different activation energies, which may be attributed to different dominant conduction processes *i.e.*, a polaron hopping model and migration of charge *via* oxygen vacancies. These changes may be associated with a core-shell model with a concentration gradient of defects in the sample. However, as there may be changes in the phase composition of the samples the different conduction processes may be associated with the individual phases. The different scenarios may be linked such that a change in the concentration of defects which will affect the lattice may be sufficient to change the phase fractions.

In the most electrically homogeneous samples, the $FWHM$ changes as a function of temperature. This may suggest that both phases contribute to the electroactive response and have very similar activation energies. Changes in the $FWHM$ will then occur due to this difference in activation energy.

Studying a wide variety of compositions has shown that the activation energies fall within one of two ranges, *circa* 0.5 eV or 1 eV, and can be attributed to polaron hopping or migration of charge *via* oxygen vacancies, respectively.

This study demonstrates that the electrical analysis of BiFeO₃-based samples is complex owing to the presence of multiple electroactive regions and the sensitivity to subtle changes in the reaction conditions. ac-Impedance measurements, particularly using a combined formalism approach such as impedance/modulus spectra, is therefore a vital tool in the understanding of the overall electrical behaviour of these materials as it allows the separation of the electroactive responses which is lost in DC or fixed frequency (total capacitance) measurements.

5.13 References

1. Yu. E Roginskaya, Yu. E Venevtsev, S. A Fedotov and G. S. Zhdanov, *Sov. Phys. Crystallogr.*, 1964, **8**, 490.
2. M. Polomska, W. Kaczmarek and Z. Pajak, *Phys. Status Solidi*, 1974, **23**, 567.
3. G. A. Smolenskii and V. M. Yudin, *Sov. Phys. Solid State* 1965, **6**, 2936.
4. S. J. Clark and J. Robertson, *Appl. Phys. Lett.*, 2007, **90**, 132903-132903.
5. G. Catalan and J. F. Scott, *Adv. Mater.*, 2009, **21**, 2463-2485.
6. R. Palai, R. S. Katiyar, H. Schmid, P. Tissot, S. J. Clark, J. Robertson, S. A. T. Redfern, G. Catalan and J. F. Scott, *Phys. Rev. B*, 2008, **77**, 014110.
7. S. K. Pradhan and B. K. Roul, *Physica B*, 2011, **406**, 3313-3317.
8. M. Valant, A.-K. Axelsson and N. Alford, *Chem. Mater.*, 2007, **19**, 5431-5436.
9. K. Kalantari, I. Sterianou, S. Karimi, M. C. Ferrarelli, S. Miao, D. C. Sinclair and I. M. Reaney, *Adv. Funct. Mater.*, 2011, **21**, 3737-3743.
10. Z. Hu, M. Li, Y. Yu, J. Liu, L. Pei, J. Wang, X. Liu, B. Yu and X. Zhao, *Solid State Commun.*, 2010, **150**, 1088-1091.
11. Y. P. Wang, G. L. Yuan, X. Y. Chen, J. M. Liu and Z. G. Liu, *J. Phys. D: Appl. Phys.*, 2006, **39**, 2019.
12. D. C. Arnold, K. S. Knight, F. D. Morrison and P. Lightfoot, *Phys. Rev. Lett.*, 2009, **102**, 027602.
13. P. Patnaik, *Handbook of Inorganic Chemicals*, McGraw-Hill Professional, 2002.
14. D. A. Rusakov, A. M. Abakumov, K. Yamaura, A. A. Belik, G. Van Tendeloo and E. Takayama-Muromachi, *Chem. Mater.*, 2011, **23**, 285-292.
15. J. T. S. Irvine, D. C. Sinclair and A. R. West, *Adv. Mater.*, 1990, **2**, 132-138.
16. F. D. Morrison, *Synthesis and Electrical Characterisation of Lanthanum Doped Barium Titanate*, PhD Thesis, University of Aberdeen, 1999
17. M. S. Islam, *J. Mater. Chem.*, 2000, **10**, 1027-1038.
18. I. O. Troyanchuk, D. V. Karpinsky, M. V. Bushinsky, O. S. Mantytskaya, N. V. Tereshko and V. N. Shut, *J. Am. Ceram. Soc.*, 2011, n/a-n/a.
19. I. O. Troyanchuk, M. V. Bushinsky, D. Karpinskii, O. Mantytskaya, V. Fedotova and O. Prokhnenko, *JETP Letters*, 2008, **87**, 641-644.
20. I. O. Troyanchuk, D. V. Karpinsky, M. V. Bushinsky, V. A. Khomchenko, G. N. Kakazei, J. P. Araujo, M. Tovar, V. Sikolenko, V. Efimov and A. L. Kholkin, *Phys. Rev. B*, 2011, **83**, 054109.
21. R. D. Shannon, *J. Appl. Phys.*, 1993, **73**, 348-366.
22. R. D. Shannon, *Acta Crystallogr. Sect. A: Found. Crystallogr.*, 1976, **32**, 751-767.
23. M. O. Zacate, L. Minervini, D. J. Bradfield, R. W. Grimes and K. E. Sickafus, *Solid State Ionics*, 2000, **128**, 243 – 254.

Summary, Conclusions and Future work

6.1 Summary

A number of different $\text{Bi}_{1-x}\text{RE}_x\text{FeO}_3$ (RE = La, Nd) samples have been synthesised using standard solid-state methods. The samples have been analysed with powder neutron diffraction (PND) and ac-immittance spectroscopy (ac-IS). This revealed isostructural displacements and a change in magnitude of the octahedral tilts as a function of temperature. These changes occur due to a changing balance between the magnetic properties and other bonding contributions in the respective systems leading to phenomena such as negative thermal expansion and magnetostriction (invariant lattice parameters *i.e.*, the invar effect).

Synthesis conditions have been varied resulting in a wide range of bulk conductivities demonstrating the need for careful synthesis and analysis with ac-IS to separate the individual contributions in the immittance spectra.

6.2 Conclusions

Chapter 3 discussed a wide band gap semiconductor, $\text{Bi}_{0.5}\text{La}_{0.5}\text{FeO}_3$ (BLFO50), which was primarily studied with PND and ac-IS. BLFO50 adopts the orthorhombic GdFeO_3 structure with a G_z antiferromagnetic unit cell ($Pn'ma'$). Further analysis showed the structural and dielectric behaviour is driven by the magnetic properties. Structural distortions were analysed using both conventional Rietveld analysis and the symmetry mode analysis tool ISODISTORT. An unusual orthorhombic distortion with an increasing in-phase tilt as a function of increasing temperature was revealed. This was accompanied by corresponding A-site antipolar atomic displacements where the lanthanum and bismuth are displaced by different degrees along the a -axis. The onset of antiferromagnetic order *circa* $T_N \sim 704$ K and a magnetostrictive, Invar effect along the magnetic c -axis causes the unusual variation in the orthorhombic distortion.

Chapter 4 studied the Nd analogue $\text{Bi}_{0.7}\text{Nd}_{0.3}\text{FeO}_3$ (BNFO30), which adopts the same GdFeO_3 structure as BLFO50, with the same antiferromagnetic G_z ordering. The electrical properties reveal BNFO30 is a semiconducting relaxor, which contrasts with the lanthanum analogue.

At low temperature, the unit cell undergoes negative thermal expansion, which prompted further investigation into the origins of this unusual structural evolution. In-depth analysis showed that the material's structure and dielectric behaviour is mediated by superexchange. Competition between covalent bonding and the G_2 -type antiferromagnetic order drives changes in the tilt behaviour below the Néel temperature (*circa.* 642 K). Superexchange favours linear Fe-O-Fe interactions, which means both tilt modes decrease on cooling. The competition between covalent bonding and magnetism results in more subtle effects, such as distortions in the octahedra and a shortening of the axial Fe-O1 bond together with corresponding A-site displacements along the *c*-axis.

In contrast to BLFO50, which utilises anomalous behaviour of the in-phase tilt to relieve strain, BNFO30 uses both in-phase and anti-phase tilts. This is probably due to the relative sizes of the A-site cations competing with the effects of magnetic superexchange.

Chapter 5 studied a number of samples that have a broad range of electrical responses. Based on a comparison of the total sample capacitance of electrically inhomogeneous samples compared with the bulk response of homogeneous samples the overall electrical response is dominated by bulk behaviour in all cases. Therefore, the observed differences in the time constants in samples are due to different conductivities of the various electroactive regions which constitute the bulk region. Samples with particularly broad features in the M'' spectra, *e.g.*, on the initial heating of BLFO25, were assigned activation energies associated with different electroactive responses. This reveals two significantly different activation energies, which may be attributed to different dominant conduction processes *i.e.*, a polaron hopping model and migration of charge *via* oxygen vacancies. These changes may be associated with a core-shell model and a concentration gradient of defects. However, there are other possibilities that cannot be discounted. There are significant changes in the phase composition of the samples with changing temperature and the different conduction processes may be associated with the individual phases. These scenarios may be linked and a concentration gradient of defects may influence the phase assembly.

The full width half maximum (*FWHM*) has been used to gauge the electrical homogeneity of the samples. In the most electrically homogeneous samples, *i.e.*, samples with *FWHM* close to the ideal 1.14 decades, changes as a function of temperature may suggest that both

phases contribute to the electroactive response and have very similar activation energies. In this case, changes in the *FWHM* are due to differences in activation energy. Studying a range of samples with different compositions reveals that activation energies fall into one of two regimes, *circa.* 0.5 eV or 1.0 eV which can be associated with polaron hopping or migration of charge *via* oxygen vacancies, respectively.

This study demonstrates that the electrical analysis of BiFeO₃ based samples is complex owing to the presence of multiple electroactive regions. ac-IS is a vital tool as it allows the separation of the electroactive responses and a more in-depth understanding of the electrical properties. Specifically, the combination of impedance and modulus data is particularly powerful as it allows: 1) simple separation of electroactive responses considered to be in a series pathway (*i.e.*, the brick layer model); and 2) the modulus is most sensitive to the response with the lowest associated capacitance, *i.e.* the bulk. This level of information is lost in the most commonly used direct current (including leakage current) or fixed frequency (total capacitance) measurements which give only a total, composite response with no detail on the number, or relative magnitudes of, various electroactive responses.

The use of symmetry-mode analysis in combination with conventional analysis of PND data has revealed subtle structural changes *i.e.*, oxygen displacements, which are responsible for changes in the electrical and other physical properties. This subtlety is only revealed with techniques like PND, which are sensitive to the oxygen positions. The use of symmetry-mode analysis (*via* ISODISTORT), in combination with conventional crystallographic analysis, is therefore an important step forward in researching materials like rare earth doped BiFeO₃.

In a wider sense, this combined approach for both structural and electrical analyses presents a new paradigm for investigation of structure-property relationships in a range of electroceramic materials.

6.3 Further Work

There are a number of possible directions for further research. Chapters 3 and 4 show that Bi_{1-x}RE_xFeO₃ is strongly influenced by the G-type antiferromagnetic order. This magnetic order competes with other bonding contributions and influences the electrical properties. It

may be possible to disrupt this order by B-site doping with Co^{3+} . A theoretical study of the $\text{BiCo}_{1-x}\text{Fe}_x\text{O}_3$ system suggests that C-type antiferromagnetic order can be induced at a composition $\text{BiCo}_{0.875}\text{Fe}_{0.125}\text{O}_3$.¹ If the magnetic order can be tailored, it may be useful for magnetoelectric device applications.

Other rare earth doped $\text{Bi}_{1-x}\text{RE}_x\text{FeO}_3$ with smaller ionic radii can be studied such as $\text{RE} = \text{Tb}^{3+}$ and Dy^{3+} . Studying these rare earth systems may lead to further understanding about the A-cation size and its influence on the structure-property relations.

Chapter 5 raises a number of questions about the electrical behaviour in $\text{Bi}_{1-x}\text{La}_x\text{FeO}_3$. An *in situ* electrical and structural study may reveal a link between changes in the electrical properties and the phase fractions. This may be achieved with a temperature dependent X-ray diffraction (XRD) study, which will simplify the diffraction pattern, revealing only structural contributions.

A temperature dependent study may also reveal if there is a concentration gradient of defects. If the sample is held at temperature over an extended period of time this may result in changes in the immittance spectra.

6.4 References

1. C. Xing-Yuan, T. Ren-Yu, W. Jian-Ming, Z. Yu-Jun, D. Hang-Chen and D. Chun-Gang, *J. Phys.: Condens. Matter*, 2011, **23**, 326005.